Advanced Magnetic Resonance Imaging in Lung Mesothelioma

Lin Cheng

A thesis submitted for the degree of

Doctor of Philosophy

of the

University of London

Cancer Research UK Imaging Centre
The Institute of Cancer Research and The Royal Marsden NHS Trust

2018

Declaration

I hereby declare that this thesis reports on my own original work. Any information has been derived from other sources has been indicated in the thesis.

Lin Cheng

Abstract

Malignant pleura mesothelioma (MPM) has a rind-like growth pattern and may have both solid disease and pleural fluid, so it is very challenging to accurately categorize change in tumour burden using size-based tumour response criteria, e.g. modified Response Evaluation Criteria in Solid Tumours (RECIST). Diffusion Weighted Magnetic Resonance Imaging (DWI) provides functional information of tissue microstructure and is a promising technique to enable segmentation of tumours due to its excellent contrast between tumour and suppressed background. The aim of this thesis is to evaluate the changes in tumour volume and functions during treatment thus assess disease treatment response using DWI. A novel method, T_2-adjusted computed diffusion weighted magnetic resonance imaging (T_2-cDWI), is proposed to improve the image contrast between solid tumour and pleural effusion, and may eliminate T_2 shine-through effect. In T_2-cDWI, T_2-weighted echo-planar images at multiple ($\geqslant$2) echo times were acquired in addition to the standard DWI acquisition protocol. To acquire the solid tumour volume, a workflow including image segmentation and classification has been investigated on DWI images and further applied in a clinical mesothelioma study for treatment response evaluation. DWI imaging protocols were developed to dovetail with a routine clinically chest scan for treatment evaluation. Using previously developed workflow, volumetric tumour burden and DWI parameter values are obtained and shown to be correlated with disease progression after treatment. These results clearly show the potential for the developed tools as a novel and quantifiable biomarker for assessing the volumetric response of MPM to therapy compared with the conventional modified RECIST. In summary, this thesis has investigated and provided a new volumetric response assessment strategy for MPM patients using DWI images.

Acknowledgements

Undertaking this PhD was a truly life-changing experience for me and it would not have been done without the advice and supports of my supervisors, my colleagues and my family.

Foremost, I would like to express my huge gratitude to David Collins. David is an excellent supervisor and mentor and I would like to thank him for lighting my mind up and encouraging me to work on this project. He was my trusted compass whenever research reached a cross-road, an able guide when the journey could not be made alone and a friendly companion while savouring the mini accomplishments along the way. Without his supports, open-mindedness and the trust that he showed towards me, most of this work would have not been accomplished. His genuine enthusiasm for novel ideas and discoveries always served as the best motivation for carrying out this work. I would like to sincerely thank Professor Dow Mu Koh and Professor Martin Leach, for their supervision and guidance which helped me in completing this task through various stages in the four years of research. Special thanks to my senior mentor Professor Jeffery Bamber for being always supportive and available for questions and advice. I would like to thank him for being always there in critical and stressful times and for putting off a lot of fires.

I also appreciate Dr. Matthew Blackledge for all the exciting intellectual interactions, continuous guidance and friendship. I am deeply thankful for him always being willing to share his vast knowledge in MRI, being patient to answer all my questions, and being supportive to my work during this period. I also offer my profound appreciation to the brilliant scientists, Dr. Matthew Orton, Dr. Neil Jerome and Dr. James D'Arcy, for all helps, discussions and advice. I wish to acknowledge the help and support of Dr. Nina Tunariu and radiographers in the Royal Marsden Hospital for their efforts in providing and scanning patients whose datasets have been used throughout this project. I also thank all the mesothelioma patients registered in this clinical trial.

I would like to dedicate this thesis to my family: my sister, father and mother, thanks for their endless encouragements, understandings and love. Without these, it would

be impossible for me to finish my PhD. My deepest gratitude goes to my partner, Mohammad Azizian, who has always been by my side, thanks for caring, understanding, supporting and inspiring me in this long journey.

This research has been funded by British lung foundation.

Contents

List of Figures

List of Tables

List of Acronyms

18FDG 18F-Fluorodeoxyglucose
ADC .....Apparent Diffusion Coefficient
BW .....Band Width
CA .....Cellular Automata
cDWI.....Computed Diffusion-Weighted Magnetic-Resonance Imaging
CI .....Confidence Interval
CNR .....Contrast to Noise Ratio
CR .....Complete disease
CT .....Computed Tomography
CV.....Coefficient of Variation
DCE-MRI .....Dynamic Contrast-Enhanced MRI
DWI .....Diffusion-Weighted Imaging
EM.....Expectation Maximum
EPI .....Echo Planar Imaging
EPP.....Extrapleural Pneumonectomy
FFT .....Fast Fourier Transform
FID .....Free Induction Decay
FOV .....Field of View
GC .....GrowCut
GMM .....Gaussian Mixture Model
GRAPPA ..... GeneRalised Auto-calibrating Partially Parallel Acquisitions
IMIG ..... International Mesothelioma Interest Group
IMRT..... Intensity-modulated radiation therapy
IVIM.....Intravoxel Incoherent Motion
LoA .....Limits of Agreement
LS.....Least Square Fitting
MPM .....Malignant pleural Mesothelioma
mRECIST ..... Modified Response evaluation criteria in solid tumours
MRI.....Magnetic Resonance Imaging

MVD.....Microvessel Density
NMR.....Nuclear Magnetic Resonance
NSA.....Number of Signal Averages
PCA.....Principle Component Analysis
P/D.....Pleurectomy/Decortication
PD.....Progressive Disease
PDMS.....polydimethylsiloxane
PE.....Phase Encode orientation
PET.....Positron Emission Tomography
PERCIST.....PET Response Criteria in Solid Tumors
PGSE .....Pulsed Gradient Spin Echo
PI .....Parallel Imaging
PR.....Partial Response
RECIST.....Response evaluation criteria in solid tumours
RF.....Radio Frequency
RM.....Random Walk
ROI.....Region of Interest
SD.....Stable Disease
SE.....Spin Echo
SNR.....Signal to Noise Ratio
SPAIR.....SPectral Attenuation Inversion Recovery
SPIR.....SPectral Inversion Recovery
SSFP.....Steady State Free Precession
STIR.....Short Tau Inversion Recovery
SUVmax.....Maximum Standardized Uptake Value
T2-cDWI..... T2-adjusted Computed Diffusion-Weighted Imaging
TE.....Echo Time
TNM.....Tumour-Node-Metastasis
TR.....Repetition Time
TTV.....Total Tumour Volume
VOI.....Volume of Interest
WHO.....World Health Organisation
WLS.....Weighted Least Square Fitting

1 Introduction

In **Section 1.1**, malignant pleural mesothelioma will be briefly introduced, including its particular growth pattern, staging, treatments as well as the evaluation of treatment response. The motivation and challenges of this PhD project will be addressed in **Section 1.2**, followed by the aims of this thesis. **Section 1.3** will present the structure of the rest of the thesis.

1.1 Introduction

Since the middle 19th century, asbestos fibres were widely used in construction and fireproofing in most countries, such as fire-retardant coatings, bricks, ceiling insulation, fireproof drywall etc., due to its desirable physical properties of sound absorption, resistance to fire, heat, and electricity. However, scientists found that long-time exposure to asbestos may increase the risk for asbestos-related health issues [1]. Among all diseases associated with asbestos, the most notable one is malignant pleural mesothelioma (MPM), a highly aggressive neoplasm that forms in the linings of the lungs and chest walls [1-3]. MPM has a relative low incident rate (41 per million population in the UK in the year of 2015 [4]) compared to other malignancies such as breast tumour, lung cancer etc.; however, it has been increasing rapidly over the past few decades as a result of the widespread use of asbestos between 1950-1980. Over the last half-century annual deaths caused by mesothelioma in the UK increased 16 fold [5] (**Figure 1.1**).

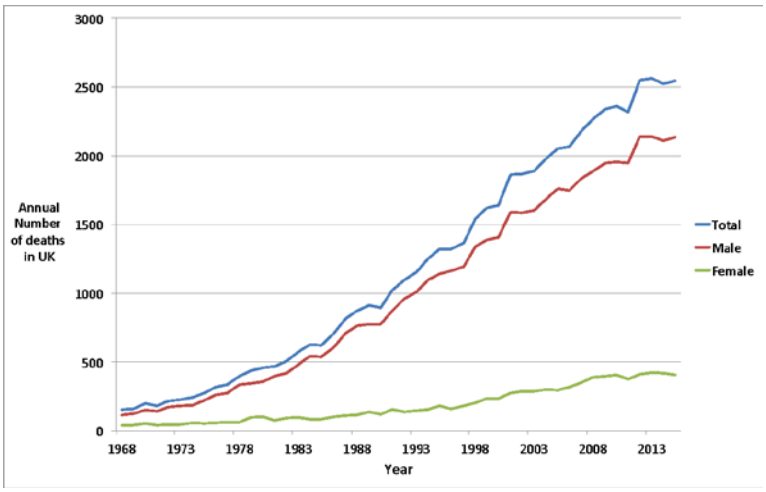

Figure 1.1: Annual number of deaths caused by mesothelioma in UK from 1968 to 2015 [5].

The prognosis for MPM patients is poor, with a median survival of 9 -17 months [6]. There are a number of potential contributing factors to the poor disease survival in MPM. First, the disease is usually multifocal at diagnosis with multiple tumour nodules along the pleura and lung fissures at presentation, sometimes also involving the diaphragm and pericardium, rendering a complete surgical resection impossible. Second, despite the known association between asbestos and MPM, there is a long latency between asbestos exposure and the onset of MPM, making the life-long surveillance of disease within the at-risk population challenging. Third, conventional chemotherapy has not been very effective for the treatment of these cancers, although promising new targeted therapies are now beginning to emerge. Last but not least, there is still a significant challenge for the accurate quantification of disease burden and the assessment of disease response to treatment. This has undoubtedly had an impact on clinical trial designs in MPM, and the robustness of end-points used to define disease response or progression in research and clinical practice.

1.1.1 Malignant pleural mesothelioma

There are three major histological subtypes of MPM, epithelioid (about 70% of all MPM cases), sarcomatoid (15-20%), and mixed or biphasic, which is a mix of the epithelial and sarcomatoid cell types [7]. In malignant pleural mesothelioma, the tumour originates from mesothelial cells lining the pleura [1-3]. Unlike other solid tumours, malignant pleural mesothelioma grows as thin diffuse sheet-like extensions throughout the pleural cavity [8-10]. In addition to the formation of solid tumours, pleural effusion is common in MPM [1] and may be difficult to distinguish, especially when complicated by haemorrhage or exudates, from solid pleural disease using routine clinical imaging approaches such as conventional computed tomography (CT) or magnetic resonance imaging (MRI) (**Figure 1.2**). The shape of MPM and the presence of both solid disease and pleural effusion makes it challenging to accurately quantify the disease burden and assess treatment response.

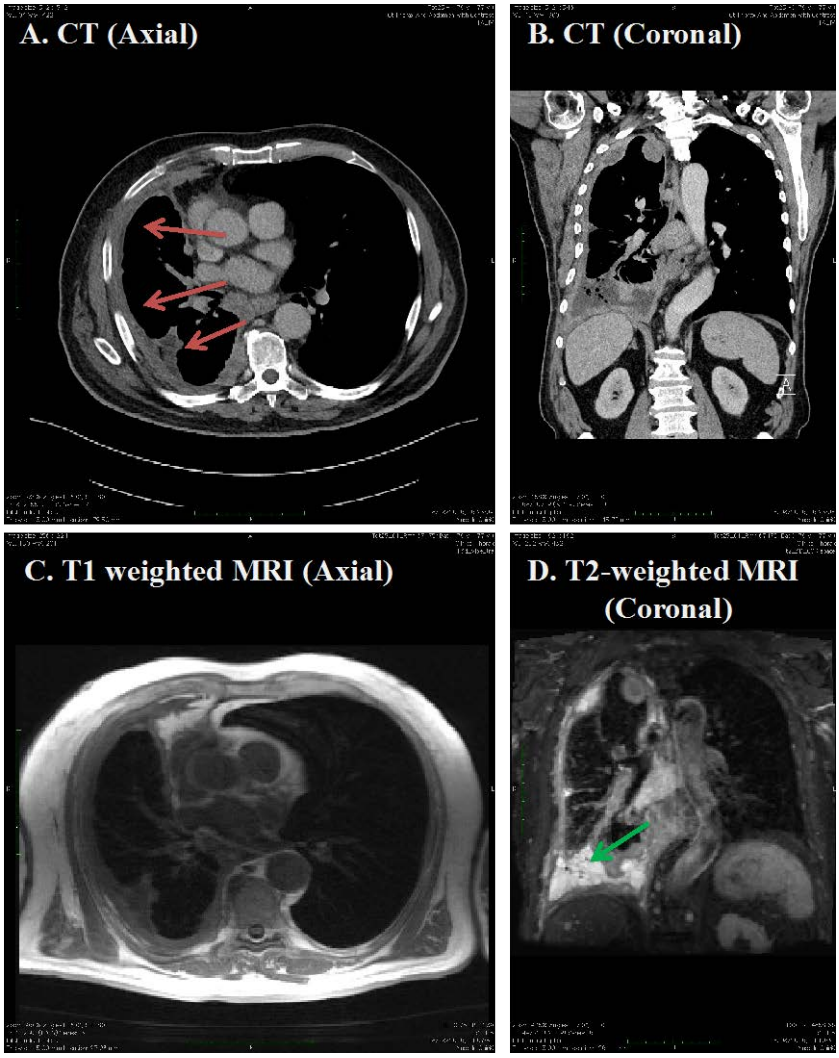

Figure 1.2: (A) Axial and (B) coronal reformat CT, (C) Axial T1-weighted and (D) Coronal T2-weighted MRI of a 77-year-old man with malignant mesothelioma of the right hemithorax.

Note the rind of irregular pleural thickening (Red arrows) encasing the right lung is typical of the disease. The green arrow refers to the pleural effusions.

1.1.2 Staging

In 1995, the International Mesothelioma Interest Group (IMIG) proposed a tumour-node-metastasis (TNM) staging system for MPM (**Appendix 1**) [11]. The revised Brigham and Women's Hospital surgical staging system defined four stages of MPM with respect to resectability, tumour histology, and nodal status [7]. Although staging is beyond the scope of this work, the fact that the MPM phenotype could be associated with metastasis gave rise to the hypothesis that in-vivo imaging may serve as an appraisal tool to refine the decision making on whether or not to intervene. The readers are encouraged to find more information in **Appendix 2**.

1.1.3 Treatment and treatment effectiveness evaluation

Most existing treatments in MPM remain palliative rather than curative. Currently there are three main treatment approaches followed by clinicians, namely, surgery, radiation therapy and chemotherapy; these treatments can be employed individually or in tandem.

1.1.3.1 Surgery

Surgery was performed for patients without obvious signs for widespread chest wall invasion (resectable chest wall lesions were accepted) or obvious infiltration of mediastinal structures as the aorta, heart, spine or oesophagus according to the CT scan [12]. There are two main surgical procedures in mesothelioma: extrapleural pneumonectomy (EPP) and extended pleurectomy with decortication (also known as pleurectomy/Decortication, P/D) (**Figure 1.3**).

EPP is a radical surgical procedure that generally involves the removal of the entire tissues from the affected hemithorax, including the affected lung, pleura, pericardium and diaphragm, etc. [13]. EPP is associated with significant morbidity and complication although it was reported to enhance survival in the original description of EPP [13-15]. These reports, based on highly selected patients, are not from

randomised controlled trials. Via a systematic review, Looser et al. concluded that it was almost impractical to determine whether EPP improves survival or effectively palliates the symptoms of MPM patients [16].

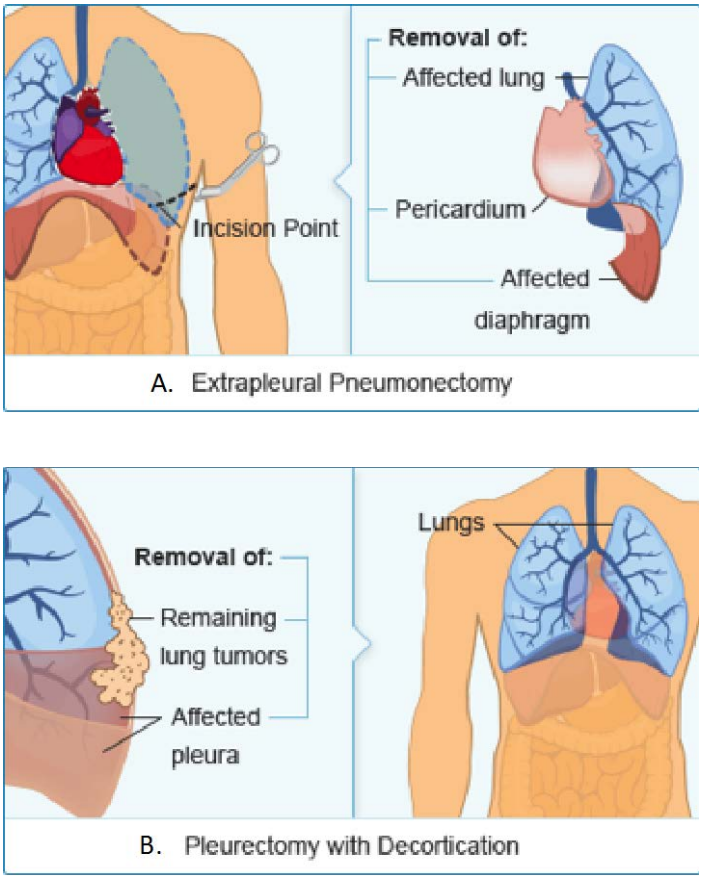

Figure 1.3: Illustrations of two surgery options in MPM: (A.) extrapleural pneumonectomy (EPP) and (B.) extended pleurectomy with decortication (P/D).

Image source: www.mesotheliomaguide.com/treatment/surgery/

Pleurectomy/Decortication (P/D) is a more conservative lung-sparing procedure and it involves resection of the macroscopic visible tumour, including the visceral and

parietal pleura. It is usually performed in patients with stage 1 or early stage 2, in which cancer has not spread beyond the origin site. P/D is associated with less mortality and fewer surgical complications so it has gained more popularity in the last decade. As P/D does not aim for macroscopic complete resection, adjuvant treatment such as chemotherapy or radiotherapy is employed after operations, to minimize the residual microscopic tumour [17].

In most cases EPP was chosen as the surgical option when P/D was considered inadequate to achieve macroscopic complete resection, so most trials were subjected to evidence selection bias. Therefore, the benefit of surgery in MPM is still much debated specifically with respect to the absence of strong randomised evidence.

1.1.3.2 Radiation therapy

On the one hand, radiotherapy is a promising approach to reduce chest wall masses, or use as a palliative method to treat symptoms or an adjuvant to surgery and chemotherapy within the context of timidity treatment. But on the other hand, MPM has a complex disease shape and large treatment volumes are required. It may cause a high risk of toxicity to the surrounding tissues after radiotherapy treatment. The dose delivery has been improved substantially using the so-called Intensity-modulated radiation therapy (IMRT). IMRT uses small radiation beams at multiple angles in a three-dimensional conformal pattern. Owing to the better dose localization, IMRT is promising to be used after EPP to avoid recurrence in the ipsilateral hemithorax. Regardless, to the knowledge of the author there are no randomised trials that show whether radiotherapy adds any value to prolong patient survival.

In general, it is difficult to deliver enough doses (> 60 Gy) to the entire tumour and, at the same time, avoid exposing the organs-at-risk to the high radiation dose. As a result, radiotherapy played a limited role in the treatment of MPM and has seldom been used as the primary choice for MPM treatment.

1.1.3.3 Chemotherapy

Only 10-15% of MPM patients are eligible for surgery, the rest are advised for chemotherapy or other palliative treatment approaches. Chemotherapy was not the method of choice in many cases, mainly due to the relative chemo-resistance of

mesothelioma and the lack of active agents with acceptable toxicity. The development of new effective chemotherapeutic agents and therapeutic combinations have paved the way for chemotherapy to become the most commonly adopted and mature treatment for MPM in the clinical practice. For example, in a multicentre randomised Phase III trial of 456 patients, Vogelzang has compared cisplatin alone with a combination of cisplatin and pemetrexed. The results showcased that the survival time of the combination arm has a significant benefit, 12.1 months versus 9.3 months for cisplatin alone [18]. Tumour response was 41.3% of the 226 pemetrexed and cisplatin treated patients and 16.7% of the 222 patients receiving cisplatin alone ($P < 0.0001$) [18]. This study led to the approval of the pemetrexed and cisplatin combination therapy as the standard treatment for mesothelioma patients who are not surgical candidates.

1.1.3.4 Treatment effectiveness evaluation

In clinical trials, the evaluation of treatment response in mesothelioma is crucial to optimally manage the disease, but also to improve the treatment outcomes of patients. Yet, there exists a significant challenge for the accurate and effective quantification of disease burden and the assessment of disease response to the treatment. Currently, there are various methods to address this issue, among which the size measurement criteria (e.g. WHO, Response evaluation criteria in solid tumours (RECIST) and modified RECIST) and functional imaging techniques (such as positron emission tomography (PET), diffusion-weighted MRI (DWI) and dynamic contrast-enhanced MRI (DCE-MRI)) are of more interest. A detailed literature review including the above-mentioned methods in mesothelioma is presented in **Chapter 2**.

1.2 Motivation and challenges

Modified RECIST (mRECIST) criteria is the current standard of treatment response assessment in MPM. It measures tumour thickness perpendicular to the chest wall or mediastinum in two sites at three different levels on transverse cuts of the CT scan. The sum of these six measurements is defined as a pleural uni-dimensional measurement and used to represent the tumour at a specific time point. Current

evidence suggests that the modified RECIST criteria is associated with a higher degree of inter-observer variability compared to a volumetric approach to assess therapy response [19]. This is attributed to the fact that the tumour size measurement is limited to only three slices and six positions in total. The main motivation of the presented dissertation therefore is the inherent limitations in size measurement criteria including mRECIST. There is an urgent need for a more reliable and easily-applied MPM treatment assessment approach on an imaging system that proffers enhanced tumour contrast.

Among the allied techniques in MRI, Diffusion-Weighted MRI appears to be one of the most promising functional imaging techniques to quantify various aspects of the tumour pathophysiology. DWI is relatively quick to perform and does not require the administration of any exogenous contrast agent. Additionally, the apparent diffusion coefficient (ADC) value quantified from DWI has been shown to reflect tissue cellularity, and may provide prognostic information [20; 21]. Trials in various tumour types demonstrated that ADC has good measurement repeatability and reproducibility, and a significant increase in ADC values is observed in responders to treatment [22]. As for MPM, clearly there is a demand for clinical trials using DWI; to investigate diffusion volume, and to explore the associated tumour ADC values as potential response, predictive and prognostic biomarkers. However, performing DWI in the lungs is still very challenging. The lungs have low proton density and MPM in the early stage presents as a very thin layer, so the images in the thorax DWI have low SNR and suffer serious susceptibility artefacts from air-tissue interfaces. Furthermore, due to the acquisition schemes employed in DWI, images are extremely sensitive to artefacts related to the respiratory and cardiac motion [2; 23; 24]. Last but not least, the definition of the whole MPM solid tumour volume is very challenging due to the special tumour growth pattern and the presence of both pleural effusion and solid tumour. On that account, DWI imaging for MPM remained challenging and a proper DWI protocol will be developed using a more adaptive approach better suited to the nature of MPM.

1.3 Aims

In order to properly address the above challenges, the aims of this thesis are to

- Develop optimised DWI imaging protocols as well as post-processing methods to improve DWI image quality for MPM.
- Develop volume analysis methods and quantify tumour heterogeneity.
- Investigate the potential of using DWI parameters (total tumour volume and ADC) to evaluate treatment response of MPM patients following a chemotherapy treatment.

1.4 Thesis structure

The organisation of the work is as follows.

Chapter 2 reviews the existing and potential criteria for MPM treatment response assessment, including the currently applied size measurement criteria on CT and MRI, and new functional imaging techniques, such as positron emission tomography, DWI and dynamic contrast-enhanced MRI.

Chapter 3 provides a brief background on the theory of both MRI and DWI. The purpose of this chapter is to provide a background for the following chapters.

In **Chapter 4** a novel method, T_2-adjusted computed diffusion-weighted imaging (T_2-cDWI), has been presented to synthesize images from diffusion-weighted images and T_2-weighted images from the same diffusion protocol. Phantom data and clinical examples show that T_2-cDWI has the ability to improve the image contrast between tumour and normal tissues.

Chapter 5 is allocated to the tumour segmentation methods. In particular the performance of two state-of the-art semi-automatic approaches, GrowCut and random walk, are investigated on clinical DWI images. The success of approaches in defining

the whole MPM disease volume and their diagnostic accuracies are tested on the patients.

Based on the segmented whole disease volume, two classification methods – global ADC thresholding and Gaussian mixture model - have been explored in **Chapter 6**, with the aim of distinguishing solid tumour from pleural effusion.

In **Chapter 7** the proposed segmentation and classification methods are applied to a clinical MPM cohort using optimised diffusion-weighted MRI to provide ADC and estimates of total volumetric tumour burden. The median ADC values and total solid tumour volume (TTV) of MPM is compared at 4 and 12 weeks after treatment with pre-treatment values in responders and non-responders defined by CT modified RECIST.

Chapter 8 summarises the findings of the thesis, and discusses possible future developments.

2 Literature review of treatment response assessment of MPM

This chapter is organised as follows: **Section 2.1** will introduce the special growth pattern of malignant pleural mesothelioma and the associated challenges. **Section 2.2** will survey the existing roles of CT and MRI for the management of MPM. **Section 2.3** will discuss the currently applied size measurement criteria (e.g. WHO, RECIST (Response Evaluation Criteria in Solid Tumours) and modified RECIST) for the assessment of treatment response. **Section 2.4** will discuss studies using volumetry on CT and MRI for treatment response assessment. Functional imaging techniques, such as positron emission tomography (PET), diffusion-weighted MRI and dynamic contrast-enhanced MRI (DCE-MRI) that may potentially improve the assessment of treatment response will be highlighted and discussed in **Section 2.5**. A chapter summary will be presented in **Section 2.6.**

2.1 A challenge for imaging: Special Growth pattern of MPM

As introduced in Subsection 1.1.1, malignant pleural mesothelioma grows on the pleural surface by the irregular rind-like tumours [8] and frequently extends to or invades the thoracic wall, the diaphragm, and/or the mediastinum [8-10]. The tumour can also spread along interlobar fissures across the mediastinum to the opposite pleura, or through the diaphragm into the peritoneum and/or adjacent organs [8] (**Figure 2.1).** Conventional size measurement criteria used to determine tumour burden, be it using bi-dimensional or uni-dimensional tumour diameters, assume a spherical tumour growth pattern, allowing approximation of tumour burden to be made. However, this assumption cannot be meaningfully applied in MPM because of the non-spherical growth pattern. This poses significant challenges for its diagnosis, staging and the assessment of tumour response.

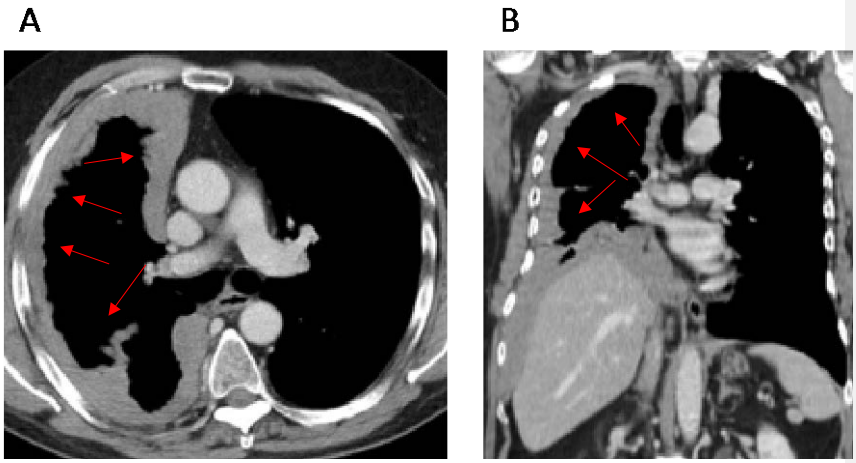

Figure 2.1: (A) Axial and (B) coronal reformat CT of a 52-year-old man with malignant mesothelioma of the right hemithorax (red arrows).

2.2 The roles of conventional CT and MR imaging

Currently, CT is routinely used for the diagnosis, staging, and treatment planning of MPM due to its wide availability and relatively low cost [25; 26]. At diagnosis, the main CT findings include unilateral pleural effusion, nodular pleural thickening and thickening of the interloblar fissure [27]. However, CT is limited for detecting early local tumour extension, including chest wall invasion, transdiaphragmatic spread and small lymph node metastases [28].

MRI has superior soft tissue contrast to CT. Compared with chest wall musculature, MPM returns moderately or slightly hyperintense signal on T1-weighted images and appears hyperintense on proton density and T2-weighted images [29]. Pleural effusions are low signal intensity on T1-wighted images and have high signal intensity on T2-weighted sequences. The visualisation of MPM may be further improved by using gadolinium-based MR contrast agent. On contrast-enhanced T1-weighted images, malignant pleural lesions often show contrast enhancement compared with intercostal muscles [30]. It has been found that contrast-enhanced T1-

weighted fat suppressed images are the most reliable for detecting tumour spread into the interlobar fissures and tumour invasion of adjacent structures, such as the chest wall and the diaphragm (**Figure 2.2**) [8; 31].

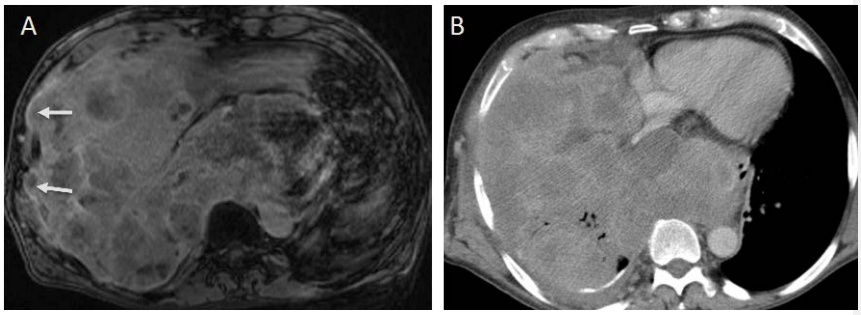

Figure 2.2: (A) Fat suppressed T1-weighted MRI and (B) CT in 49-year-old with malignant mesothelioma of the right hemithorax.

The MRI scan shows foci of chest wall invasion (arrows), which is more easily visualised compared with CT.

2.2.1 Benign versus malignant pleural disease differentiation

To explore the clinical role and limitations of MRI as the primary imaging for MPM, Knuuttila et al. [8] studied 13 confirmed mesothelioma patients and compared CT with MRI. It was shown that contrast-enhanced MRI, with its capability to produce multiplanar images, was superior to CT in indicating tumour infiltration of interlobar fissures, which is useful in the staging of early malignant pleural disease. Contrast-enhanced MRI was also better for showing chest wall changes and invasion of the diaphragm than axial CT. The author suggested MRI should be more commonly used when assessing tumour resectability and accurately evaluating extent of tumour.

Hierholzer et al. [30] performed a retrospective study involving 42 pleural disease patients to look for the role of MRI in the separation of benign from malignant pleural disease. High signal intensity with reference to intercostal muscles on T2-weighted

and/or contrast-enhanced T1-weighted images suggested malignant disease with a significantly high sensitivity (91%, 93% respectively) and specificity (80%, 73% respectively). When combining MR morphological features with the information on signal intensity, the sensitivity and specificity of MR in the detection of pleural malignancy were further improved. In this study MRI was also found to be superior to CT in indicating chest wall and diaphragmatic invasion.

2.2.2 Disease staging and assessing resectability

In a comparative study of MRI and CT for staging of MPM, Heelan et al. [31] evaluated 65 mesothelioma patients and found that CT and MR have similar accuracies (50-65%) for the staging. However, MRI was superior to CT for assessing invasion of the diaphragm, with accuracy of 82% and 55% respectively. For demonstrating endothoracic fascia involvement or solitary resectable foci of chest wall invasion, the accuracy was reportedly 46% for CT and 69% for MRI [31].

Patz [32] and colleagues compared CT with MRI in 41 patients and found that CT and MR were both sensitive in predicting resectability of mesothelioma along the diaphragm (sensitivity > 92%), while MRI was better than CT for evaluating the resectability at the chest wall [32]. By comparing MRI with surgical staging in 51 patients, Stewart et al. [33] found that MRI could still under-stage 50% of MPMs because of suboptimal detection of pericardial involvement or nodal involvement.

2.2.3 Assessment of tumour response to treatment

One of the most important roles of imaging is for the assessment of tumour response to treatment. The early identification of responders and non-responders is important in drug development and can help to stratify patient management, allowing precision treatment to be delivered in patients with MPM.

2.3 Assessing treatment response using size measurement criteria

2.3.1 WHO and RECIST

In the 1980s, the World Health Organisation (WHO) proposed using the product of the bi-dimensional tumour diameters as the basis for assessing tumour shrinkage after treatment [34]. This was further simplified by the Response Evaluation Criteria in Solid Tumours (RECIST) criteria in the 1990s, when a single maximum axial tumour diameter measurement was proposed [35]. More recently, the RECIST 1.1 criteria, a revision of the original RECIST, are being widely adopted as imaging end-point in clinical trials [36].

The main problem of applying these criteria to MPM is that these simplified measurements approximate tumour burden in cancers that typically exhibit a spherical pattern of growth. However, since MPM typically demonstrates a non-spherical growth pattern, it is often difficult to accurately categorize change in tumour burden using bi-dimensional or uni-dimensional tumour measurement [29]. One study evaluated the consistency of estimating disease volume by RECIST measurements [37] performed on geometric models. The study found that applying RECIST response criteria to a spherical tumour model resulted in partial response (PR) classification based on a 66% volume decrease and progressive disease (PD) based on a 73% volume increase. Using the mesothelioma model, RECIST criteria resulted in PR classification based on a 30% volume decrease and PD based on a 20% volume increase. Using RECIST for mesothelioma thickness measurements resulted in PR and PD classifications based on smaller volume changes compared with the spherical tumour model.

Not surprisingly, the limitations of bi-dimensional or uni-dimensional measurements for MPM are well-recognised. In one study that compared response assessment of MPM using either bi-dimensional WHO or uni-dimensional RECIST criteria, there

was a discrepancy of 27% in the assessment of treatment response depending on which criteria were applied [38]. Furthermore, measurement of individual pleural lesions was also subject to significant inter-observer variability, depending on how the diameters of each lesion were defined [39].

2.3.2 modified RECIST criteria

Byrne and Nowak [40] proposed the modified RECIST criteria for MPM in 2004, to take into account the changes in tumour bulk across the affected thorax. The modified RECIST criteria are still based on using a uni-dimensional tumour diameter, but these are measured perpendicular to the chest wall or the mediastinum. In each patient, six measurements are acquired in total, two at any particular slice of the thorax and three different slices at least 1cm apart from each other, are assessed on the CT (**Figure 2.3**). These measurements are then summated and compared between two occasions 4 weeks apart. It is noteworthy that these measurements should be acquired at similar levels and positions in the same patient at each CT study.

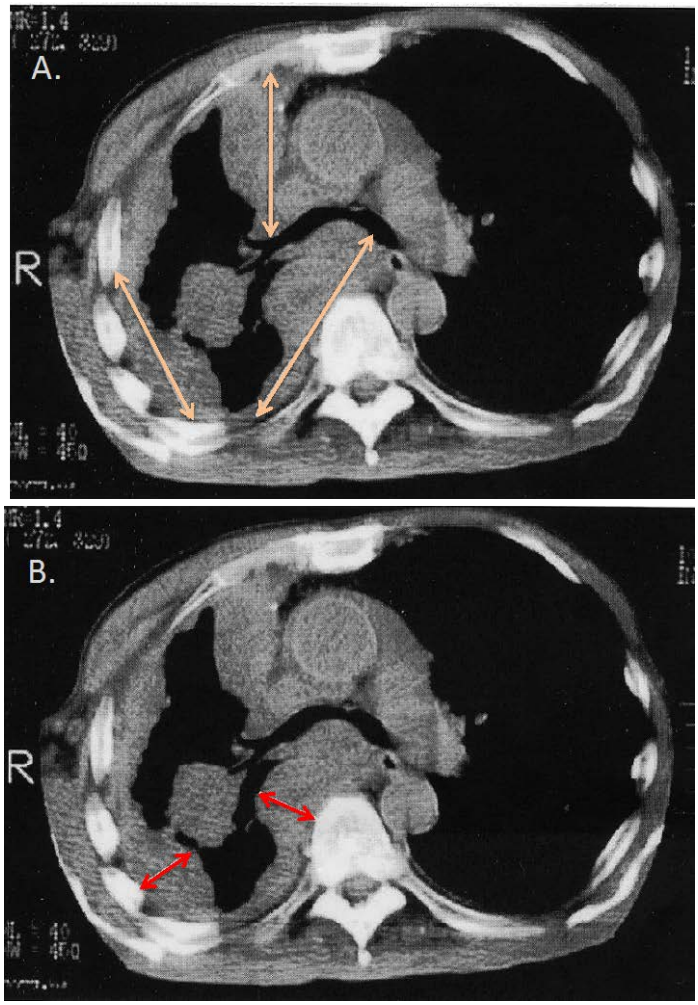

Figure 2.3: Example measurements are illustrated on one axial CT image, according to the (A.) RECIST (Orange arrows) and (B.) modified RECIST criteria (Red arrows).

Image from M.J. Byrne and A.K. Nowak, 2004

In an attempt to be more specific about how measurements are acquired using RECIST or modified RECIST criteria to reduce intra-observer and inter-observer variability, guidelines have been published on the application of such criteria on CT

[41; 42]. These practical steps go some way towards increased consistency of pleural disease measurement, but do not entirely eliminate the problems associated with selection/ measurement bias in the choice of target lesions or the site of measurements, which may show differing degrees of tumour enlargement/ regression with treatment. In one recent study [43] evaluating observer variability in the measurement of mesothelioma tumour thickness, it was found that the mean range of variability was 15.1% of the mean per-site measurement. It may be possible in future to reduce the definition of minimally measurable disease from 10mm to 5 or 7.5mm in MPM, but this would clearly require further validation.

A number of clinical trials conducted in MPM using the modified RECIST criteria have found good correlation with clinical outcomes. In one study of 50 patients with MPM, 28 patients showed partial response, 12 patients showed stable disease and 10 patients showed progressive disease at early therapy response (after three of six chemotherapy cycles) evaluation with patient follow-up examination (after six chemotherapy cycles) as the reference standard [44]. Using modified RECIST response criteria, the responses of all patients were classified similarly to the reference standard, whereas there were four cases of mismatch using RECIST criteria (partial response versus stable disease). Modified RECIST showed a higher inter-observer agreement compared with RECIST criteria (kappa = 0.9-1.0 vs. 0.7-1.0). In another study, which performed pooled analysis of data from 716 patients from nine MPM clinical trials [45], tumour response was evaluated by either modified RECIST or WHO criteria. Despite the inherent limitations of size measurement criteria, the study found that patients who had partial response (12.8 months) or stable disease (9.4 months) following chemotherapy were associated with significantly longer overall survival compared with patients who had disease progression (3.4 months). Although unusual, a complete disappearance of disease on CT has been reported with patients treated with chemotherapy [46; 47], these were associated with prolonged survival.

2.4 Response assessment using volumetry on CT and MRI

Disease burden before and after treatment has been measured by volumetry on CT or MR images with encouraging results [19; 44; 48-50]. These studies applied segmentation techniques to the CT or MR images to estimate the total amount of disease present within a hemithorax. In a study of 57 patients with MPM treated with chemotherapy, response assessment was evaluated by CT volumetry, WHO and modified RECIST criteria [48]. The authors found that objective response defined by CT volumetry best correlated with patient survival compared with WHO or modified RECIST criteria. Using one particular segmentation technique, CT volumetry was found to have a higher inter-observer reliability and agreement compared with modified RECIST criteria [19]. In a more recent study of serial CT scans in 81 patients with MPM, a change in CT disease volume after treatment was found to be a significant predictor of patient survival in multivariate analysis, along with histopathological subtype, patient performance status and the degree of dyspnoea [50]. An increase in disease volume was found to be a significant predictor of poor patient outcome in both univariate and multivariate analysis [50].

Another approach in volumetric assessment has been the measurement of lung volume rather than the pleural disease as a surrogate for treatment response. In a study of 61 patients with 216 CT scans, measurements of pleural disease by modified RECIST and CT volumetry were undertaken. In addition, the lung volume of the affected hemithorax was also segmented and normalized to the contralateral lung, to account for differences in the degree of inspiration between studies [51]. The authors found a negative correlation between changes in normalized lung volume and changes in pleural disease volume, while a positive correlation was found between modified RECIST linear tumour measurements and the CT disease volume. An increase in linear tumour thickness, increase in disease volume and decrease in lung volume were independently associated with poor patient prognosis [51].

Table 2.1: comparisons of different size-measurement criteria [34-36; 40].

Criteria	
WHO	Up to 5 measureable lesions
RECIST	Up to 5 lesions per organ (up to 10)
RECIST 1.1	Up to 2 lesions per organ (up to 5)
Modified RECIST	Tumour thickness at 2 positons/ slice and 3 CT slices in total

2.5 Response assessment using functional imaging techniques

Recognising the inherent limitations of size-based tumour response criteria, particularly in the context of MPM, there is considerable interest in using functional or molecular imaging techniques to assess treatment effectiveness. Functional imaging techniques are applied to derive quantitative measurements of tumours, which reflect particular aspects of the tumour pathophysiology. By quantifying how these measurements change with treatment, it is possible to observe treatment effects.

Functional imaging techniques that appear relevant to MPM include 18F-Fluorodeoxyglucose (18FDG) positron emission tomography (PET), diffusion-weighted MR imaging and dynamic contrast-enhanced MRI (DCE-MRI). The biological underpinning of each technique, the quantitative measurements derived and the evidence for its application in MPM are discussed below.

2.5.1 18FDG-PET imaging

18F-Fluorodeoxyglucose is a glucose analogue, and its uptake into tissues is a marker for glucose metabolism. In general, tumour tissues show an increased uptake of 18FDG tracer compared with background or normal tissues, thus enabling plaques or foci of MPM to be recognized on imaging. Not surprisingly, 18FDG-PET has been found to be superior to CT for disease localization and staging, and for surgical decision-making [52-56]. 18FDG-PET is also more sensitive for the detection of

nodal, chest wall invasion and distant metastases [57-59], as well as port-site disease [60]. More recently, PET imaging has also been adopted to guide radiation therapy planning [61; 62].

The degree of 18FDG uptake on PET imaging can be measured semi-quantitatively (e.g. using the maximum standardized uptake value, SUVmax), or using more robust quantitative measurements that are derived using more prescribed data acquisition and analysis (e.g. PET Response Criteria in Solid Tumors (PERCIST) [63]), with the aim of reducing measurement variability between studies [63].

There is now compelling evidence that 18FDG-PET imaging can provide prognostic information in patients with MPM. Studies using 18FDG-PET have found that patients with higher tumour SUV values were associated with shorter disease survival [58; 64; 65], which may be linked to the underlying histopathological features (e.g. pleomorphic subtype of epithelioid MPM and non-epithelioid tumours) [66]. In one retrospective study of 177 patients, multivariate analysis found that a tumour SUV_{max} > 5 was significantly associated with poorer patient prognosis [67].

However, the evidence for the use of 18FDG-PET for the assessment of treatment response in MPM appears more uneven. On the encouraging side, one study which defined a decrease of 25% or more in the SUVmax as metabolic response, found that metabolic response was associated with a median time to progression of 14 months [68] for responders versus 7 months for non-responders (P = 0.02). Patients with a metabolic response also had a trend towards longer overall survival. Several studies also found volumetric parameters derived from the PET imaging, such as the total glycolytic volume, metabolic tumour volume or total lesion glycolysis to be useful for response assessment and for patient prognostication [69; 70] (**Figure 2.4**). In another study of 23 patients, who underwent CT and 18FDG-PET imaging, the total glycolytic volume of MPM was analysed before and after chemotherapy [49]. After one cycle of chemotherapy, Cox regression analysis showed a statistically significant correlation between decrease in total glycolytic volume and improved patient survival (P = 0.015). However, neither a reduction in the maximum standardized uptake value (P = 0.097) nor CT linear measurements (P = 0.131) demonstrated a statistically significant association with patient survival. In a further study [71], multivariate

analysis found that the metabolic tumour volume (HR 1.003, P = 0.025) and total lesion glycolysis (HR 1.001, P = 0.031) were independently associated with tumour progression. The time to tumour progression was shorter in patients with a high metabolic volume on PET imaging.

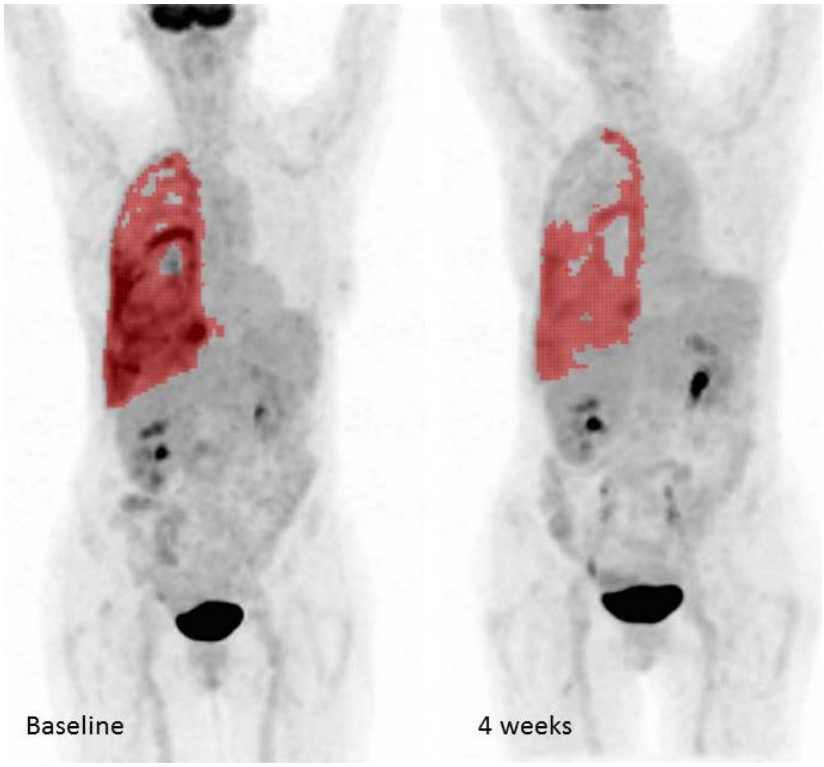

Figure 2.4: Baseline and 4 weeks post-treatment 18FDG-PET maximum projection images in a 54 years old woman with sarcomatoid mesothelioma showing good response to therapy.

The pleural tumour segmented volumes (shown in red) reduced from 938.88 to 540.42 cm^3 and the total lesion glycolysis from 2667.90 (g/ml) to 1194.24 (g/ml) after treatment.

One study was, however, less encouraging. In this study, MPM patients were treated with pemetrexed and platinum-based chemotherapy and FDG-PET/CT imaging was performed within 2 weeks before starting treatment and after every three cycles of chemotherapy. The CT images were evaluated using modified RECIST criteria, while the FDG-PET/CT images were analysed using SUV_{max} change in the total lesion glycolysis and the metabolic tumour volume. The authors found that the SUV_{max} showed a high degree of variance over time for individual patients and that changes in SUV_{max} did not predict for the patient overall survival. By contrast, morphological response on CT by modified RECIST had the highest correlation with overall survival and predicted survival up to the 15^{th} cycle of continued permetrexed and platin-based chemotherapy treatment [72]. This study also illustrates the need for meticulous 18FDG-PET data acquisition and analysis to minimize inter-study measurement variability, which is not related to drug effects. In this regard, the adoption of a more standardized and robust approach to these studies (e.g. using PERCIST criteria), should be encouraged particularly in the setting of multicentre clinical trials.

It is also important to keep in mind that in patients who have undergone talc pleurodesis, caution will need to be exercised towards the interpretation of 18FDG-PET imaging because pleurodesis can induce an increase in the SUVmax values [73], which should not be misinterpreted as disease worsening.

2.5.2 Diffusion-weighted MRI

The mechanism of contrast for diffusion-weighted MRI (DWI) is based on differences in the mobility of water between tissues. Water molecules in unrestricted environments exhibit random thermal motion (Brownian motion, or free diffusion), while the motion of water molecules in tissues is impeded by structural barriers, such as cell membranes and macromolecules.

The signal intensity measured on DWI is sensitive to the net displacement of water molecules following the application of a pair of MR diffusion-sensitizing gradients [21]. In tissues where there is a greater barrier to the movement of water molecules (e.g. mesothelioma tumours), the DWI signal is usually higher compared with areas

with free water (e.g. pleural effusion) or normal tissues (e.g. lung and chest wall), thus enhancing the visual detection of solid cellular disease against the background tissues (**Figure 2.5**). Recently, the use of visual assessment on DWI of pleural thickness, lung shrinkage (**Figure 2.6**) and pleural pointillism (**Figure 2.7**) in particular, have been found to be useful for the diagnosis of pleural mesothelioma [74].

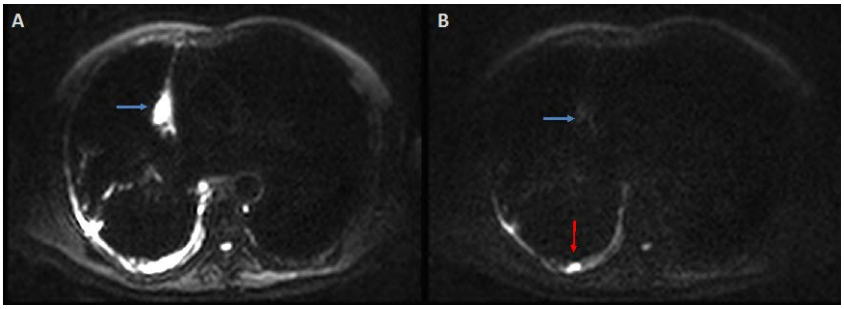

Figure 2.5: DWI images of (A.) b at 100 mm^2/s and (B.) b at 800 mm^2/s of a 69-year-old male who has malignant pleural mesothelioma. The mesothelioma tumour (red arrow) is more hyperintense than the pleural effusion (blue arrow) on the high-b-value DWI image.

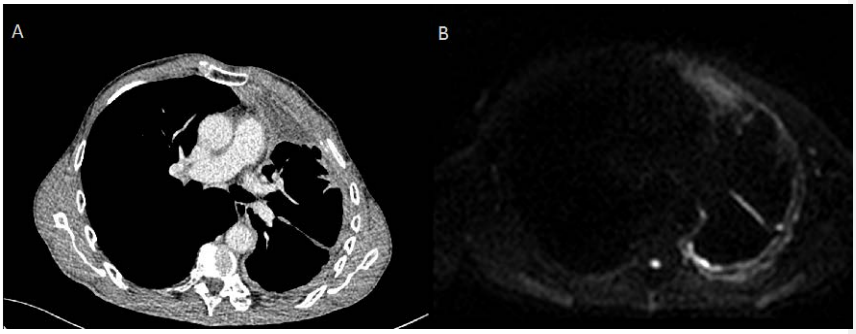

Figure 2.6: (A.) CT and (B.) DWI images of b at 800 mm^2/s of a 69-year-old male with mesothelioma in the left lung. Both CT and DWI images show the shrinkage

of the left lung while DWI further indicates the pleural thickening of the left lung.

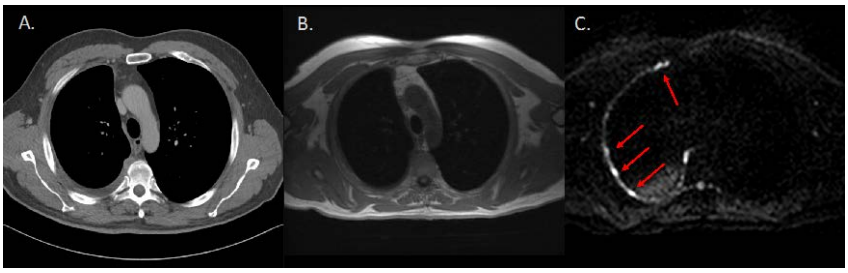

Figure 2.7: A 60-year-old man with right-sided MPM. (A.) CT and (B.) T1-weighted MRI show right-sided pleural thickening with shrinking lung sign. (C.) DWI (b = 800 s/mm^2) shows a sign of pointillism such as multiple speckled hyperintense pleural spots (red arrows), which are most likely caused by small multifocal deposits of tumours.

In addition, water diffusion in tissues has been shown to be inversely related to tissue cellularity and the integrity of cell membranes [20; 21; 23], and this degree of water mobility in tissues can be to be quantified in DWI by calculating the apparent diffusion coefficient (ADC) based on the gradient of attenuation with increased diffusion weighting [2] (Described in detail in Section 3.3). [22]. Based on this principle, ADC has been shown to significantly increase in disease sites that respond to chemotherapy, radiotherapy, novel therapeutics and embolization treatment across a variety of tumour types [75-79]. Hence, DWI appears to be an attractive tool to aid tumour detection/ visualization and for the assessment of treatment effectiveness or failure [80]. **Figure 2.8** shows typical DWI images and ADC map in a patient with malignant pleural mesothelioma.

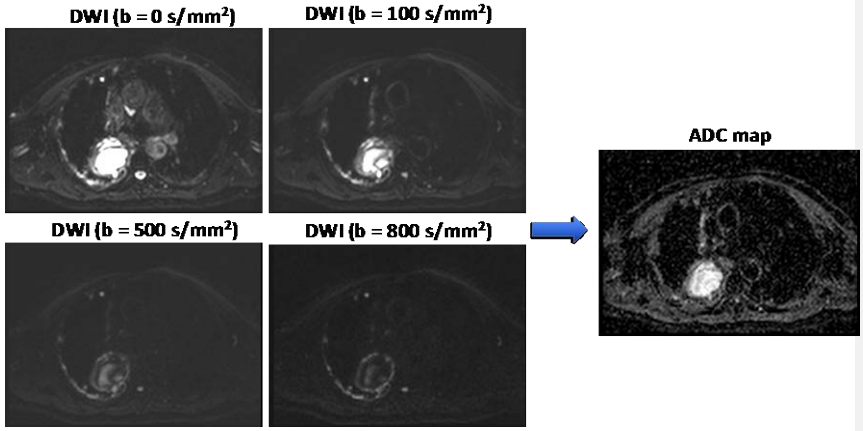

Figure 2.8: The DWI images at multiple b-values and the derived ADC map of a 74-year-old male patient with malignant pleural mesothelioma in the right lung comprising both cystic and solid disease.

As ADC measurements are linked to tissue cellularity, it has been found that the ADC values may help to distinguish between benign and malignant pleural nodules. Coolen et al. [81] found that the ADC value of malignant pleural disease (1.40×10^{-3} mm²/s) was significantly lower than that of benign lesions (2.49×10^{-3} mm²/s). When applying a threshold ADC value of 1.52×10^{-3} mm²/s to differentiate benign from malignant pleural disease, the sensitivity, specificity, and accuracy were 71.4%, 100% and 87.1%, respectively. Using DCE-MRI parameters to correct wrongly diagnosed cases where ADC was between 1.52 and 2.00×10^{-3} mm²/s, the result could be improved to 92.8% sensitivity, 94.1% specificity and 93.5% accuracy, respectively. DWI supplemented with DCE-MRI may be a promising tool in diagnosis of malignant pleural disease.

ADC value has also been found to differ between different histopathological subtypes of MPM, as different subtypes are different in cellularity, the higher microvascular density, micronecrosis, and cell oedema of the sarcomatoid subtype may lead to restricted water diffusion in tumours, which could be detected by DWI [2]. The reason to develop a non-invasive diagnosis of tumour subtypes is because the epithelioid

MPM has a better prognosis than the other two subtypes (sarcomatiod and biphasic) [82; 83], distinguishing histologic subtypes may thereby inform on tumour aggressiveness and patient prognosis. Gill et al. correlated the ADC values of three histological subtypes of MPM in 62 patients [2]. The ADC values for epithelioid, biphasic and sarcomatoid were (1.31±0.15) × 10^{-3}, (1.01±0.11) ×10^{-3} and (0.99 ±0.07) ×10^{-3} mm^2/s, respectively, with the poor prognosis sarcomatoid tumours returning the lowest ADC value. When the threshold ADC value was 1.1×10^{-3} mm^2/s, the sensitivity, specificity and accuracy to distinguish epithelioid with sarcomatiod subtype were 60%, 94% and 84%, respectively. However, there is significant overlap in the ADC values between the histological subtypes, which can make it difficult to prospectively prognosticate individual patients based on single ADC measurements.

ADC has also been used to assess the type of pleural effusion and help in the differential diagnosis of pleural effusions. Baysal et. al evaluated fifty-seven patients with pleural effusion using diffusion-weighted imaging and found that the mean ADC values are 3.42±0.76 ×10^{-3} and 3.18±1.82×10^{-3} mm^2/s for transudates and exudates respectively. A sensitivity of 90.6% and specificity of 85% were found using the optimum cut-off ADC of 3.38× 10^{-3} mm^2/s [84]. Inan et. al has shown that exudative effusion has a significant lower ADC than transudative effusion: the mean ADC values for the exudative and transudative effusions were (3.3±0.7) ×10^{-3} and (3.7±0.3) ×10^{-3} mm^2/s respectively [85]. A threshold ADC value at 3.6 × 10^{-3} mm^2/s has been described to differentiate transudative from exudative effusion with 71% and 63% of sensitivity and specificity, respectively [85]. It is worth noting that these reported ADC values of effusions are higher than the ADC of water at 37 degree (3.2×10^{-3} mm^2/s), which indicates challenges in obtaining accurate ADC are the bulk motion of fluids caused by the respiratory.

The evidence for the use of DWI for the assessment of treatment response is still being accrued [86], and there are to date no published trials evaluating the value of DWI or ADC for treatment response assessment in MPM. Nonetheless, there is emerging data for the potential of DWI to provide objective quantification of disease burden and tissue cellularity before and after treatment. The ability of DWI to highlight cellular malignant pleural disease from pleural fluid and background normal

tissue provides us with the ability to segment solid pleural disease using a semi-automatic algorithm, to provide an estimate of the total diffusion volume in patients with MPM. In addition, it is also possible to evaluate the ADC values associated with the diffusion volume, thereby monitoring the cellularity of the disease following chemotherapy or radiotherapy. It is expected in responders to treatment that the diffusion volume would decrease and the ADC value increase (**Figure 2.9**). It is worth noting that in the case in **Figure 2.9** the total disease burden includes pleural effusion and solid lesions, and the reduced total disease volume after treatment also implies an increase in the left lung volume, which is a significant predictor of patient survival discussed in Section 2.4.

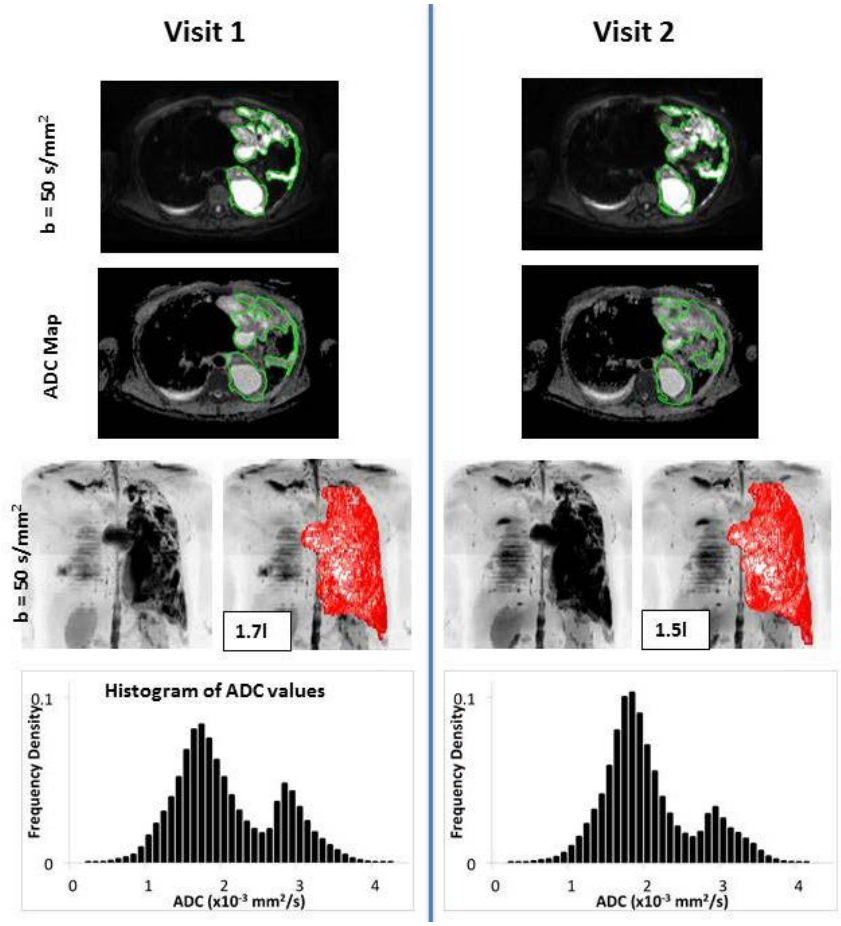

Figure 2.9: Diffusion MR volumetry and tumour ADC of one MPM patient.

Pre- and post- treatment diffusion-weighted MRI of the thorax were performed in a patient with malignant pleural mesothelioma, which enabled the disease to be segmented and derive the total tumour volume. The histogram distribution of the apparent diffusion coefficient associated with this volume is also shown. In this case, note the slight reduction in total tumour volume following chemotherapy.

2.5.3 Dynamic contrast-enhanced MRI (DCE-MRI)

Dynamic contrast-enhanced MRI is performed by tracking the signal changes following the passage of an intravenous injection of gadolinium-based MR contrast agent through a tissue, by rapid and sequential imaging through a region of interest. As a high rate of temporal data sampling is required to observe contrast kinetics through tissues, this often limits the spatial coverage of the technique, such that only a proportion of the pleural disease can be studied after a single contrast injection.

The time-course of the signal intensity change within the tissue of interest after contrast injection can be used to derive vascular parameters that reflect vascular flow and permeability [87; 88]. As the contrast agent diffuses passively between intravascular and extracellular spaces, one of the ways to quantify differences in microcirculation and vascular permeability is extended Toft's bi-compartmental mathematical model [3]. Typical parameters that can be derived include the forward rate constant (K^{trans}), rate constant (k_{ep}) and extracellular extravascular volume (v_e) and changes in these parameters can be monitored in response to treatment (**Figure 2.10**).

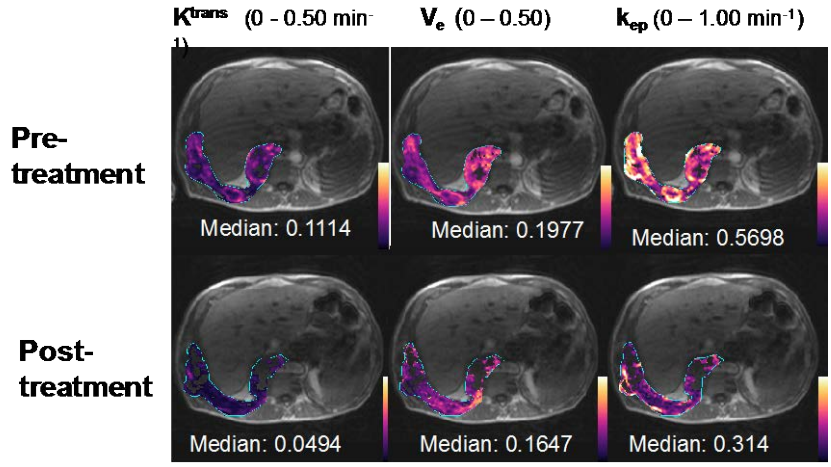

Figure 2.10: Dynamic contrast-enhanced MRI performed before and after treatment with a novel therapeutic in a patient with malignant mesothelioma.

Quantitative analysis results in parametric maps of the volume-transfer constant (K^{trans}), rate constant (k_{ep}) and extracellular extravascular volume (v_e). Note the reduction in median values of all three parameters after treatment.

Giesel et al. [87] found that it was possible to differentiate malignant pleural tumour from normal tissues by measuring the pharmacokinetic vascular parameters. In a therapeutic follow-up study [87], DCE-MRI was performed in MPM patients prior to treatment (n = 19), after the third cycle (n = 12), and sixth cycle (n = 7) of chemotherapy to assess the tumour microvascular properties and to predict therapeutic outcome. Clinical non-responders, characterized by short median survival (460 days), had significantly higher k_{ep} values (3.6 min^{-1}) than responders (2.6 min^{-1}) with longer median survival (780 days), because a more heterogeneous tumour, observed with more hot spots defined by a rapid initial uptake of contrast, might not respond well to chemotherapy. The study showed that a high pre-therapeutic k_{ep} value within MPM was correlated with a poorer overall response following chemotherapy, but this requires a further validation due to the relative small sample population of this study. Interestingly, vascular parameters derived by DCE-MRI have also been

found to show moderate positive correlations with microvessel density (MVD) (r = 0.5) [89].

Table 2.2: a summary of the quantitative imaging modalities (PET/CT, DWI, and DCE-MRI) for malignant pleural mesothelioma and their functional parameters.

Technique	Biophysics basis	Quantitative parameters
FDG-PET	Metabolism, cell proliferation and apoptosis	SUVmax
DWI	Cellularity and tortuosity of interstitial space	ADC
DWI (IVIM)	Blood flow and tissue diffusivity	f, D, D*
DCE-MRI	Blood flow and tissue permeability	K^{trans}, v_e, k_{ep}, AUC

2.6 Chapter Summary

Despite the known limitations of size measurement response criteria in MPM; WHO, RECIST (1.0 and 1.1) and modified RECIST criteria are still widely used in clinical trials of MPM. This may be because these measurements are relatively simple to undertake, and when performed meticulously, can yield meaningful results that inform on patient outcomes. Nonetheless, current evidence suggests that using the modified RECIST criteria is associated with a lower degree of inter-study and inter-observer variability.

There are data to support CT and MRI volumetry for the assessment of treatment response in MPM. However, these techniques are more time consuming to undertake, may have to be performed offline, and may require the help of clinical scientists for optimal image segmentation. Furthermore, due to the inherent lower contrast between solid and fluid pleural disease on CT, it may not be easy to distinguish between the two. The emerging evidence for the use of volumetric analysis is encouraging, both

for the direct assessment of pleural disease; as well as for the assessment of the underlying lung volume as potential surrogates for treatment response.

As imaging in oncology becomes increasingly quantitative, functional imaging techniques which can quantify various aspects of the tumour pathophysiology will become more important. In MPM, there is now a body of literature showing the predictive and prognostic value of 18FDG-PET imaging, and for the assessment of tumour response to treatment. However, it would appear that measurement variability in a multicentre setting may be an issue, which would need to be addressed in a concerted way in future PET imaging studies.

Of the available MRI techniques, DWI appears to be most promising as the technique is relatively quick to perform and does not require the administration of any exogenous contrast agent. The ADC value quantified from DWI has been shown to reflect tissue cellularity, and may provide prognostic information. Trials in other tumour types have shown that ADC has good measurement reproducibility, and a significant increase in ADC values is observed in responders to treatment. Clearly, clinical trials using DWI needs to be undertaken in MPM to investigate diffusion volume and the associated global tumour ADC values as potential response, predictive and prognostic biomarkers.

As a general note, imaging research published in the medical literature has been patchy in addressing the wider validation and translation of potential imaging biomarkers. There is now recognition and acknowledgement within the imaging research community that this process has to be actively pursued to enable promising techniques to be translated and applied to daily clinical practice and research [90]. There is a clear need for standardization of the functional MRI sequences and collaborative multicentre studies to enable a larger number of patients to be evaluated using these newer imaging techniques; and the importance of building a test cohort and a validation cohort as part of the imaging biomarker development should always be kept in mind and emphasized [91].

This chapter is based on the publication: Cheng, L., Tunariu, N., Collins, D.J., Blackledge, M.D., Riddel, A.M., Leach, M.O., Popat, S., and Koh, D.M., 2015.

Response evaluation in mesothelioma: Beyond RECIST. ***Lung Cancer, 90,*** **pp.433-441.**

3 Background of Diffusion Weighted Magnetic Resonance Imaging

In this chapter, the fundamental principle which this dissertation relies upon is described. Firstly, a brief background on the basic theory of nuclear magnetic resonance (**Section 2.1**) is presented. Then, the underlying physics in image acquisition and formation of MRI and DWI is discussed (**Section 2.2**) and the key factors and related artefacts in body DWI are outlined (**Section 2.3**). The ultimate goal of this chapter is to provide a building-block for the upcoming chapters.

3.1 Theory of NMR

MRI is based on the principle of nuclear magnetic resonance (NMR) [92; 93], which was first introduced by Bloch and Purcell in 1946. The reference of this section is [94] .

3.1.1 Nucleus Spin

MRI signals are generated through the interaction between the magnetic properties of hydrogen nuclei, external magnetic fields and pulsed electromagnetic waves. Nuclei have an angular momentum $\boldsymbol{I}$, known as 'Spin', which yields a magnetic moment $\boldsymbol{\mu}$ of the nucleus. Their relationship is defined by the following equation:

$$\boldsymbol{\mu} = \gamma * \boldsymbol{I}$$

where $\boldsymbol{\mu}$ is the magnetic moment of the nuclei, γ is the gyromagnetic ratio of the nucleus, and a constant for each nucleus (For the proton γ is 42.58 MHz/T), and $\boldsymbol{I}$ is the angular momentum of the nuclei, given by:

$$I = \hbar\sqrt{s(s+1)}$$

where $\hbar$ is Planck's constant, and s is the spin number. The magnetic moment enables the interaction of the particle with an external magnetic field.

Spin numbers are different according the different types of nuclei:

- If the number of neutrons and the number of protons are both even, the nucleus spins cancel out, hence no net spin.
- If the number of neutrons plus the number of protons is odd, the nucleus spin is a half-integer. (either -½ or +½ for hydrogen depending on the magnetic moment orientation).
- If the number of neutrons and the number of protons are both odd, the nucleus spin is an integer.

Table 3.1: Net nuclear spin numbers, γ and relative sensitivity for example nuclei.

Nuclei	Unpaired Protons	Unpaired Neutrons	Net Spin	γ (MHz/T)	Sensitivity [1]
^{1}H	1	0	1/2	42.58	100
^{13}C	0	1	1/2	10.71	1.59
^{19}F	1	0	1/2	40.08	83.3
^{23}Na	1	2	3/2	11.27	9.25
^{31}P	1	0	1/2	17.25	6.63

Hydrogen with the net spin of ½ and a high nuclear gyromagnetic moment ratio is the main molecule used in the clinical MRI. This is due to the fact that water, containing two hydrogen atoms for every oxygen, accounts for 60% of human body, hence, the spins mentioned in the rest of this thesis refers to hydrogen spins.

Nonetheless, when there is no strong external magnetic field applied, all the spins in the human body are randomly oriented and cancel each other, therefore, the net magnetic moments of the body are zero.

[1] Relative sensitivity (signal strength as compared with hydrogen) for the same number of nuclei at constant field strength as a percentage of sensitivity for 1H. Source: Data from James, T. L. Nuclear Magnetic Resonance in Biochemistry. New York, Academic Press, 1975.

In the presence of a strong external magnetic field B_0 with the direction of the magnetic field along the z-axis, the spins magnetization vector, M,[2] will align itself with the field and the spins will precess around B_0. The spins have two energy states, spin up state (the lower energy state, I = 1/2) and spin down state (higher energy state, -I = -1/2). The difference between the two energy states is proportional to the strength of the applied magnetic field:

$$\Delta E = \gamma h B_0$$

Where γ is the gyromagnetic ratio (unit: MHz/T), h is Plank's constant, B_0 is the magnetic field strength (unit: Teslas).

Notably, spins in the lower energy state can be excited to the higher energy state if absorbing an external photon or external magnetic field that has energy equal to the energy gap ΔE.

[2] As the signal of one spin is impossible to measure, in general spins are considered as an ensemble and are described in terms of precession around a spin magnetization vector, M (see more details in section 3.1.2 and 3.1.3).

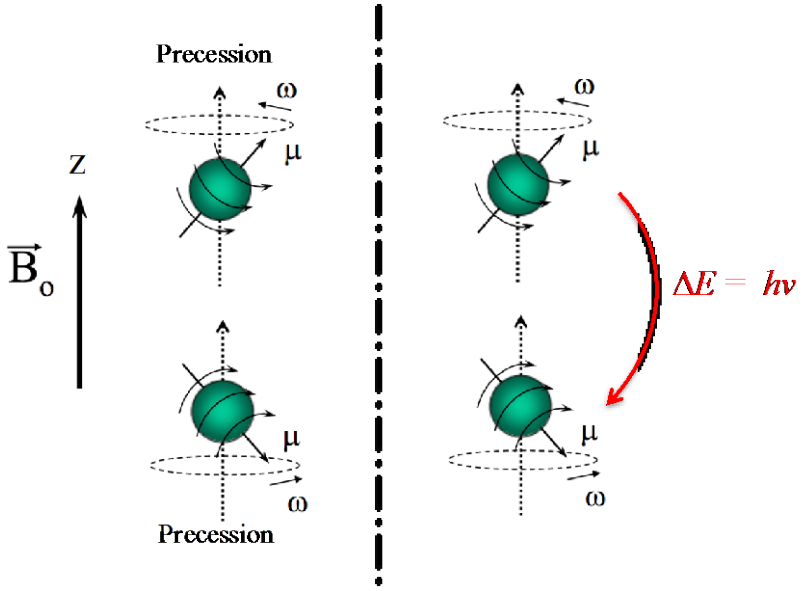

Figure 3.1: (Left) A graphical representation of proton spin for both spin-up (Upper) and spin-down (Lower) particles. The resultant magnetic moment, μ, is opposite in direction for the two spins. (Right) The graph illustrates the lower energy proton is excited to higher energy after absorbing the energy ΔE.

3.1.2 Bulk Magnetization

In MRI, a group of spins experiencing the same magnetic field are observed instead of individual spins. For a group of spins in a small volume (such as a voxel) in an external magnetic field, more spins are in the spin-up state. Bulk magnetization describes this situation such that a group of spins give a net contribution of the magnetic moments in the presence of an external magnetic field. It is proportional to the strength of the magnetic field and can be characterized as the magnetization vector ***M*** with components in the x, y and z directions:

$$\boldsymbol{M} = \begin{bmatrix} M_x \\ M_y \\ M_z \end{bmatrix}$$

At equilibrium, the non-zero net magnetization vector will align with the external field $\mathbf{B_0}$, and is called the equilibrium magnetization $\mathbf{M_0}$. If $\mathbf{B_0}$ is applied along the z-axis, the longitudinal magnetization $\mathbf{M_z}$ is equal to $\mathbf{M_0}$ at equilibrium, while the transverse ($\mathbf{M_x}$ or $\mathbf{M_y}$) magnetization is zero.

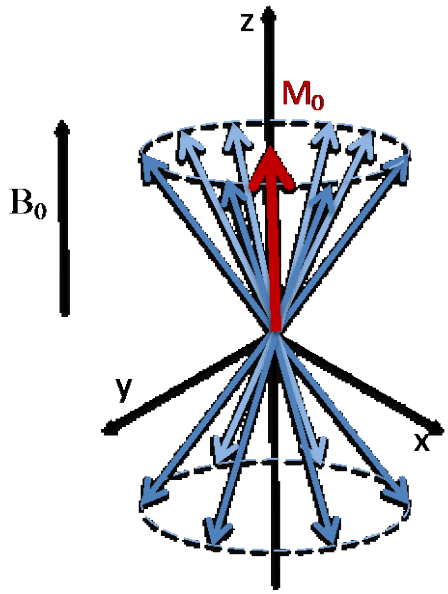

Figure 3.2: Diagram indicates excess alignment of spins with B_0 to form the net magnetization M_0. Conventional designation of Cartesian dimensions is also shown.

3.1.3 Precession

Due to the angular moment of the proton, the nuclear magnetic moment will not be kept exactly in the same direction as the external magnetic field, the spins will precess around the B_0 field axis. This is called precession and the precession frequency is known as the Larmor frequency:

$$\omega_0 = \gamma B_0$$

where ω_0 is the angular frequency of the precession, B_0 is the strength of the applied external magnetic field, and γ is the gyromagnetic ratio for the proton. For clinical MRI scanners with the field strength of 1.5 or 3 Tesla, all the hydrogen nucleus in the patients placed in the scanner precess at the Larmor frequencies of 63.87 and 127.74 MHz respectively, in the axis of the magnetic field.

It is worth noting that nuclei surrounded by many electrons (such as hydrogen atoms in fat molecules), experience a lower applied effective magnetic field due to the electron shielding effect, hence, it has a lower Larmor frequency than hydrogen atoms in water. This difference in resonance frequency are known as the chemical shift, defined in parts per million (ppm) and is independent of the spectrometer frequency.

$$\delta = \frac{\omega - \omega_{ref}}{\omega_0} \times 10^{-6}$$

where ω is the Lammor frequency of the imaged species, ω_{ref} is the reference Larmor frequency of a substance (such as Tetramethylsilane, TMS, for ^1H), and ω_0 is the operating frequency of the scanner.

The difference in the resonance frequencies of different nuclei may cause chemical shift artefacts in MRI images and will be discussed in subsection 3.3.6.

3.1.4 RF Pulses in MRI

It is impossible to directly detect the bulk magnetization *M* of protons in a magnetic sample when *M* is in the same direction as the applied magnetic field B_0. The magnetization must be re-oriented into the transverse plane to be detected. This can be accomplished by applying an RF pulse (typically less than or equal to 90 degree). In the presence of the induced external magnetic field, the RF coil produces an oscillating magnetic field. This oscillating magnetic field is called the B1 magnetic

field. The net magnetisation of the isochromat,[3] is in a function of B_0 and B_1 and is described by the Bloch equation (ignoring relaxation effects):

$$\frac{dM(t)}{dt} = \gamma M(t) \times (B_0(t) + B_1(t))$$

As described in **subsection 3.1.1**, spins in the lower energy state can be excited to the higher energy state if the absorbing energy meets the energy difference between the two spin states. Assuming that B_1 field is in the x-y plane with the same frequency as the Larmor frequency ω_0 of spins within the B_0 field, some lower energy protons will absorb energy from the oscillating electromagnetic wave and flip into the higher energy state. If the 90-degree pulse is applied over a short enough timescale, and assuming the B1 is uniform over the sample, $\boldsymbol{M_z}$ will go down to zero as the opposing components from the two energy states cancel each other out. Meanwhile, as the pulse is short, all the protons will be in phase, and the net magnetisation vector $\boldsymbol{M}$ will rotate around the direction of B_1 at the Larmor frequency (ignoring relaxation effects, discussed in Section 3.1.5). This is called transverse magnetisation $\boldsymbol{M_{xy}}$.

[3] An isochromat is a small volume which contains a small group of spins, and all the spins within this volume experience the same magnetic field and resonate at the same frequency.

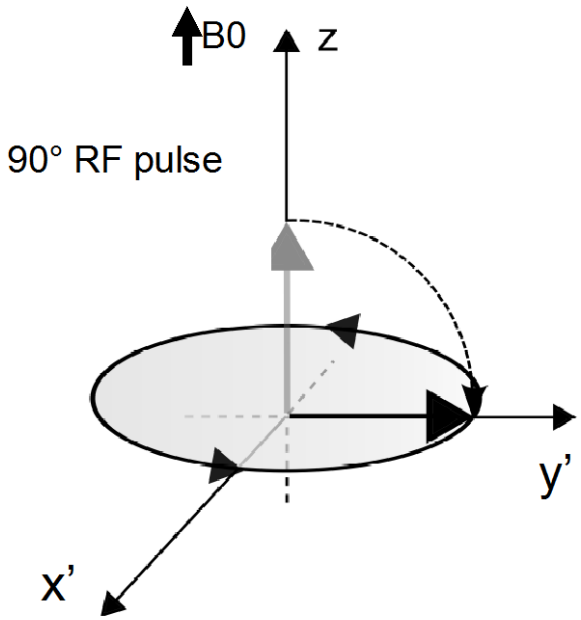

Figure 3.3: a 90-degree RF pulse with Larmor frequency flips the net magnetisation vector *M* to y' axis in the rotating frame of reference rotating about z at the resonance frequency (Assume B0 is along Z and B1 is along x' axis).

Image from http://zerpoii.opentronix.com/?p=1148

This oscillating magnetic wave is considered to be radio frequency (RF) pulse as its frequency (the RF frequencies would be in the range of 64 and 128 MHz at 1.5T and 3.0T scanner, respectively) falls into the range of radio waves in the electromagnetic spectrum. The flip-angle between ***M*** and the external B_0 filed (usually in z-axis) is dependent on the magnitude and duration of the RF-pulse given a strong and rectangular RF pulse:

$$\alpha = f_1 * t_p = \gamma * B_1 * t_p$$

where α is the flip angle of the RF pulse, γ is the gyromagnetic ratio, and B1 is the magnitude of the RF pulse, t_p is the duration of the RF pulse and is typically of the order of a few microseconds.

The described case of a 90° flip angle, is referred to as a 90° RF pulse and is one of the most commonly used RF pulse in clinical MRI. The other commonly used is referred to as a 180° RF pulse, and will flip the equilibrium $\boldsymbol{M}$ 180° from z axis to –z axis.

3.1.5 Relaxation

After the RF pulse has been removed, spins return to their equilibrium state and M falls back to equilibrium magnetisation $\boldsymbol{M_0}$, this process is called relaxation.

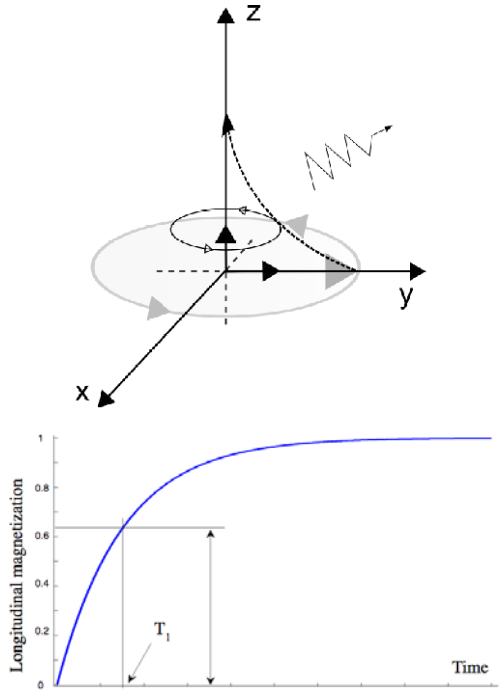

Figure 3.4: (Up)Spin-Lattice relaxation (T1 relaxation) and (Down) the magnitude of the longitudinal magnetisation is an exponential function of time t.

Image from http://zerpoii.opentronix.com/?p=1148

In the longitudinal plane, some high-energy protons flip back into their equilibrium state (low energy state), releasing the energy that was previously absorbed into the surrounding tissues. During this process, the longitudinal magnetization $\mathbf{M_z}$ regrows to equilibrium magnetisation $\mathbf{M_0}$. This behaviour is referred to as the T_1 relaxation or spin-lattice relaxation. The time constant, T1, is used to describe how fast spins transfer energy to the lattice or $\mathbf{M_z}$ returns to its equilibrium value. The relaxation time T_1 depends on the gyromagnetic ratio of the nucleus and the mobility of the lattice. In the absence of any other effects, the recovery of the magnetisation in the z-direction is described by the Bloch equation in the rotating frame of reference:

$$\frac{dM_z(t)}{dt} = \frac{M_0 - M_z(t)}{T_1}$$

And its solution is

$$M_z(t) = M_0\left(1 - e^{-t/T_1}\right)$$

where M_0 is the equilibrium magnetisation, the relaxation time T_1 is a time constant for a given lattice. Different tissues have different T_1values (**Table 3.2**).

In the transverse plane (x-y), spins' magnetic fields interact with each other and will cause spins to precess at different frequencies and thus spread apart (out of phase); this means that the transverse magnetization $\boldsymbol{M_{xy}}$ will reduce to zero. This process is called the T_2 relaxation or spin-spin relaxation. T_2 relaxation has to do with the interactions of the protons or spins and no net energy transfer occurs with T_2 relaxation. The rate of return to equilibrium of the transverse magnetization M_{xy} is characterised by a time constant, the spin-spin relaxation time, or T_2 relaxation time. This is described by the Bloch equation for transverse magnetization in the rotating frame of reference

$$\frac{dM_{xy}(t)}{dt} = -\frac{M_{xy}(t)}{T_2}$$

And its solution is

$$M_{xy}(t) = M_{xy}(0) * e^{-t/T_2}$$

where $M_{xy}(0)$ is the transverse magnetisation in the rotating frame at time t = 0 after removing the 90-degree RF pulse, and T_2 is a time constant for a given tissue. Different tissues have different T_2 relaxation times (**Table 3.2**).

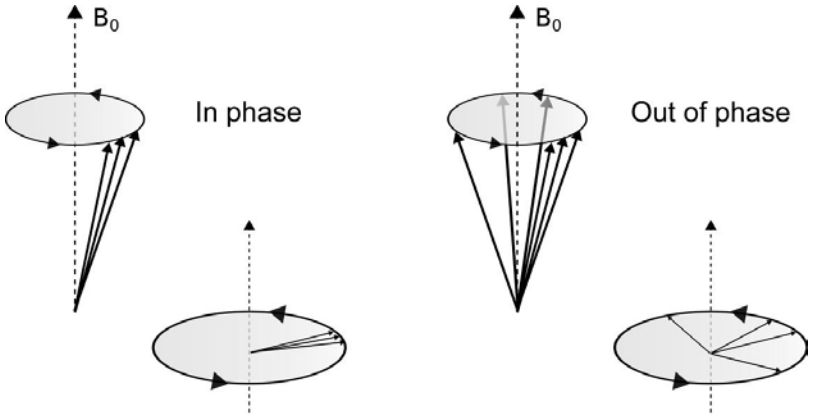

Figure 3.5: Illustration of In-phase and dephasing of the nuclei. Each nucleus precesses at a different frequency causing loss of coherence between the spins.

Image from http://zerpoii.opentronix.com/?p=1148

In the previous introduction, the spin-lattice relaxation and spin-spin relaxation processes, were described individually for clarity. In fact, both processes take place simultaneously and T_2 is always smaller than or equal to T_1. **Table 3.2** shows the T1 and T_2 values of several tissues frequently used.

Table 3.2: Approximate values of relaxation parameters T1 and T2 at 1.5T and 37 degrees (human body temperature) [95].

	T1 (ms)	**T2 (ms)**
Brain Gray matter	900	100
Brain white matter	600	80
Liver	500	40
Fat	250	60
Water	4000	2000
Skeletal muscle	900	50

In reality, the B_0 magnetic field is not absolutely homogeneous. The inhomogeneity in B_0 causes the spins to dephase faster and the transverse relaxation characterised by the effective transverse relaxation time, T_2*. The T_2* decay is considered as the combination of the imperfect B_0 field and T_2 dephasing and that, T_2* is always smaller than T_2.

The relaxation process in the transverse plane immediately following a 90-degree RF pulse is called free induction decay (FID).

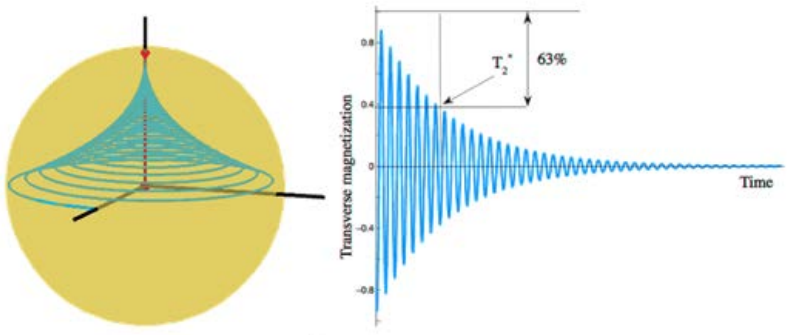

Figure 3.6: Illustration of an example of free induction decay.

3.1.6 Echo formation

Spin-echo (SE) and gradient-echo (GE) are the two types of methods to form echoes in MRI.

A spin-echo is formed by applying a 90° excitation pulse and a 180° refocussing pulse. Immediately after the 90° excitation pulse tips the longitudinal magnetization into the transverse plane, the spins start to dephase, making the net signal decay. After a time τ, the 180° refocusing pulse is applied (assume in x-axis), flipping the spins 180° about the x-axis. This means the relative phase of the spins in the transversal

plane is reversed, causing spins to regain coherence (Rephasing). The rephrasing of the spins will produce an echo at the time 2τ from the 90° excitation pulse. (Figure 3.7). The time between the 90° pulse and the centre of the echo, 2τ, is called echo time, TE.

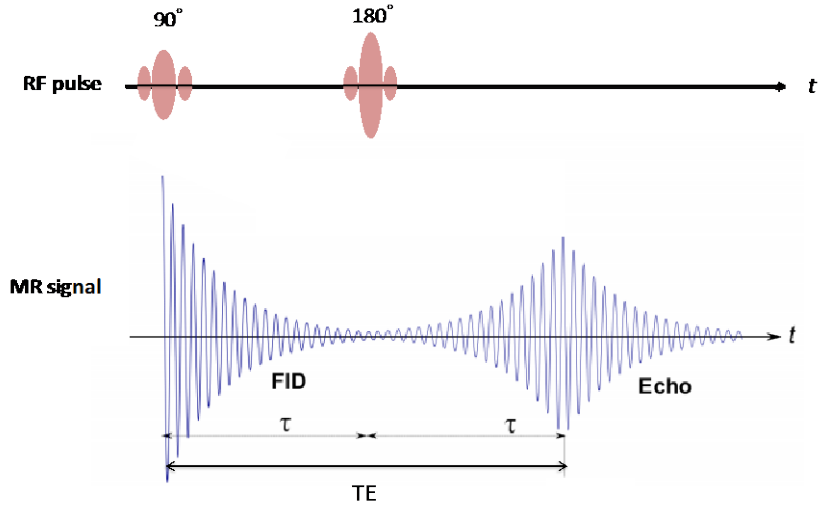

Figure 3.7: time graph of a simple spin echo sequence.

A gradient echo is formed with a linear magnetic field gradient (Gradient field is described in Subsection 3.2.1). After an excitation RF pulse of angle θ (less than 90°), a negative gradient lobe is applied immediately, and this causes spins to precess at different rates at different positions across the tissue, which leads to a faster dephasing than FID. The reversed positive gradient is then applied; spins start to rephrase and at time t = TE from the excitation pulse, all spins come in phase and an echo is formed (Figure 3.8).

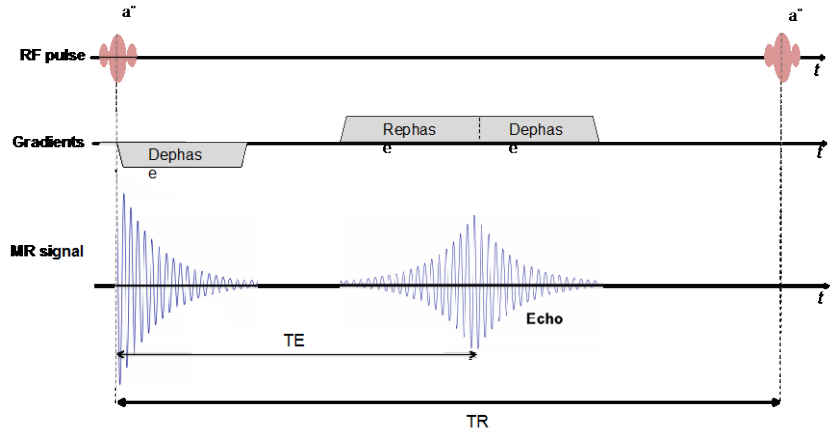

Figure 3.8: time graph of a simple gradient echo sequence.

3.2 Magnetic Resonance Imaging

To produce MRI images, the key components of the MRI hardware include a system magnet, a radio frequency (RF) coil, gradient coils and a computer (**Figure 3.9**). The main static magnet provides the main strong magnetic field referred as B0 field. A range of field strengths is used for clinical MR imaging from 1 to 3 Tesla. RF coils are used to transmit and receive the RF field. The electromagnetic field generated from the RF transmit coil, following an RF pulse is B_1. Gradients coils are used to slightly distort the magnetic field for slice location.

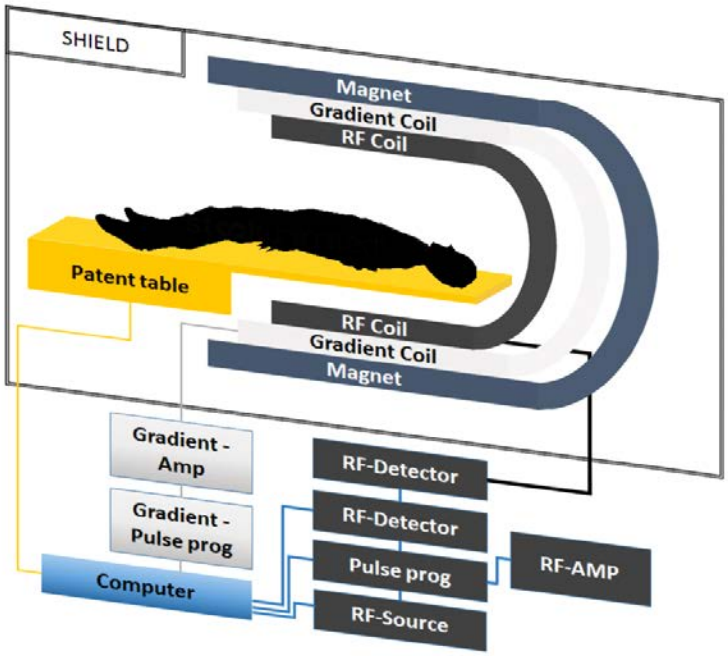

Figure 3.9: Illustration of the key features of the MRI machine.

In this thesis, the coordinate of the MRI scanner is defined as the **Figure 3.10**. Assume a patient lie supine with the head first in the MRI scanner,

- The head-foot (anterior-posterior) direction of the patient is referred as the z-axis which is along the central axis of the magnet tube. The direction of the B0-field is set along the z-axis.
- The left-right direction of the patient is referred as the x-axis which is in the horizontal plane.
- The front-back direction of the patient is referred as the y-axis which is in the vertical plane.

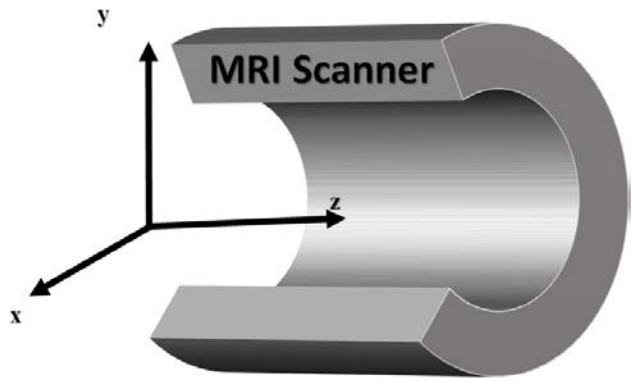

Figure 3.10: Illustration of the MRI coordinate planes with a patient lying supine with head first in the MRI scanner.

The anatomical planes will be used with relation to x-y-z axes,

- The axial plane is in the x-y plane with a fixed z. The RF pulses are usually in the x-y plane.
- The coronal plane is in the z-x plane with a fixed y.
- The sagittal plane is in the z-y plane with a fixed x.

3.2.1 Magnetic field gradients

As described in Section 2.1, the Larmor frequency is dependent on the strength of the external magnetic field B_0. In the homogeneous magnetic field B_0, all the protons precess at the same Larmor frequency and it is impossible to spatially distinguish between spins. To localise the spatial locations of the spins, three gradient magnetic fields, (Gx, Gy, Gz), *in x, y, z directions* respectively, are applied to the external magnetic field *B0*, thus each spin in the 3D space will precess at a unique Larmor frequency. The magnetic field gradients are generated by the corresponding gradient coils implemented in the MRI scanner (**Figure 3.11**).

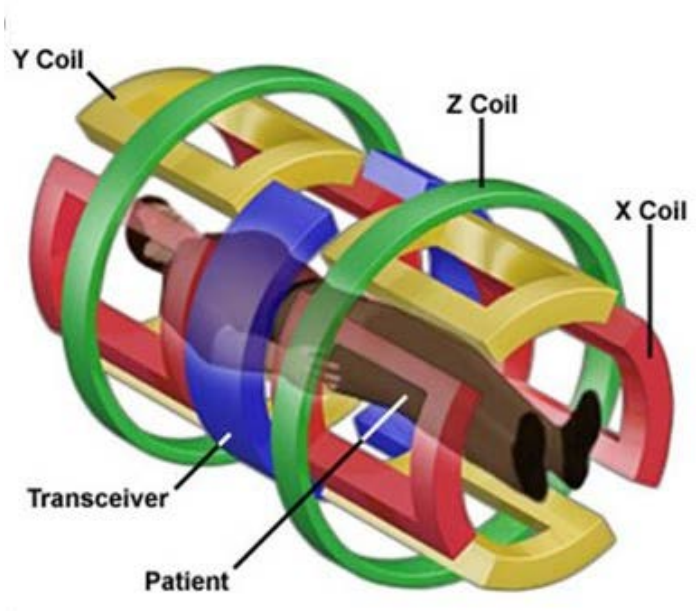

Figure 3.11: An illustration of the gradients coils in all three dimensions (Figure taken from Coyne, 2012).

Gz, the slice-selection gradient, will create a linearly variable magnetic field along the z axis (head-foot direction), and the Larmor frequency along the z-axis will be different depending on the positions. A desired slice of the object will be excited by using a RF pulse oscillating with the corresponding Larmor frequency range.

The Larmor frequency is dependent on the position along the z-axis:

$\omega = \gamma (B_0 + G_z(z-z_0)) = \gamma B_0 + \gamma G_z \Delta z$

Where γ is the gyromagnetic ratio for the proton. B_0 is the external magnet field, Gz is the gradient in the z-axis, z_0 is the isocentre of the magnet field B_0. ΔZ is the thickness of the desired slices. By changing Gz or the excitation RF pulse bandwidth, the thickness of the excited slice can be chosen.

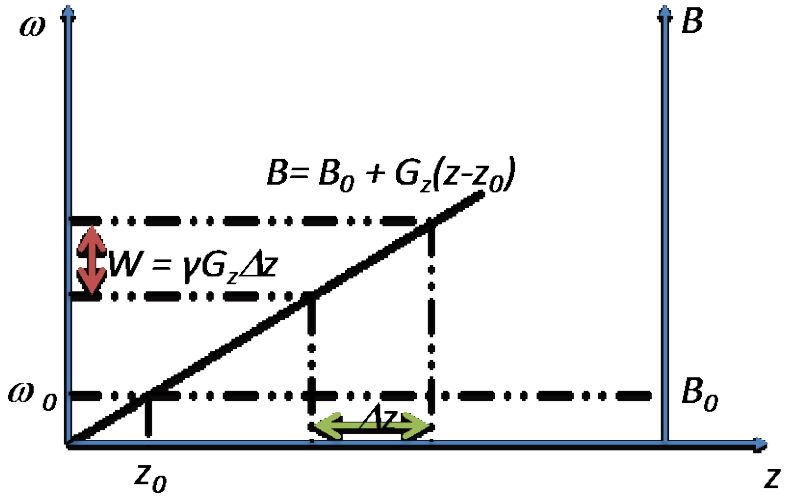

Figure 3.12:Illustration of the slice selection when applying an excitation RF pulse. z_0 is the isocentre of the magnet field B_0.

After the desired slice of the object is selected, all of the net magnetic moments in the slice precess at the same frequency and phase and cannot be distinguished spatially.

Linear field gradients along the y and x-axis, G_y and G_x, are applied to further localise the magnetic moments in the transverse plane.

When the phase encoding gradient, G_y, is turned on, it creates a gradient along the y axis, altering the proton precession frequency along the y axis. The spins at a lower magnetic field will slow down, while the ones at the higher magnetic field will speed up.

When G_y is quickly turned off, the frequencies of the spins in the selected 2D slice will return to their base value but the phases will be shifted between spins at different positions on the y axis. Based on the phase shift effect, positions of the spins with a particular phase in the y axis can be localised.

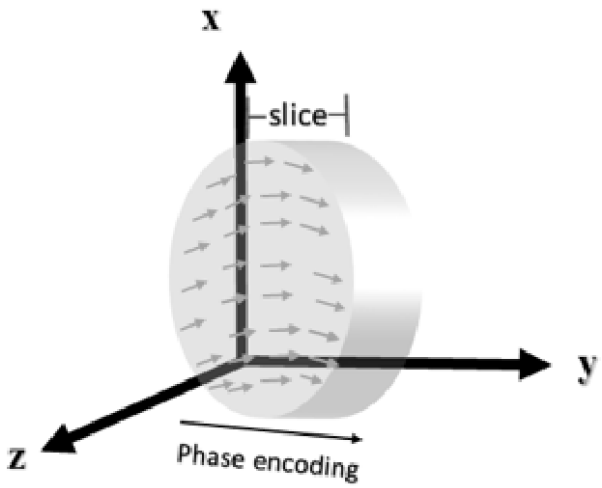

Figure 3.13: The effect of the phase-encoding gradient is to vary the phase of precession of the protons along the y axis. The phase of precession of protons along the x direction is the same at any location along the x axis.

When the frequency encoding gradient (Read out gradient), G_x, is applied along the x axis, the selected spins with the particular phase will precess at different frequencies along the x axis, resulting in the localisation of the spins in the 3D space.

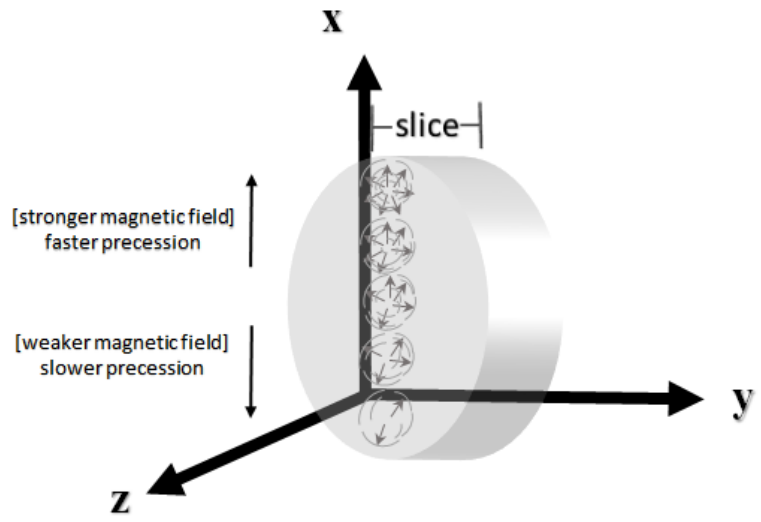

Figure 3.14:The effect of the frequency-encoding gradient is to vary the rate or frequency of precession of protons along the x axis.

3.2.2 K-space

After applying a 90-degree RF pulse and the three gradients, the signal emitted by the chosen spins during the FID will be detected by a receiver coil and it corresponds to the Fourier transform of the transverse magnetisation $\mathbf{M_{xy}}$. The spatial encoded signals in a single slice are stored in a k-space plane. The k-space contains the frequency and phase (k_{FE}, k_{PE}) information for every signal: each row, k_{PE}, is a phase-encoding gradient value, while each column, k_{FE}, corresponds to a frequency encoding gradient step. In k-space, the brightness stands for the signal intensity of

each point (k_{FE}, k_{PE}). The most popular trajectory pattern is sampling of the k-space signal along a Cartesian grid for its easy reconstruction of MRI image. The reconstruction for this type of acquisition is straightforward: by applying the inverse Fast Fourier Transform (FFT) of the k-space raw image, an MRI image of the selected slice can be reconstructed (**Figure 3.15**). Conventionally, the k-space sampling density is designated to meet the Nyquist condition, otherwise, the reconstructed image would suffer from aliasing artefacts (**Figure 3.15**) (Discussed in details in Subsection 3.3.6). Non-Cartesian trajectories are faster than Cartesian Trajectories, for example, radial lines and spiral sampling trajectories (**Figure 3.16**). Most of the image contrast information is found near the centre of normally ordered k-space (low frequencies). Detailed image information and noise are stored further away from the centre of k-space, corresponding to the high frequencies. In both radial and spiral trajectories, the sampling is much denser in low frequency regions in order to avoid low CNR and SNR. The other complicacy associated with these types of sampling is their need for a rather complicated reconstruction algorithms such as filtered back-projection, nonuniform FFT and model based reconstruction.

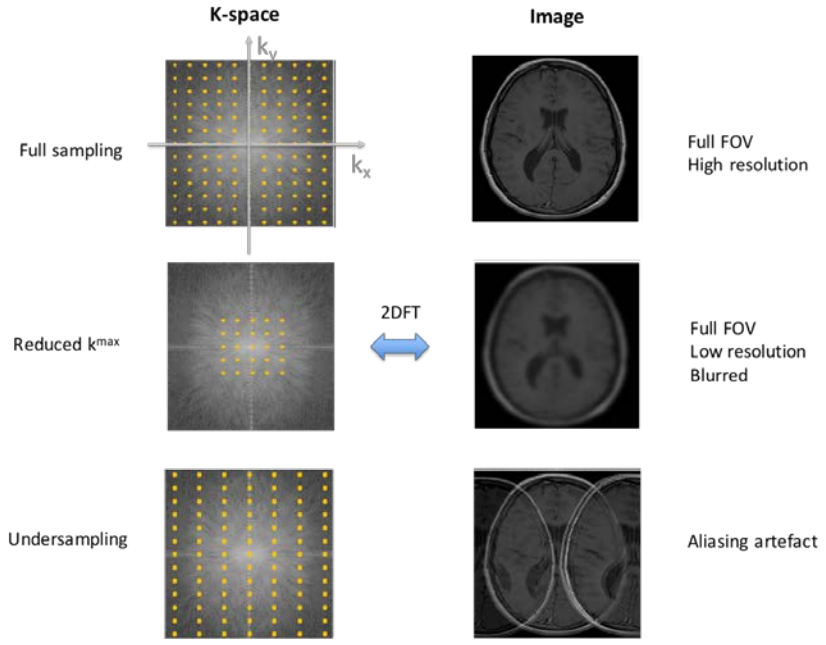

Figure 3.15: image quality is determined by the extent of k-space and the sampling density.

1st row shows when the k-space is fully covered and Nyquist condition is matched, expanse in sampling dense is accompanied with a higher spatial resolution. 2nd row shows only the inner area of k-space is covered, making the image with lower resolution. 3rd row shows the aliasing artefact in the MR image is caused by the undersampling in k-space.

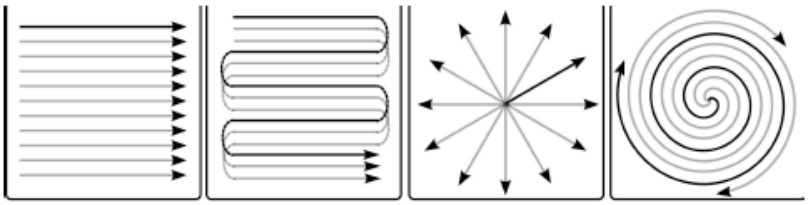

Figure 3.16: Common k-space sampling trajectory patterns. (from left to right) Cartesian 2D, Cartesian echo-planar, radial, spiral.

Image from Hans Chr van der Werf, Towards real-time imaging: a literature study on fast imaging by undersampling and smart reconstruction, 2012

3.2.3 Echo-Planar Imaging (EPI)

EPI is an image acquisition technique to increase the acquisition of each individual MR slice up to the speed of 50 ms. The term indicates a form of data acquisition in which multiple lines of k-space data are collected with only one spin excitation, providing significant reduction in overall scanning time. The technique is associated with multiple application of readout gradient alternating the polarity between positive and negative direction and hence the acquisition along k_x. To avoid the readout to rescan the same line, a small phase encoding gradient (pre-phasing grading) is applied to in timely manner to reinitialise the scanning in k_y direction, modulating by series of blips. Therefore, the entire k-space is scanned in a raster scan fashion, using only one excitation (**Figure 3.17**). Noteworthy is that the time varying gradient determines the trajectories during the readout.

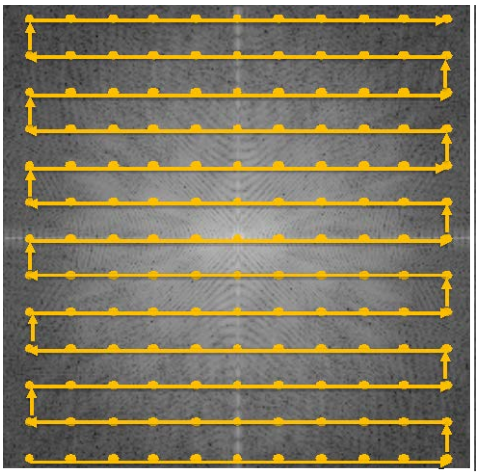

Figure 3.17: Illustration of the trajectory of EPI in k-space.

Theoretically, EPI performance is determined by the spacing between gradient modulation echoes and the time for k-space rectilinear trajectories. However, on the practical ground, magnetic field strength variation, eddy currents induced by the gradient fields and imprecision in time varying gradient fields would cause variation in the quality of trajectories. Therefore, in order to properly apply the EPI, a perfect agreement must be settled between the number of shots, number of sample for the given FoV (in the order of mm) [96] and the induced artefact/imperfections in the final image.

EPI acquisition in essence compromises the spatial resolution (i.e. blurring and distortion) and SNR related physical limitation. One of the earliest attempts to tackle the aforementioned challenge was the invention of multi-shot EPI strategy where the echo train is fractioned to multi several portions and consequently increase both SNR and spatial resolution [97] and comparable results to conventional T_2-weighted spin echo technique have been reported [98]. EPI found its application in in-vivo diffusion as well, where the difference between ADC has been demonstrated qualitatively for normal and disease tissues [99].

The fast acquisition time of single-shot EPI makes it minimise the motion artefact and is an ideal technique for diffusion-weighted MRI with fairly large number of diffusion directions and b-values. Regardless, the overall spatial resolution remained an unmet challenge owing to T_2^* blurring and the magnetic flux inhomogeneities e.g. at air-tissue interface. The former is generally due to the severe signal loss at k-space margin, hence the blurred image. The latter is associated with local field distortion which induces prompt susceptibility variations which in turn swamps the weak gradients, disturb the phase encoding and results in distortion.

There are undergoing research schemes to address the aforementioned challenges including parallel EPI, non-EPI trajectories and reduced field of view. Generally, the main effort is focused on choosing the optimum echo spacing and under sampling such that faster traversal along the phase encoding direction is guaranteed. These techniques are beyond the purpose of this chapter and interested readers are referred to the recent review [100].

3.3 Diffusion-weighted MR Imaging (DWI)

Diffusion-weighted magnetic resonance imaging (DWI) is a new functional MRI imaging technique that measures water diffusion. It is fast to acquire and there is no need to inject contrast agents. The mechanism of the DWI image contrast is based on differences in the rate of diffusion of water molecules in different environments. DWI provides a surrogate marker of tissue microstructure [20; 101; 102], and helps detect functional differences between malignant diseases and normal tissues. DWI is becoming more commonly used in oncological applications for tumour detection and characterization [101]. DWI has the ability to capture the diffusion rate of extracellular water molecules in the tissue, which Is hypothesised to probe the microstructure of the biological tissues.

3.3.1 Diffusion

Diffusion is caused by the microscopic movement of molecules in liquids and gases due to their thermal energy. At the microscopic scale, water molecules in unrestricted environments move freely and collide with each other in a random thermal motion, this phenomenon is known as Brownian motion, or free diffusion.

According to Fick’ s second law, the diffusion equation expresses how diffusion causes the concentration to change with time t:

$$\frac{\partial C}{\partial t} = D\nabla^2 C$$

where C is the concentration of the diffusing material at time t at one location, D is the diffusion coefficient for density C at the location.

Einstein proposed that in an isotropic material the net displacement σ of a particle caused by Brownian motion is characterized by a diffusion coefficient and can be expressed as:

$$\sigma^2 = 2Dt$$

where σ is the net diffusion displacement in any direction. D is the diffusion coefficient and is described by the Stokes-Einstein relation:

$$D = \frac{k_B T}{6\pi\mu r}$$

Where k_B is the Boltzmann constant, T is absolute temperature, μ is liquid viscosity and r is the particle radius.

3.3.2 Diffusion encoding

DWI sequences sensitize the MRI signal to the diffusion of water molecules as they diffuse through the extra-cellular space. The **P**ulsed **G**radient **S**pin **E**cho (**PGSE**) sequence is the most commonly applied diffusion weighted sequence (**Figure 3.18**) proposed by Stejskal and Tanner in 1965. It has a pair of large and equal gradient pulses before and after the 180° refocusing RF pulse, called diffusion-sensitizing gradients. The first pulse dephases the magnetization of spins and the second pulse rephases the spins. For stationary spins, which have no net movement during the diffusion gradients, there is no loss of signal. Due to the random nature of diffusion, diffusing spins move to a different location in the gradient field between pulses, causing phase dispersion, so signal attenuation occurs. A higher diffusion gives a stronger signal attenuation.

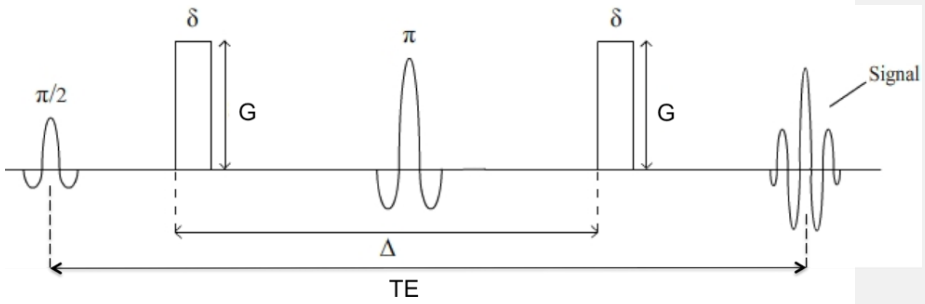

Figure 3.18: Basic PGSE sequence for diffusion weighting.

δ denotes the pulse width and Δ is the centre-to-centre spacing. G is the magnitude of the diffusion-weighting gradient.

3.3.3 b-values

The sensitivity of the DWI sequence to water diffusion can be expressed as the b-value, which can be changed arbitrarily as follows:

$$b = \gamma^2 G^2 \delta^2 \left(\Delta - \frac{\delta}{3}\right)$$

where G is the amplitude of the diffusion gradients, δ is the duration of the diffusion gradient, Δ is the time interval between the leading edge of the diffusion gradients, and γ is the proton gyromagnetic ratio [103; 104]. The unit of b is s/mm^2.

The b-value encodes a sensitivity to water diffusion. A large *b*-value gives a large signal loss in areas with high diffusion. This is called strong diffusion weighting. The greater b-value will result in increased contrast between areas of higher and lower diffusivity. When the applied b value is 0, which means no applied diffusion weighting, the PGSE sequence corresponds to the simple spin echo sequence.

3.3.4 Measuring the diffusion coefficient

The DWI signal from simple free diffusion where $<r^2> = 6Dt$ applies, is described by an exponential decay:

$$\frac{S(b)}{S(b=0)} = e^{-b*D}$$

Where $S(b=0)$ is the signal intensity without the diffusion weighting (that is when b = 0 s/mm^2) and is T_2-weighted.

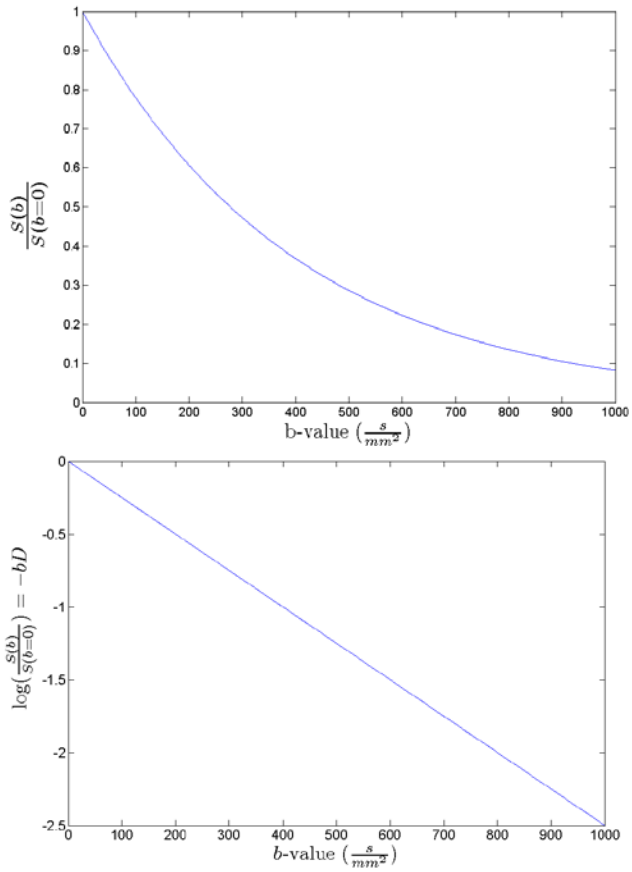

Figure 3.19: the ratio between image signal with diffusion weighting at b and without diffusion weighing is in an exponential curve dependant on b-value for isotropic diffusion, in practise isotropic diffusion is rarely observed.

By applying the logarithm transform of the signal, the slope of the curve stands for the physical diffusion coefficient D:

$$log(S(b)/S(b=0)) = -b*D$$

Water diffusion in tissue

Diffusion in biological tissues is not free as structural barriers, such as cell membranes and macromolecules, restrict the motion of water molecules in tissues. The measured restricted diffusion in biological tissues is an average over many restricted random motions instead of the physical diffusion coefficient, thus the term Apparent Diffusion Coefficient (ADC) is introduced. ADC represents the exponential signal decay of a single component of water molecules in one voxel. ADC may be calculated by using at least two b-values:

$$ADC = -\frac{1}{b_1 - b_0} \ln\left(\frac{S(b_1)}{S(b_0)}\right)$$

where $S(b_0)$ and $S(b_1)$ are the signal intensities when applying diffusion gradient b_0 and b_1 respectively.

Hindrance of water diffusion in tissues reveals the degree of tissue cellularity (number of cells per unit volume) and integrity of cell membranes and is observed in malignancies, hypercellular metastases, and fibrosis, where cell density is larger than in healthy tissues [20; 21; 23]. ADC is the quantitative measure of diffusion rate of water molecules in the extra-cellular space in the tissue: higher ADC values stand for less restricted diffusion while lower ADC values means more restricted diffusion in the tissue. Therefore, ADC may reflect tissue cellularity and can be used as a biomarker for tumour and necrosis.

When using ADC to quantify the diffusion degree in biology tissues, the DWI signal intensity is expressed as

$$S(b) = S(0) * e^{-b*ADC}$$

where S(0) is the signal intensity without the diffusion weighting (that is when b = 0 s/mm^2).

In practice, a strong diffusion weighting (high b-value) is commonly used in DWI imaging as it results in a large signal attenuation in areas with high diffusion rate, but it also causes decreased signal-to-noise ratio (SNR) and make the estimation of ADC less reliable. Therefore, repeated DWI acquisitions with multiple b-values are averaged at each b-value to increase image SNR.

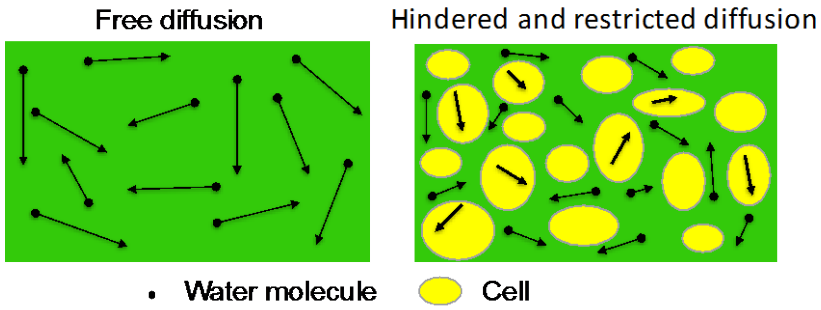

Figure 3.20: illustration of free diffusion and restricted diffusion in the tissue.

Green box represents a pixel in the tissue and the yellow ovals represent cells in the tissue.

3.3.5 Non-mono- exponential DWI models

In addition to mono-exponential DWI model, non-mono-exponential DWI models including bi-exponential intravoxel incoherent motion (IVIM), stretched exponential model, and kurtosis model, are briefly introduced as below:

3.3.5.1 Intravoxel incoherent motion *(IVIM)*

In 1988, Le Bihan et al. has proposed the bi-exponential model of diffusion, intravoxel incoherent motion MR imaging (IVIM). The IVIM model does not only describes the water diffusion within extra-vascular / extra-cellular space, but also take

into account of the microcapillary perfusion within the normal capillary network, thus it has the ability to separate capillary perfusion and tissue diffusion. The IVIM model is described by:

$$S(b) = S_0 \cdot (f\, e^{-b \cdot D^*} + (1 - f) e^{-b \cdot D})$$

where *S(b)* is the signal at a given b value, and S_0 is the signal with no diffusion weighing, *D** is the 'fast' diffusion (or pseudodiffusion) coefficient associated with perfusion, *D* is the 'slow' diffusion coefficient associated with diffusion, and *f* is the perfusion fraction ($0 \leq f \leq 1$).

- Fast and slow diffusing components

As stated in the previous equation, IVIM model has modelled the diffusion signal decay due to the contribution of the fast and slow diffusing compartments, which are related to perfusion and diffusion processes in the tissue respectively.

- *D* stands for 'slow' diffusion coefficient: the hindered water diffusion through static tissue is considered free from the influence of fast flowing water in the capillary network.
- *D** stands for the 'fast' diffusion coefficient, as water molecules in the blood flows in the randomly orientated capillary network, it is considered as 'pseudo- diffusion'.
- The effect of 'fast' diffusion goes down when the b-value increases (b >200 s/mm^2), however, at lower b values (0 – 200 s/mm^2) the influence can be significant.

- Number and choice of b values

The number and choice of b values are important for estimating parameters in the IVIM model; typically, at least four b values ranging between 0 and 1000 s/mm^2 and lower b values (0 – 200 s/mm^2) are needed to extract the perfusion sensitive information, however, there is no consensus on the number and magnitude of b values

that should be used in clinics. Koh et al. has suggested six to eight b values with several averages, among which are fewer high b value images and more lower b value data (e.g. four or more). Although IVIM is able to provide perfusion sensitive information, it should be recognised that IVIM is not always clinically feasible due to the increased scanning time.

3.3.5.2 Stretched-exponential model

Bennett et al. has proposed the stretched-exponential model to evaluate distributed diffusion and intravoxel heterogeneity.

$$S(b) = S_0 \cdot \exp\{(-b\ DDC)^{\alpha}\}$$

where DDC is the distributed diffusion coefficient, α is the stretching parameter and represents the heterogeneity index ($0 \leq \alpha \leq 1$). When the value of α is 1, which is in the case of high homogeneity in diffusion, the model simplifies to the mono-exponential model.

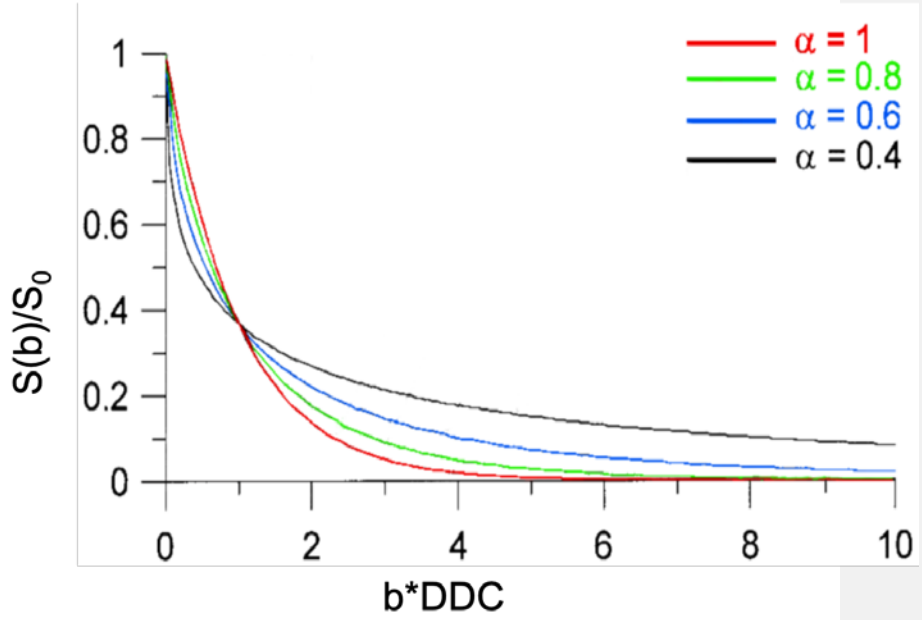

Figure 3.21: The decay in the stretched-exponential function $f = S(b)/S_0$ with different values of α (0.4, 0.6, 0.8, 1).

3.3.5.3 Kurtosis model

The relationship of diffusion signals and the b-value follows a mono-exponential decay in the case of completely free diffusion, however, due to restrictions of diffusion caused by cellular structures, water molecules do not always obey free diffusion in real cases. Thus, the kurtosis model is used to describe the non-Gaussian behaviour of diffusion which may reflect the complexity of tissue microstructure and provide important information about tissue microstructure. The model is described as follows:

$$S(b) = S_0 \cdot \exp(-b\, D_k + b^2 D_k^2 K/6)$$

where *S(b)* is the diffusion weighted signal along that direction with a given b value, and S_0 is the signal with no diffusion weighing, D_k is the apparent diffusion coefficient and K is the kurtosis along a certain diffusion direction,

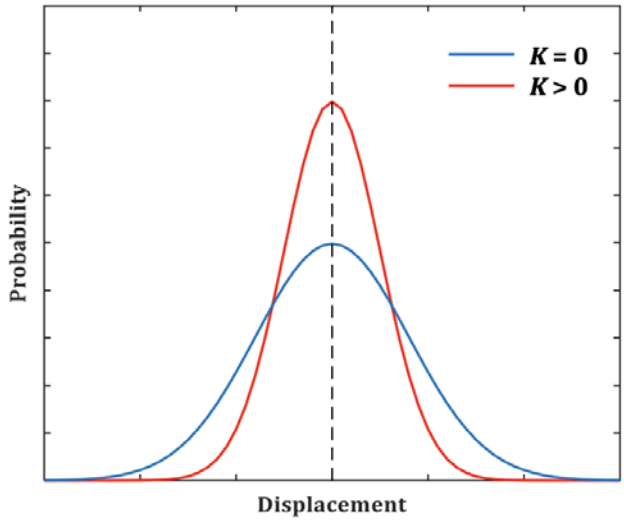

Figure 3.22: An example of a Gaussian distribution (blue line, K = 0) and a non-Gaussian distribution (red line, K>0)

3.3.6 Clinical application in oncology

DWI provides functional information about the tissue cellularity and the integrity of cell membranes and serves as a marker of tissue microstructure, which can be combined with the morphological information provided by conventional MRI [105]. It has the potential to quantitatively differentiate malignant diseases, stage tumours, and evaluate treatment effectiveness.

DWI appears to be an attractive tool to aid tumour detection/visualisation. DWI provides excellent contrast between tumour and suppressed background and is superior to CT in delineating tumours. Based on high image contrast between tissues,

the total tumour volume (TTV) can be derived from a semi-automatic segmentation tool.

As has been mentioned, the main advantage of DWI is delivering quantitative information, which means allowing the degree of water mobility in tissues is quantified by calculating ADC [2]. Following successful treatment for malignancy, the tumour cell density decreases as a consequence of necrosis and apoptosis, which results in increased water mobility and hence an increase in the tumour ADC values[22]. Furthermore, ADC measurements have been shown to have good measurement reproducibility and relatively low inter-scanner variability in the body [106], even in a multicentre study setting [107]. Hence, DW-MRI might be a very attractive tool for follow-up studies to indicate treatment effectiveness or failure [80].

3.3.6.1 DWI in the thoracic region

DWI is increasingly being used in the thoracic region due to developments in MR hardware, advances in MR techniques such as echo-planar imaging (EPI), parallel imaging and stronger MR gradients [21; 24; 103]. However, performing DWI in the lungs is still challenging because of motion artefacts related to respiratory and cardiac motion, and susceptibility artefacts from air-tissue interfaces [2; 23; 24]. **Figure 3.21** shows typical DW-MRI images and an ADC map, which can now be achieved in a patient with malignant pleural mesothelioma.

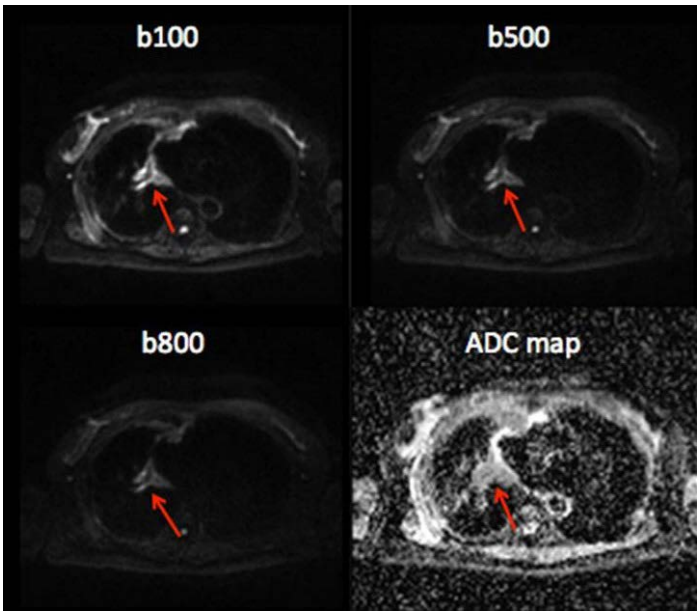

Figure 3.23: typical high quality DW-MRI images values and ADC map, which can now be achieved in a patient with malignant pleural mesothelioma.

3.3.7 Artefacts

EPI allows the acquisition of the whole k-space within one repetition time (TR) and greatly reduces the scan time (See **subsection 3.2.3**), so it is the most commonly used DWI acquisition scheme and is the main technique used in this project. However, the main disadvantage of EPI is the presence of artefacts.

Eddy current distortion

The rapidly changing magnetic fields produced by the magnetic gradients and RF fields induce eddy currents in the conducting components of the MR scanner. Eddy currents create inhomogeneity in the main magnetic B0 field, including time-varying gradients and shifts in B0 field. Eddy currents are mostly common in the fast imaging sequences when the gradients are turned on and off rapidly, such as EPI sequences.

Eddy currents cause spatial distortions including scaling, shearing and translation in the phase-encoding direction of EPI sequences.

Nyquist N/2 ghost

In the EPI scheme MRI signal is sampled using alternating gradients so EPI is very sensitive to ghost artefacts. Any imperfections in the acquisition can modulate the MRI signal at half of the Nyquist frequency. After Fourier transform, the phase errors induce N/2 ghosts which appear pixels shifted by N/2 in the phase-encoding direction (N: pixels number across field of view) (**Figure 3.21**). The main source of N/2 ghost is from B0 field inhomogeneity, especially from eddy currents.

Methods to reduce Nyquist N/2 ghosts include but are not limited to re-shimming, reducing echo train length, lowering the phase-encoding resolution, using multi-shot EPI, and applying parallel imaging acceleration.

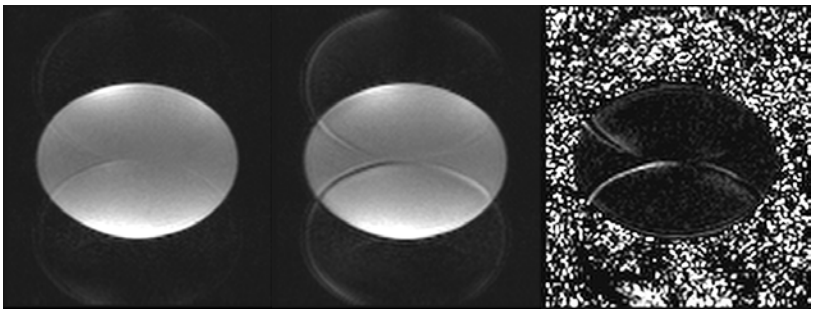

Figure 3.24: N/2 artefacts in DWI (b0), DWI (b900) and the fitted ADC map of a PDMS phantom. Note that N/2 artefact is made worse in DWI(b900) than DWI(b0) by eddy currents.

Susceptibility artefacts

The magnetic susceptibility characterises the property of material becoming magnetized when it is placed in an external magnetic field. Various tissues are associated with various magnetic susceptibilities, such as air has a very low magnetic susceptibility. Susceptibility artefacts are observed due to the susceptibility

differences between tissues (such as tissue air interfaces) as the differences cause local B0 field variations leading to signal intensity change in the interface areas and geometric distortions by spatial mismapping in the frequency encoding direction for spin echo and gradient echo imaging. In the EPI readout, the distortion appears in the phase direction due to the low bandwidth.

Chemical shift artefact

Chemical shift artefact produces high and low intensity bands near fat/water interfaces primarily in the frequency encoding direction.

Inversion recovery methods such as STIR (Short Tau Inversion Recovery) can be used for fat-suppression.

Motion artefacts

Motion effects, such as respiratory motion and heartbeat, have different impacts on diffusion MRI compared with other MRI sequences. MRI signal in DWI is purposely made sensitive to the diffusion-related molecular displacement in the extracellular space, so bulk or physiological motions during the time between the diffusion gradients will cause additional phase shifts and errors between read-outs.

3.3.8 The effect of diffusion on T2 measurement

As T2 will be measured in Chapter 4, here we briefly talk about the effect of diffusion on T2 measurement. Measurements of the transverse relaxation time T2, are usually measured with spin echoes, especially the Carr Purcell Meiboom Gill (CPMG) pulse sequence. Diffusion effects are a common source of error in measurements of T2, because the incoherent motion of spins in external magnetic field gradients distorts T2 weighting of the transverse magnetization, the measured T2-values are not accurate.

The diffusion of spins through these internal gradients affects the magnetization and as a result the measured T2 relaxation time decreases and be expressed as:

$$^1/_{T2} = {}^1/_{T2_{int}} + {}^1/_{T2_{diff}}$$

where $T2_{int}$ is the intrinsic T2 without diffusion effects and $T2_{diff}$ is the effect of diffusion.

The expected effect of the internal magnetic field gradients on the measured T2 with a CPMG sequence can be estimated from

$$^1/_{T2} = {}^1/_{T2_{int}} + {}^{\gamma^2 G^2 TE^2 D}/_{12}$$

where G is the magnetic field gradient experienced by the diffusing protons, with the diffusion coefficient D during the interecho time TE.

3.4 Chapter summary

This chapter introduces the reader to the principles of DWI. Throughout the chapter, the physical phenomena involved with MRI image acquisition has been described and the challenges and artefacts have been introduced providing the underground for exploiting DWI imaging sequences in the lung. Thus, the goal of this chapter was to provide a fundamental background with respect of the principle of DWI and sequence optimisation that might be needed for thoracic DWI imaging will be discussed in detail in the next chapters.

4 T2-adjusted computed diffusion-weighted imaging: A novel method to enhance tumour visualisation

4.1 Introduction

High-b-value (b > 1000mm^2/s) DWI images with corresponding ADC maps have shown great promises for the assessment of early treatment response due to their ability to non-invasively provide quantitative and qualitative information at the cellular level throughout the course of therapy [108; 109]. However, high-b-value images face the challenges of geometrical distortions and relatively low image signal-to-noise ratio (SNR). Computed diffusion-weighted magnetic-resonance imaging (cDWI) has been previously proposed to improve image SNR and reduce geometric distortions for high-b-value images [110]. By acquiring images at a range of lower b-values, cDWI has the ability to generate synthetic images corresponding to arbitrary b-values without increasing the image acquisition time [110]. cDWI was shown to improve the sensitivity and specificity of bone metastasis detection over conventional DWI, by enabling the radiologists to compute images of higher b-values [110]. In primary prostate cancer, cDWI at high b-values has been shown to perform better than or at least equivalent to directly acquired DW images with respect to image contrast-to-noise ratio (CNR) and deliver an improved tumour conspicuity [111-116]. Body DWI sequences usually use relatively long echo times (TEs), typically 60-100ms, and this imparts intrinsical T_2-weighting to all acquired DWI images. In turn, it results in heavy T_2-weighting in cDWI images. For this reason, cDWI is often (even at high b-values) unable to discriminate between cellular disease and tissues with long T_2-relaxation times (e.g. cystic areas, necrosis, fluid, and pleural effusion), leading to a diagnostic interpretation phenomenon known as ‘T2 shine through’.

In this chapter, a novel method namely, T_2-adjusted computed diffusion-weighted imaging (T_2-cDWI), has been proposed to generate synthetic DWI images corresponding to arbitrary b-values and echo times (TE). This has been achieved by acquiring a small subset of additional images with different (≥2) echo times. The additional images are acquired using the same DWI echo-planar-imaging (EPI) protocol so that the spatial resolution and imaging readout are matched. This implementation may provide a clinical tool to independently modify both the level of diffusion- and T_2-weighting for a given image. And it would also allow clinicians to

improve the image contrast by retrospectively removing/isolating the T_2-shine-through effect [117]. The purpose of this chapter is to describe the methodology behind this novel imaging strategy, derive mathematical approximations for the noise in T_2-cDWI and validate these models using a diffusion test-object. Furthermore, the feasibility of using T_2-cDWI in clinics will be investigated to improve image contrast and enhance disease interpretation in oncology.

This chapter is organised as follows:
Section 4.2 illustrates the theory of T2-cDWI model, the proposed optimal T2-cDWI sequence and its noise considerations. T2-cDWI will be applied on phantoms and clinical patients with methods and materials shown in Section 4.3, results in Section 4.4, and discussion in Section 4.5. The final section summarises this chapter.

4.2 Theory

When using a spin-echo echo-planar imaging (SE-EPI) sequence, the signal intensity for a given voxel location in the magnitude image is modelled by:

$$S = k \cdot H_\rho \cdot (1 - e^{-TR/T_1}) \cdot e^{-TE/T_2} \cdot e^{-b \cdot ADC} \quad \textbf{(4.1)}$$

where k is a scaling constant incorporating both coil sensitivity and receiver gain, H_ρ is the proton density, TR is the repetition time, T_1 is the tissue longitudinal relaxation time, TE is the acquisition echo time, T_2 is the tissue transverse relaxation time, ADC is the apparent diffusion coefficient and b represents the diffusion weighting.

4.2.1 cDWI model

cDWI is a mathematical computation technique that computes diffusion signal intensity at any b-value for the ADC values. Normally ADC values are estimated from DWI images acquired from at least two different b-values [110]. It follows that the ADC of tissues can be calculated on a voxel-by-voxel basis using:

$$S(b_c) = S^*(0) * e^{-b_c * ADC^*} \quad \textbf{(4.2)}$$

where $S^*(0)$ and ADC^* are per-voxel estimates of $S(0)$ and ADC, respectively. In this model, echo time is constant and T_2 contrast remains the same at various b-values for each pixel, so T_2 decay is disregarded.

4.2.2 T2-cDWI model

In single-shot fat-suppressed EPI DW sequences that allow for the acquisition of images at multiple combinations of b-values and echo times, assuming inversion-recovery is not used and TR is long enough to avoid T_1 effects, **Eq.4.1** can be modified as

$$S_i(b_i, TE_i) = S_0 \cdot exp\{-b_i \cdot ADC\} \cdot exp\{-TE_i \cdot R_2\} + \varepsilon_i \quad \textbf{(4.3)}$$

where S_0 is a constant and related to the proton density and measurement factors, b_i and TE_i are for the i^{th} combination of b and TE, ADC and $R_2 = 1/T_2$ are the tissue apparent diffusion coefficient and transverse relaxivity respectively. It is assumed $\varepsilon_i \sim N(0, \sigma_i)$ to be the additive noise.

T_2-cDWI is an approach where enough combinations of b and TE are acquired (at least 3) in the image acquisition protocol such that S_0, ADC and R_2 may be estimated for each pixel. In the estimation process, a linear least squares algorithm is used to fit to the logarithm of the acquired DWI data. With these estimated values, T2-cDWI signal contrast at any desired b-value (b_c) and TE (TE_c) are generated according to **Equation 4.4**.

$$S_c(b_c, TE_c) = \widehat{S_0} \cdot exp\{-b_c \cdot \widehat{ADC}\} \cdot exp\{-TE_c \cdot \widehat{R_2}\} \quad \textbf{(4.4)}$$

where $\widehat{S_0}$, $\widehat{ADC}$, $\widehat{R_2}$ are the corresponding estimated values for each voxel determined from the joint fitting.

Figure 4.1 shows the workflow of T2-cDWI approach.

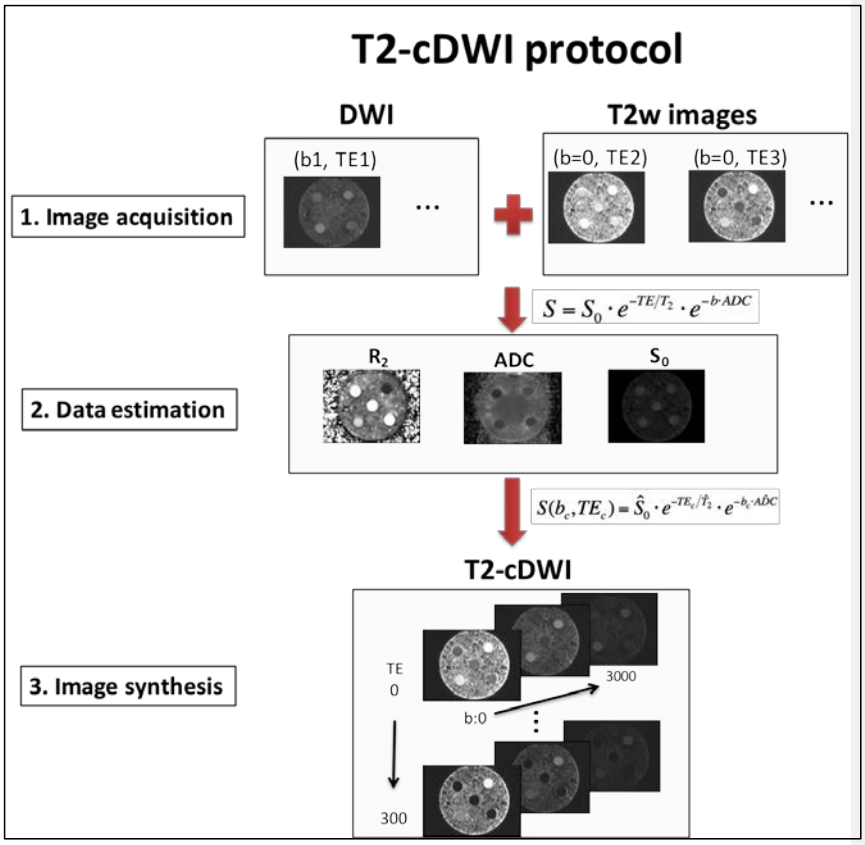

Figure 4.1: illustration of the workflow of T2-cDWI.

4.2.3 Optimised protocol for T2-cDWI

In general, the acquisition parameters (b-values, echo times and numbers of images) in the T2-cDWI protocol are in the choice of the readers. In order to achieve a better performance of T2-cDWI and easier calculation of noise characters in a relative short acquisition time, an optimised imaging protocol [118; 119] is suggested. These methods consider the calculations of *ADC* and R_2 as summarized below (also shown in **Table 4.1)**:

- Data acquisition A: 1 image acquired with ($b_1 = 0$, $TE_1 = TE_m$)[4];
- Data acquisition B: 3 images acquired with ($b_2 = 0$, $TE_2 = TE_m + \Delta TE_{opt}$);
- Data acquisition C: 3 images acquired with ($b_3 = b_{opt}$, TE_3)[5].

The b-values and echo times are optimised according to the diffusion and T2 properties (ADC, T2) of the expected tissue:

- $b_{opt} \approx 1.28/ADC$ (ignoring the effects of b-value dependence on minimum echo time and T2 [120])[6];
- $\Delta TE_{opt} \approx 1.28/R_2$ [118; 121];
- TE_3 should be the minimum echo time achievable on the scanner for the high b-value acquisition (for the institutional protocol and scanners a lookup table has been derived to provide the minimum TE over the range $0 \leq b \leq 6000$ s/mm^2, although approximations are available in [121].

[4] TE_m is the minimum possible echo time on the scanner for the minimum b-value $b_1 = 0$

[5] TE_3 is the minimum possible echo time for b-value $b_3 = b_{opt}$ on the scanner

[6] To achieve the optimal estimate of ADC, optimal b-value difference in two b-values DWI measurements [120, 121]:

$$\Delta b \cdot D = \xi$$

where D is the anticipated ADC for the tissue of interest. Δb is the difference in the two b-values.

ξ converges to 1.28 when ignoring the effect of b-values dependence on minimum echo time and T2 relaxation (More details see the reference ref 121 Saritas). And the first measurement is made with minimum weighting, b_1, that is b_1 is zero in this chapter, therefore, $b_{opt} \approx 1.28/ADC$

Table 4.1: b-values, echo times and number of images for the optimised protocol according to a tissue with known ADC and R2 properties. In total, 7 images have been acquired.

TE_m and TE_3 are the minimum echo times achievable on the MRI scanner for b = 0 and $b_3 = 1.28/ADC$ acquisition respectively.

Data Acquisition	b (s/mm²)	TE (ms)	No. of images
A.	$b_1 = 0$	$TE_1 = TE_m$	1
B.	$b_2 = 0$	$TE_2 = TE_m + 1.28/R_2$	3
C.	$b_3 = 1.28/ADC$	TE_3	3

4.2.4 Noise considerations for T_2-cDWI

Equation 4.3 can be considered as a special case of a family of exponential functions

$$\underline{S} = \exp\{\underline{\underline{X}} \cdot \underline{\alpha}\},$$

where $\underline{\underline{X}}$ is the $N \times 3$ matrix that contains the applied DWI parameters in the data acquisition, that is

$$\underline{\underline{X}} = \begin{pmatrix} b_1 & TE_1 & 1 \\ \vdots & \vdots & \vdots \\ b_N & TE_N & 1 \end{pmatrix},$$

and $\underline{\alpha}$ is the vector that contains the unknown parameters to be estimated, that is

$$\underline{\alpha} = \begin{pmatrix} ADC \\ R_2 \\ \ln S_0 \end{pmatrix}$$

such that the linearized least-squares estimate of the tissue parameters is given by:

Commented [MOU1]: Define X with two underlines.

$$\underline{\hat{\alpha}} = \left(\underline{\underline{X}}^{\mathrm{T}}\underline{\underline{X}}\right)^{-1}\underline{\underline{X}}^{\mathrm{T}}\, ln\,\underline{S}$$

In matrix notation **Equation 4.4** may be rewritten as

$$S_c = exp\left\{\underline{\underline{X}}_c \cdot \underline{\hat{\alpha}}\right\} = exp\{A \cdot ln\,\underline{S}\} = \prod_{i=1}^{N} S_i^{A_i} \qquad \textbf{(4.5)}$$

where $\mathrm{X}_c = (b_c, TE_c, 1)$ $\qquad \underline{A} = \underline{\underline{X}}_c \cdot \left(\underline{\underline{X}}^{\mathrm{T}}\underline{\underline{X}}\right)^{-1}\underline{\underline{X}}^{\mathrm{T}}$

Using error propagation, it is possible to approximate the expected variance of S_c:

$$\sigma_c^2 \approx S_c^2 \cdot \sum_{i=1}^{N}\left(\frac{A_i}{S_i}\right)^2 \sigma_i^2 \qquad \textbf{(4.6)}$$

4.2.4.1 Noise considerations for T2-cDWI for the optimised acquisition

For the specially optimised protocol in **Table 4.1**, it is derived that:

$$\underline{A} = \left(-\frac{b_c(TE_2 - TE_3)}{b_3(TE_2 - TE_1)} - \frac{(TE_c - TE_2)}{(TE_2 - TE_1)}, -\frac{b_c(TE_3 - TE_1)}{b_3(TE_2 - TE_1)} - \frac{(TE_1 - TE_c)}{(TE_2 - TE_1)}, \frac{b_c}{b_3}\right)$$

$$S_c = S_1^{A_1} \cdot S_2^{A_2} \cdot S_3^{A_3} \qquad \textbf{(4.7)}$$

$$\sigma_c^2 \approx \sigma^2 e^{-2b_c ADC} e^{-2TE_c R_2}\left\{\frac{A_1^2}{e^{-2TE_1R_2}} + \frac{A_2^2}{3e^{-2TE_2R_2}} + \frac{A_3^2}{3e^{-2TE_1R_2}e^{-2b_3ADC}}\right\} \qquad \textbf{(4.8)}$$

where σ^2 is the noise variance for the image acquired with one signal average.

Notably, for this optimised protocol multiples of 7 image acquisitions (see **Subsection 4.2.3** for the optimised T_2-cDWI protocol) are required to perform the T_2-cDWI calculation. It is therefore of interest to consider regions where $\sigma_c^2 < \sigma^2/7$, where improvements in noise reduction are gained using T_2-cDWI over conventionally acquired data.

Figure 4.2 demonstrates the theoretical advantages in noise reduction (Green surface areas) using this suggested T2-cDWI protocol (see Table 4.1) for a wide range of

desired b_c and TE_c. Additionally, T_2-cDWI enables the generation of contrast in regions where it would not be possible to directly acquire the data using the given gradient performance of the commercial scanner (Slew rate is 200 mT/m/ms) used for this study (i.e. blue surface areas where $TE_c < TE_{min}(b_c)$).

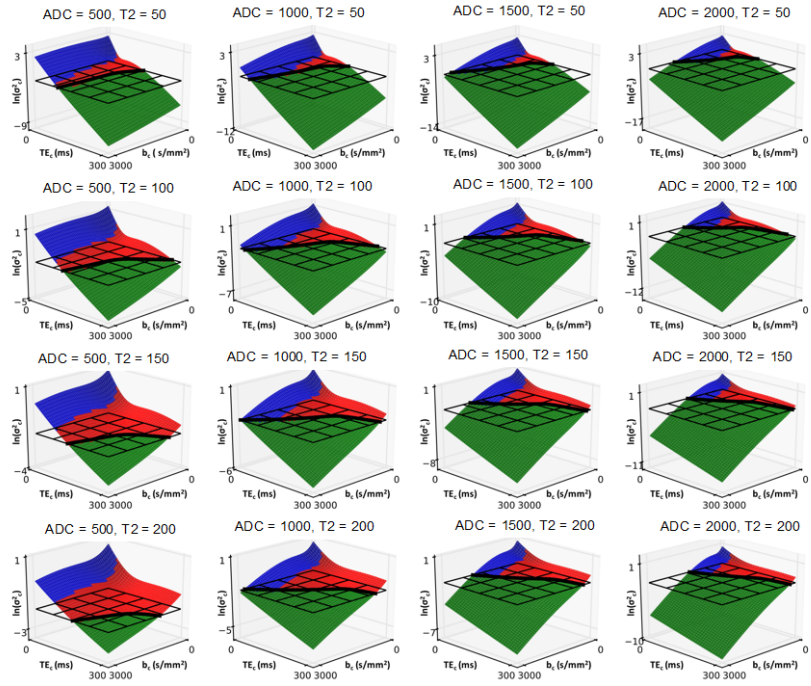

Figure 4.2: Comparison of the logarithm of noise-variance from an optimally acquired T₂-cDWI protocol, $\sigma^2(b_c, TE_c)$ (surface-plot) with logarithm of noise-variance from a conventionally acquired sequence, $\sigma^2 = 1$ (black wireframe).

Areas in which the surfaces are coloured in blue represent those combinations of b and TE that could not be acquired directly using the given gradient performance of the used scanner. Where $\sigma_c^2 < \sigma^2$, the surfaces are coloured in green. Where $\sigma_c^2 > \sigma^2$, the surfaces are coloured in red. Units of ADC are given in $\times 10^{-6}$ mm²/s, whilst for T₂ they are in ms. It is apparent there is often little advantage in directly acquiring images at a given b_c and TE_c combination (red surface areas) as T₂-cDWI either affords improved SNR (green areas) or allows generation of images that would not be possible to acquire directly (blue areas).

4.3 Methods and materials

4.3.1 Phantom studies

4.3.1.1 Validation of T2 map generated from EPI sequences

In order to verify the accuracy of estimating T2 from EPI scans, a cylindrical copper sulphate (CuSO4) MR phantom was scanned using the EPI sequence (Table 4.2) with b-value 0 s/mm^2 on a 1.5T MR system (MAGNETOM Avanto; Siemens Healthcare, Erlangen, Germany).

A reference multiple TE-SE sequence was employed on the same phantom at the same position. The FOVs in the two sequences were the same. Imaging parameters in these two sequences are presented in **Table 4.2**.

Table 4.2: Imaging parameters in the multiple spin echo sequence and DWI sequence.

Parameters	**Multiple TE spin echo sequence**	**DWI sequence**
Repetition time (ms)	3000	8000
Echo time (ms)	20/40/60/80/100/120/ 140/160/180/200/220/ 240/260/280/300/320	58/78/ 82/98/ 118/138
Field of view (mm)	261×380	261×380
Matrix size	128×88	128×88
b values (s/mm^2)	/	0
Number of signal averages	1	4
Receiver bandwidth (Hz/pixel)	230	1860
Echo-train length	1	1

The T2 map generated from the diffusion sequence was compared with the reference T2 map derived from the multiple TE-SE sequence.

4.3.1.2 Validation of the noise of T2-cDWI models

In order to validate the noise characteristics of T_2-cDWI (subsection 4.2.4) in the specifically optimised T2-cDWI protocol (subsection 4.2.3), a validation study was performed on a diffusion test-object [122]. This test-object consists of five sample tubes containing sucrose, manganese chloride ($MnCl_2$) and water, which encompass a range of T_2 (75 - 1408 ms) and physiologically relevant ADC values (700 - 1100 $\times 10^{-6}$ mm^2/s) (at 0°) [7] (**Figure 4.3**). In order to make the phantom contents was at 0°, the phantom was filled with ice - water one hour before the scanning, and more ice was added into the phantom to replace the melted amount 15min before the scanning.

[7] The values of T2 and ADC of the diffusion test-object were initial from the previous study in our team (more details could be found in the reference 122), and then were fitted again using our acquired images in this study. What is more, the ADC of ice water is about 1100 $\times 10^{-6}$ mm^2/s at 0°, and higher ADC cannot be achieved at this condition.

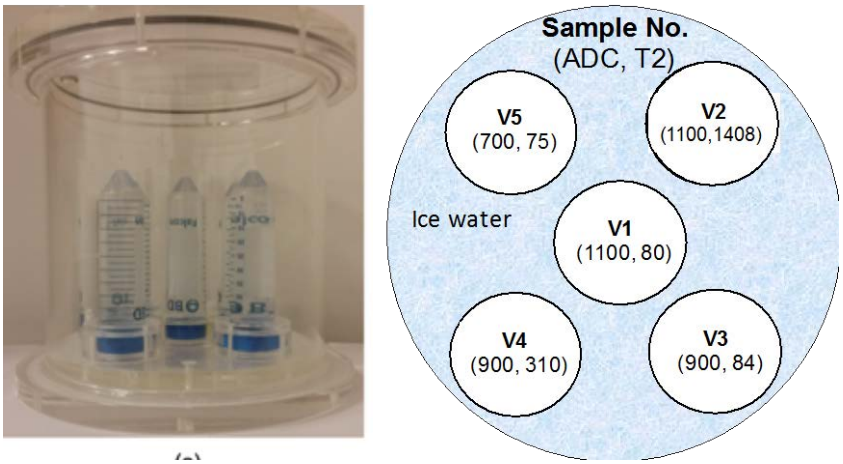

Figure 4.3: (Left) The test-object (the inner diameter is 18 cm and the height is 19 cm) containing five sample vials (diameter 2.7 cm) before filling ice water. The phantom was filled with a mixture of crushed ice and water and allowed to cool before use. (Right) An illustration of the diffusion test-object with 5 vial samples at 0°.

Each vial identifier is shown with its measured (ADC × 10^{-6} mm^2/s, T2 ms) values.

All vial samples are numbered with the same scheme used throughout this chapter.

Steps:

I. Axial images of the test-object (Figure 4.3) were acquired at the isocenter of a 1.5T system (MAGNETOM Avanto, Siemens Healthcare, Erlangen, Germany) using a prototype monopolar, SE-EPI sequence with an anterior six-channel receiver coil used in conjunction with the spine receiver coils. No parallel imaging was used. The sequence parameters are shown in **Table 4.3**.

Table 4.3： Image acquisition parameters of the optimised T2-cDWI protocol in the T2-cDWI noise verification study.

Parameter	Value
Repetition time (ms)	8000
Echo time (ms)	34.0/136.0/58.8
b - value (s/mm^2)	0/0/1100
Number of signal averages (NSA)	2/6/2
Slice thickness (mm)	5
Slice numbers	3
Pixel size (mm×mm)	2.7 × 2.7
Field of view (mm)	260×195
Acquired Matrix	96 × 72
Readout bandwidth (BW) (Hz/pixel)	1796
Echo-train length	1
partial Fourier factor	6/8
Diffusion scheme	Single spin echo
Diffusion-encoding scheme	3-Scan-Trace[8]

In this sequence b-values and echo times were optimised as ((b, TE) = (0, 34), (0, 136), (1100, 58.8) (s/mm^2, ms)) for the known diffusion and relaxation properties of vial 1 (ADC = 1.1×10^{-3}mm^2/s, T2 = 80 ms) according to the method described in **subsection 4.2.3**.

II. T_2-cDWI images were calculated using these data for each pairwise combination of b_c = 0, 750, 1500, 2250, 3000 s/mm^2 and TE_c = 0, 75, 150, 225, 300 ms, [9] ,using an in-house developed plugin [123] for OsiriX (Pixmeo, Geneva, Switzerland). This

[8] 3-Scan-Trace: acquisitions are performed using 3 orthogonal diffusion gradient directions sequentially.

[9] These b_c are synthetic values and not to compare with b-values from DWI image gradient, and they were used here to generate computed T2-cDWI images to show the advantages over acquired DWI images in changing image contrast.

plugin allows the user to compute images at any b_c (0-5000 s/mm^2) and TE_c (0 - 300 ms) in real-time.

III. Steps I and II were repeated such that T_2-cDWI difference images could be generated for each combination of b_c and TE_c.

IV. Regions-of-interest (ROIs), consisting of 75 pixels, were drawn within the vials on the images acquired at b = 0 s/mm^2 and TE = 34 ms (**Figure 4.4**).

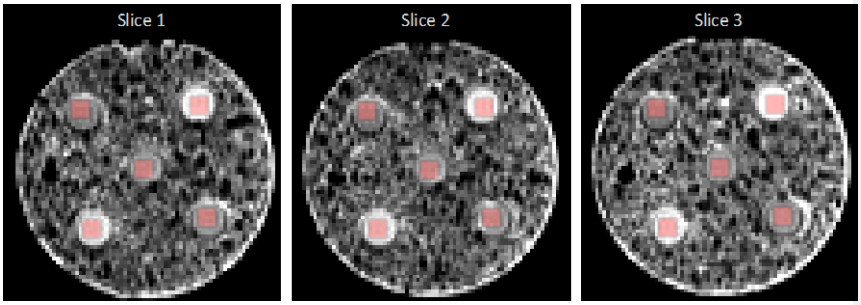

Figure 4.4: Acquired 3-slice DWI images (b 0 s/mm^2, TE 34 ms) of the diffuse test-object with ROIs overlain in red.

V. All the ROIs then translated onto the difference maps, on which the variance within these ROIs were calculated.

VI. The true noise variance in T_2-cDWI, σ^2, was estimated for each vial by dividing the variance of the difference values within the ROIs by 2 [124].

VII. The estimated noise variance from **Eq.4.7**, σ_c^2, was computed over the range of b_c (0 - 3000 s/mm^2) and TE_c (0 - 300 ms) and compared with the ground-truth values σ^2 at each combination of b_c and TE_c.

4.3.1.2.1 Simulation of Contrast-to-noise ratio

Using T2 and ADC values matched to the diffusion test-object (**Figure 4.3**), data were simulated for 10,000 voxels using Python 2.7 (Python Software Foundation), with Rician noise [125] added to S_0 (variance matched to that estimated from the acquired data), over the range of b-values (0 - 5000 s/mm^2) and TEs (0 - 300 ms). The standard deviation of all simulated voxels was calculated as an approximation of image noise, σ. The contrast-to-noise ratio (CNR) is a reliable metric in this context and here is computed between phantom samples over the range of b and TE,

$$CNR = \frac{Mean(SI_i - SI_j)}{\sigma}$$

where i, j are the sample numbers ($i, j = \{1,2,3,4,5\}, i \neq j$), SI_i and SI_j are the signal intensity distributions of Sample i and j in the diffusion test-object in the simulation, σ is the standard-deviation of ($SI_i - SI_j$).

4.3.2 Clinical Examples

Pleural effusion and solid plaques are the two main components of malignant pleural mesothelioma. Whilst solid plaques are more cellular, pleural effusion contains a higher fluid content and so it is hypothesized that they may be differentiated using different T2 and diffusion weightings by using T2-cDWI. To investigate T_2-cDWI in clinical settings, T_2-cDWI has been prospectively applied to clinically proven MPM patients. This proof-of-concept investigation was approved by the institutional research and ethics committee, and prior written consent was obtained from all patients.

4.3.2.1 Image acquisition

Malignant pleural mesothelioma patients (n = 4) were scanned on a 1.5T system (MAGNETOM Avanto, Siemens Healthcare, Erlangen, Germany). The optimised T2-cDWI protocol was not applied in the clinical cases and the reason is that the ADC

and T2 values of the MPM of our patients are not known before acquisition, thus a fat-suppressed EPI sequences were applied with optimal combinations of b-value and TE (b = 100 s/mm^2, TE = 82 ms), (500, 82), (800, 82), (0, 60), (0, 82), and (0, 177)[10]. Other sequence parameters are shown in **Table 4.4**.

In the study, no motion control was employed as most patients suffer from shortness of breath, and/ or, chest/breathing pain, so all the measurements were acquired during free breathing. To improve the signal-to-noise ratio of the images and also average over motion, all the measurements were acquired with four acquisitions.

[10] For these additional T_2-wighted sequences (when b-value is 0), three different echo times were chosen, including the same echo time (82 ms) used in the DWI sequence, the minimum (60 ms) and one maximum echo time (177 ms) in the available range on the scanner.

Table 4.4: The T2-cDWI imaging protocol used in the clinical study.

Parameter	Value
Sequence	Single-shot EPI
Coil	Body array coil
Breathing	Free breathing
Fat-suppression technique	SPAIR
Slice orientation	Axial
Phase-encode direction	Antero-posterior
Diffusion gradient scheme	Single spin echo
Diffusion-encoding scheme	Orthogonal
Parallel imaging	GRAPPA[11] = 2
Repetition time (ms)	8100
Number of signal averages (NSA)	4 (separated)
Slice thickness (mm)	5
Gap slice (mm)	0
Number of slices	30
Pixel size (mm × mm)	3 × 3
Field of view (mm × mm)	380 × 273
Acquired Matrix	128 × 92
Readout bandwidth (BW) (Hz/pixel)	1860
Echo-train length	1
partial Fourier factor	6/8

[11] GRAPPA: generalized autocalibrating partially parallel acquisition.

4.3.2.2 Data processing

Computed images were generated for clinical datasets utilising **Eq.4.4**. S_0, T2, and ADC are estimated from joint modelling of the diffusion- and T2-weighted images. Estimation of imaging parameters and synthetic images was achieved using the aforementioned in-house developed software (**Figure 4.5**).

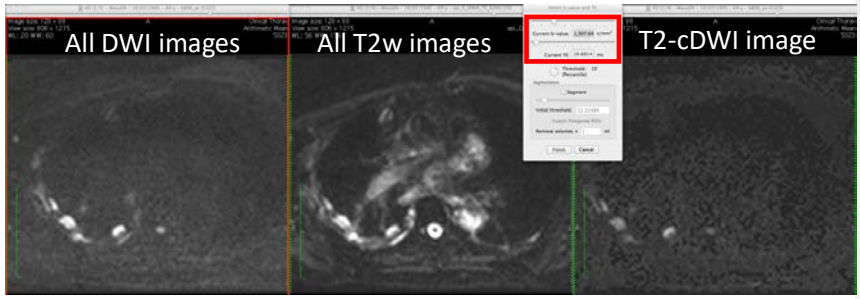

Figure 4.5: The interface of the plugin in Osirix to simulate T2-cDWI images with arbitrary b_c (0 - 5000 s/mm^2) and TE_c (0 - 300 ms) in real-time. The left is the DWI images with all three b-values shown in 4D while middle is the acquired T2w images with all three TEs shown in 4D. The right shows the generated T2-cDWI image at bc of 1307 s/mm^{2}and Tec of 10.7ms.

4.4 Results

4.4.1 Validation of T2 map generated from EPI sequences

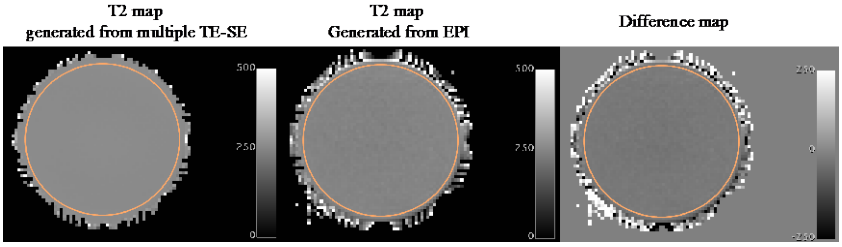

Figure 4.6: T2 maps derived from (left) multiple TE-SE and (middle) EPI sequence, and (right) their difference map.

T2 maps of the cylindrical copper sulphate MR phantom[12] derived from the reference sequence and the EPI sequence are shown in **Figure 4.6**. The mean value within the ROI on the T2 map derived from the diffusion-weighted sequence (middle) was 258 $\pm$ 4.8 (range: 215 - 285) ms, compared with 272 $\pm$ 1.3 (range: 269 - 276) ms from the reference TSE sequence (Left). The accuracy of estimating T_2 from diffusion-weighted sequences is 95%.

4.4.2 Validation of the noise of T2-cDWI models

Figure 4.7 presents the synthesised T2-cDWI images of the test-object at a range of echo times and b-values. T2-cDWI has the ability to generate synthesised DWI images at any b-value and TE, including those that cannot be acquired directly on the MRI scanner using conventional diffusion-weighted EPI sequences (black dashed boxes). It can be observed that by synthesising short echo times and high b-values, it is possible to suppress the signal from components with long T_2 (vial 2, top right image), while increasing the signal from components with low ADC but shorter T_2 (vial 5, top-right image, see white arrow). Conversely, by extending the TE_c to long values (e.g. 300 ms) it is possible to increase the signal of regions with long

[12] This cylindrical phantom is different from the diffusion test-object described in Figure 4.3, and it does not consist of any sample tubes.

T_2 (vial 2, bottom-left image, see black arrow) compared to other regions without requiring a significant increase in image acquisition time.

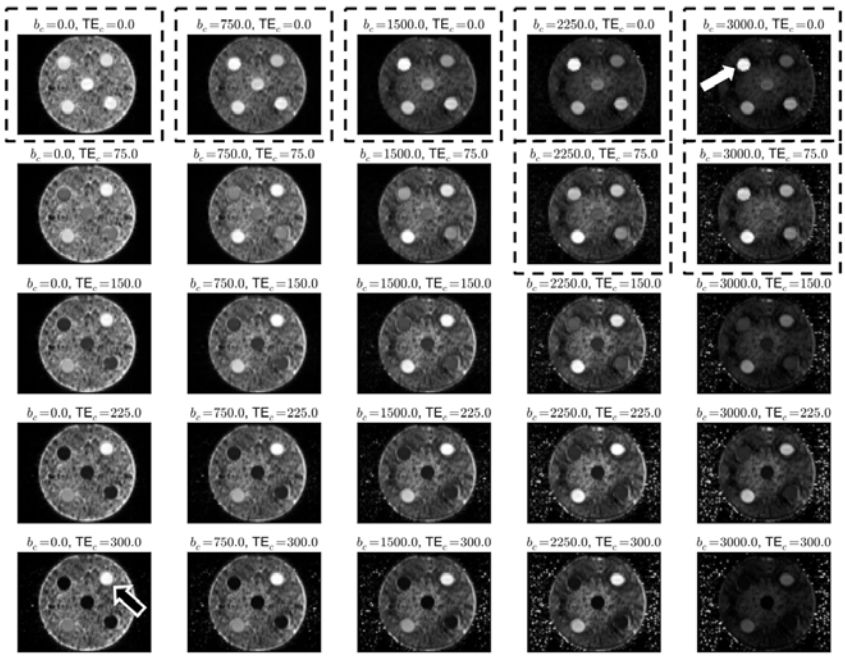

Figure 4.7: T2-cDWI images of the diffusion test-object at varying computed b-values, b_c and echo times, TE_c.

The windowing on all images has been set to optimise the visual contrast between vials. It is shown that by extrapolating the echo time to TE_c = 0.0 ms and the b-value to b_c = 3000 s/mm^2 it is possible to enhance the signal in the vial with low ADC and long T_2 (V5, white arrow). Conversely, by synthesising images with long TE_c, T2-cDWI images are acquired where the contrast favours components with a long T_2 (V2, black arrow). Those combinations of b_c and TE_c surrounded by black dashed boxes cannot be acquired directly on the MRI scanner using conventional diffusion-weighted sequences.

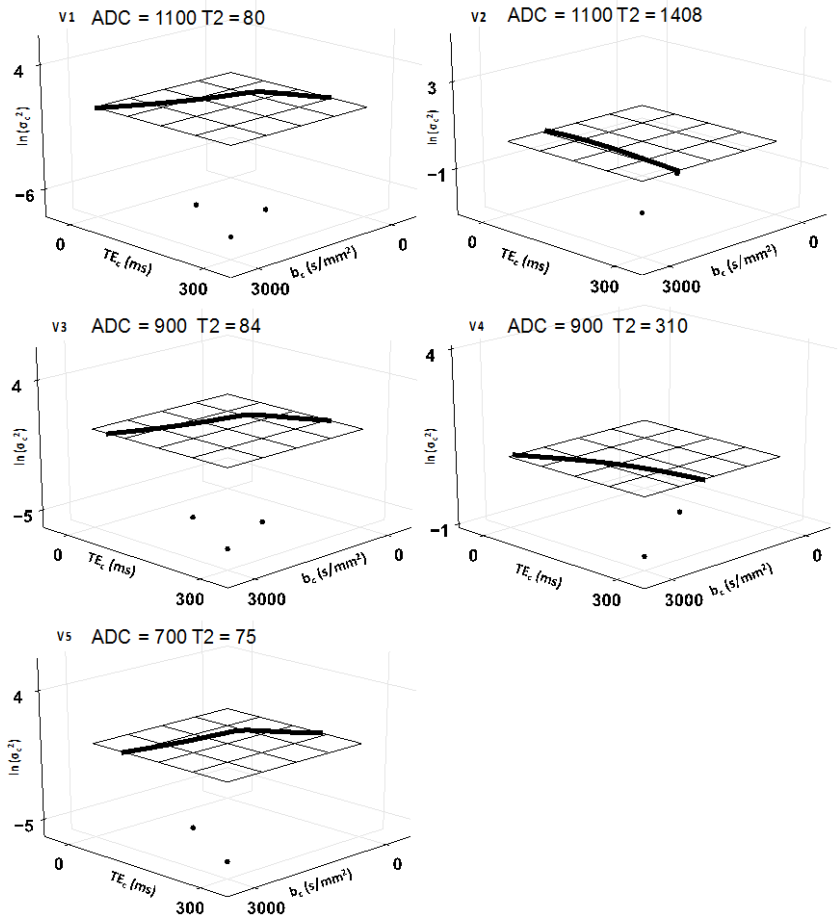

Figure 4.8: Measured image noise variance for each of the vial in T_2-cDWI, and the estimated noise variance according to Equation 8, over the range of b_c and TE_c values for each vial in this phantom. Units: ADC: × 10^{-6} mm^2/s, T2: ms

Black circles in the surface plots represent measured noise variance, σ^2, for each of the vials in the computed images with a range of b-values and echo times. The analytical estimation of the noise variance from the vial ADC and T_2 values is depicted as a surface plot (Green areas: $\sigma_c^2 < \sigma^2$, red areas: $\sigma_c^2 > \sigma^2$, blue areas: combinations of b and TE that could not be acquired directly using the given gradient performance of the scanner). There is a clear correspondence between

the estimated and measured values for σ_c^2. Black wireframes indicate the expected noise variance for an acquisition scheme of equivalent acquisition time to T_2-cDWI, but with four image averages at each respective b_c/TE_c. The solid black line represents the intersection between the surface curves and the black wireframes. It is observed that T_2-cDWI provides SNR advantages over conventional acquisitions for certain combinations of b_c/TE_c in this phantom.

In **Figure 4.8,** the true image noise in T2-cDWI (black circles) is well approximated by Equation 8 (surface plot) over the range of T2, ADC, b_c, and TE_c values explored in this phantom. Also, for vial V1, V3 and V5, it is shown that the noise variance in T2-cDWI is lower than that expected by direct calculation over the same image acquisition time (black wireframe) for many larger *b*/*TE* values. It is noteworthy that the b-values and TEs of the acquisition sequence were optimised for vial V3, and V1 and V5 both have similarly short T2 relaxation times. Surface plots below the black frame shows an improvement of the computed T2-cDWI images due to lower noise, which indicates that improved SNR can be achieved using synthetic DWI compared with conventional methods at high b/TE values.

4.4.2.1.1 Result of Simulation of Contrast-to-noise ratio

Figure 4.9 shows the simulated CNR between vial V3 and V2 when using the specially optimised T2-cDWI protocol (parameters are shown in **Table 4.3**) for the properties of vial V3. It is clear that the CNR between vial V2 and V3 was optimised by applying a moderately high TE_c (~125 ms) and low b_c (0 s/mm^2).

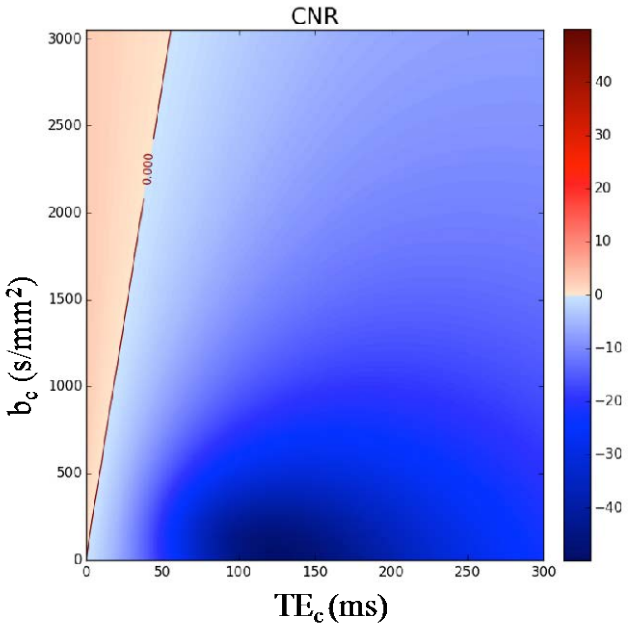

Figure 4.9: The simulated CNR between vial V3 and V2 at each TEc and bc (Red: V3 has larger signal intensity than V2; Blue: V3 has smaller signal intensity than V2).

V2 and V3 have very similar ADC values (1100 and 900 * 10^{-6} mm^2/s respectively) but quite different T2 values (1408 and 84ms respectively), indicating that the CNR will be more sensitive to echo time variations than b-values.

4.4.3 Clinical results

Simulated T2-cDWI image noise for MPM solid tumour and pleural effusion

Figure 4.10 demonstrates the theoretical advantages in noise that can be achieved using the T_2-cDWI separately for the solid tumour and pleural effusions at a wide range of desired b_c (0 ~ 3000 s/mm^2) and TE_c (0~300ms) following the protocol employed in this study.

For both components, it is apparent there is often less SNR advantage in directly acquired images over T2-cDWI (e.g. red surface areas). The reason is for most combinations of b_c and TE_c, T_2-cDWI either affords improved SNR (green areas) or allows generation of images that would not be possible to acquire directly (blue areas).

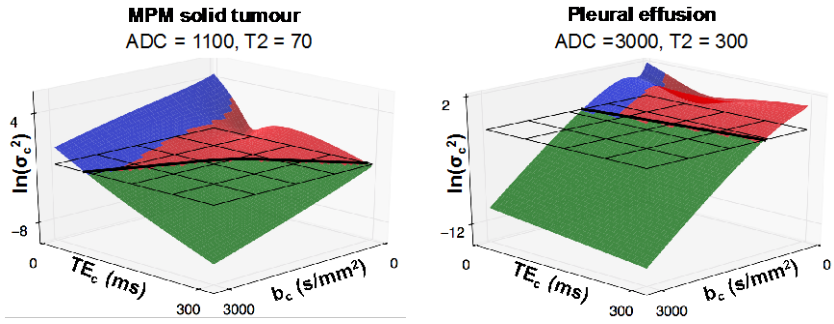

Figure 4.10: Comparison of the logarithm of noise variance of MPM solid tumour and pleural effusions (assume the same property as pure water) from the T_2-cDWI acquired from the clinical study, $\sigma_c^2(b_c, TE_c)$ (surface-plot) with logarithm of noise-variance from a conventionally acquired sequence, $\sigma^2 = 1$ (black wireframe). (ADC unit: 10^{-6} mm^2/s, T_2 unit: ms).

Green areas: $\sigma_c^2 < \sigma^2$; Red areas: $\sigma_c^2 > \sigma^2$; Blue areas: Not accessible on the scanner.

T2-cDWI in mesothelioma

Figure 4.11 shows a series of T2-cDWI images of a 73-year old male mesothelioma patient acquired using various computed b-values (s/mm^2) and TE (ms). The first row shows simulated images with a fixed small b-value (10 s/mm^2) and increasing TE values. As TE increases, the background tissues are suppressed, and the signal contrast between pleural effusion (Fluid) (blue arrow) and the other tissues increases dramatically. On the second row, a short computed echo time was used (10 ms) and images at various b-values were simulated. Solid tumours (red arrows) remain hyperintense compared to the fluid component as the b-value is increased.

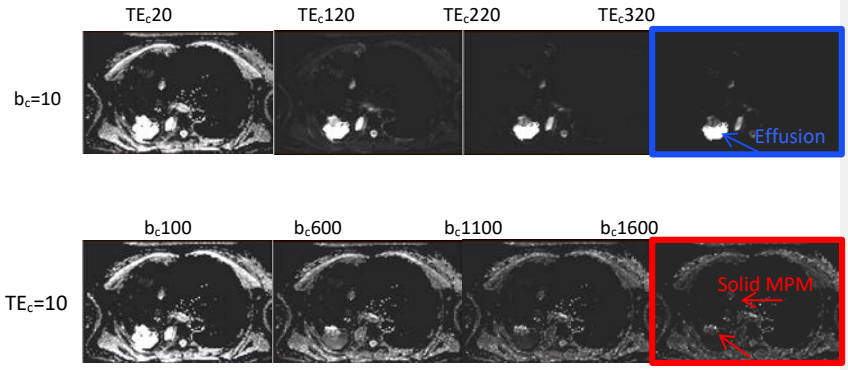

Figure 4.11: A series of T2-cDWI images of a 73-year-old male mesothelioma patient using various b-values (s/mm^2) and TE (ms).

The upper row shows simulated images with a small b_c (10 s/mm^2) and various TE_c while the lower row simulates images with a short TE_c (10ms) and four different b_c-values.

T2-cDWI vs cDWI images

In **Figure 4.12**, a short TE (5ms) was simulated for the T2-cDWI images on the first row. A solid tumour (red arrow) and the pleural effusion (blue arrow) are both bright on the T2-weighted image and low b-value cDWI images. As the b-value increases, there is a notable decrease of the signal of the fluid (blue arrow), and an obvious improvement in the image contrast between solid tumour and fluid, thus it has the potential to segment solid and fluid component of mesothelioma.

cDWI images were simulated by using a clinical TE value (TE = 82ms, the second row). By comparing images in each column, cDWI images show lower signal intensities and contrast between tumour and fluid than T2-cDWI images with a short echo time (TE = 5ms).

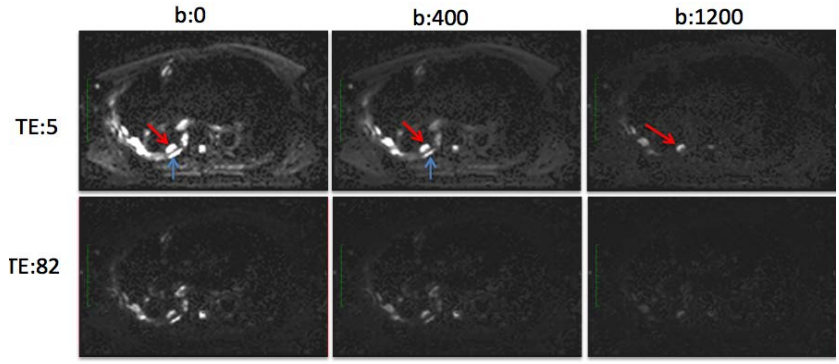

Figure 4.12: T2-cDWI images of a 69-year-old male MPM patient at various b_c values (s/mm^2) and TE_c (ms).

The upper row shows simulated images with a short TE_c (5 ms) and various b_c values. As the b-value increases, there is a clear decrease of the SNR of the fluid (blue arrow), and an obvious improvement in the image contrast between solid tumour and fluid. The lower row simulates images with an intermediate TE_c (82 ms) and three different computed b-values. As the echo time in the acquisition sequence is 82ms, the lower row images can be considered as the cDWI images with different computed b-values as well.

T2-cDWI vs DWI, cDWI

Two compartments within the MPM disease are presented in **Figure 4.13 e-f**: (i) solid tumour, characterised by low ADC and short T_2 and (ii) pleural effusion, with high ADC but long T_2. Fluid components were hyperintense on the acquired high b-value image (**Figure 4.13a**) due to the T_2 shine-through effects caused by the long T_2 of pleural effusions. Although contrast improvements could be achieved by computing a higher b-value through conventional cDWI (**Figure 4.13b**), the suppression of T_2 shine-through was inadequate to discriminate between compartments. However, after decreasing TE_c to zero through the use of T_2-cDWI (**Figure 4.13c**), it was possible to reduce the hyperintense signal of pleural effusions, and improve the contrast of the solid tumour. Conversely, by using a high TE_c and low b_c (**Figure 4.13d**) it was

possible to identify only those compartments associated with long T_2 and thus visualise the extent of pleural effusion.

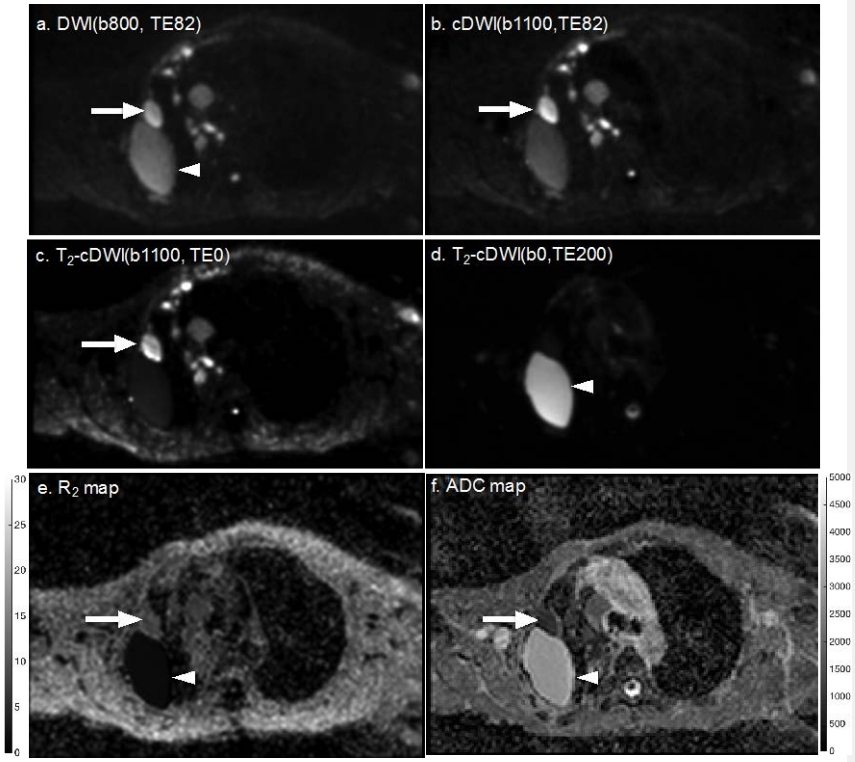

Figure 4.13: Axial images of a 62-year-old male with mesothelioma in the right lung for (a) acquired DWI (b800, TE82), (b) computed DWI (b 1100, TE82), (c) T_2-cDWI (b1100, TE0), and (d) T_2-cDWI (b, TE 200), (e) estimated R_2 map and (f) ADC map. b-value unit: 0 s/mm^2, TE unit: ms.

The solid tumour (arrow) and pleural effusion (arrowhead) both show hyperintense signal on the acquired high-b-value DW image due to the T_2 shine-through. Pleural effusions are still misinterpreted with solid disease even using a higher b-value in cDWI. By bringing the TE down to zero ms on T_2-cDWI, pleural effusions are suppressed very well and the solid tumour can be easily

segmented out. In contrast, using a very high TE and small b-value, the solid tumour and background tissue are suppressed.

T2-cDWI vs. exponential image

Using T_2-cDWI (**Figure 4.14**, **b** and **d**), the distinction of solid versus fluid disease has been improved, hence aiding disease identification. Pleural effusions demonstrated very high SNR in image (a) as well as (b) in **Figure 14**, but increasing TE and decreasing b-value further suppressed the solid disease (**Figure 14b**). This can be appreciated quantitatively; the pleural effusion returns similar mean signal intensity (~310) in both (a) and (b), while the mean signal intensity of solid tumour decreased from 85.6 to 25.5, thus enhancing visualisation of the fluid disease in (b). By contrast, the T_2 shine-through effects are reduced in (c), as well as (d). However, the visualisation of solid tumour is enhanced in (d) the T_2-cDWI (1000 s/mm^2, 0 ms) image compared with (c) DWI (800 s/mm^2, 82 ms) image. The contrast between the solid tumour versus fluid component increased from -0.23 in (c) to 0.22 in (d) when T_2-cDWI was applied[13]. An exponential image[14] with b 800 s/mm^2 is shown for comparison.

[13] Negative contrast values indicate tumour has a smaller mean signal intensity than effusion. Positive values indicate the tumour ROI has a larger mean signal intensity than the effusion ROI.

[14] An exponential image is referred to exponentially weighted DWI where only b-value and ADC are used to generate image contrast while S_0 is not considered for contrast. It can be calculated by dividing the conventional DWI image by b0 image, $S_{exp} = S(b) / S_0 = exp$ (-b*ADC).

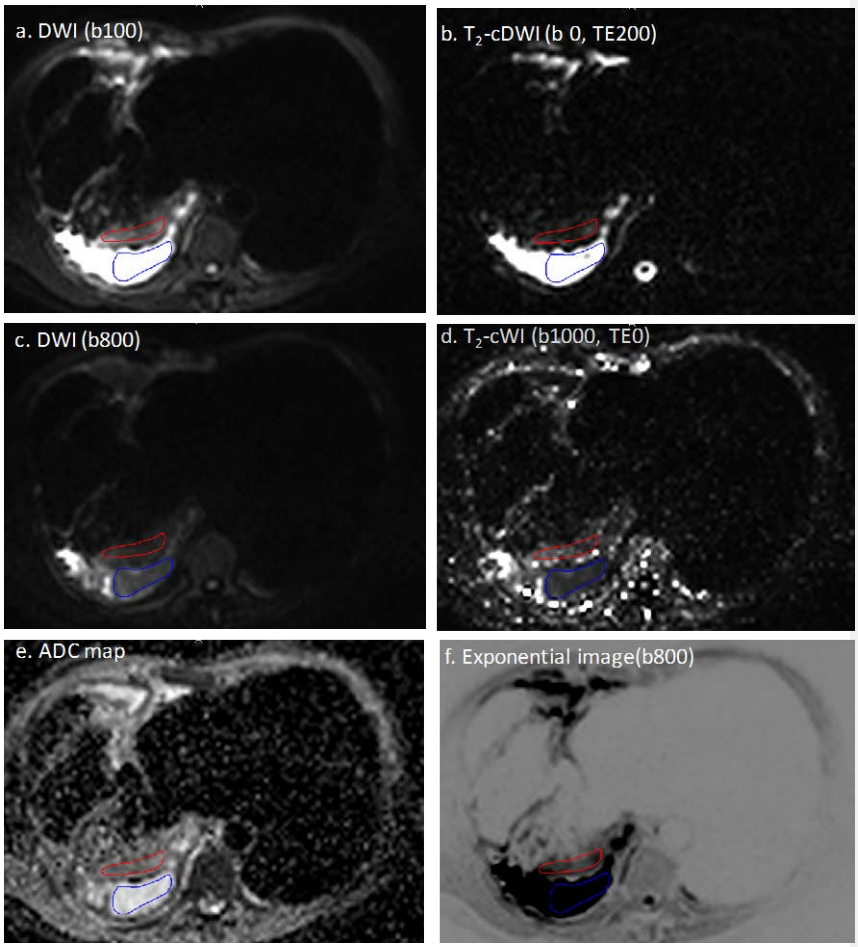

Figure 4.14: Axial DW MR images of a 69-year-old male with mesothelioma in the right lung for acquired b-values of (a) 100 and (c) 800 s/mm^2 at TE of 82ms, and (b) T_2-adjusted computed b-value of 0 s/mm^2, echo time 200 ms, and (d) T_2-adjusted computed b-value of 1000 s/mm^2, echo time of 0 ms. (e) ADC map (*10^{-3}mm^2/s) was generated from images with b-values of 100, 500 and 800 s/mm^2. (f) Exponential image with b 800 s/mm^2.

ROI of the solid tumour is marked with red and pleural effusion with blue. Compared with the acquired DW image (c), solid tumour showed greater mean signal intensity than the pleural effusion on the T_2-cDWI (d).

4.5 Discussion

A novel acquisition and post-processing method, which allows arbitrary modulation of diffusion- and T_2- weighting, has been developed to improve image contrast by varying diffusion and T2 contrast independently.

There are three things of T2-cDWI that should be noted:

Firstly, in this role, T_2-cDWI is purely a visualisation mechanism for improving image contrast for the identification of cellular tumours, and for separating confounding T_2 effects, while it is not used to predict what the true value is in the DW images. In another role, the T2-cDWI images may be considered to be comparable with conventionally acquired images using the same b-value and TE. In the context of visualisation, the employed diffusion model is not of primary concern provided that desirable tumour characteristics can be achieved.

Secondly, a joint mono-exponential diffusion model was used without consideration of perfusion contribution, but the T_2-cDWI methodology easily lends itself to alternative diffusion models with appropriate data support.

Lastly, the acquisition times for clinical studies were increased to acquire the additional T2-weighted scans; however, the additional time was modest (< 2 min for MPM patients in the study). One possible future study could explore the dependence of image quality on the choice and number of echo times.

4.5.1 The theoretical assumptions made in the development of the image acquisitions

Why b-values of 100, 500, 800 mm^2/s were chosen in the clinical image acquisition?

Taouli, [Taouli, et al, JMRI, 2016] has suggested the number of b-values should be larger than two or three for clinical purposes outside brain, for example, a low b value ($b \leqslant 100$ mm^2/s), intermediate b value ($400 \leqslant b \leqslant 500$ mm^2/s), and higher b value (between 500 to 1000 mm^2/s). In the clinical acquisition protocol, a low b-value $\leqslant$ 100 mm^2/s is preferred to image tumours in the body by radiologists in clinics, because it can avoid the IVIM (blood microcirculation) effect, suppress high signal from blood flow in the vessels, resulting in "black blood" images which are useful for detecting lesions, especially true for lesions less than 1cm in size [Maroni, et al. 2013; Taouli, et al, JMRI, 2016]. Intermediate and high b values ($\geq$500 mm^2/s) provide diffusion information used for lesion characterization [Taouli, 2003]. The b-value of 800 mm^2/s is used to avoid DWI signal intensity reaching the noise floor.

Why a mono-exponential diffusion model was chosen instead of other models (IVIM or stretched-exponential model)?

In this chapter, a mon-exponential diffusion model has been used due to the following reasons:

Firstly, IVIM model needs more b-values than what we have used in the current clinical protocol, and extra b-values could not be added in the protocol due to the scanning time limitation; with the current imaging protocol (three b-values for DWI acquisitions), the overall scanning time is about fifty minutes for each patient, thus it is impractical to extend the scanning time longer for more b-values which are acquired for IVIM model.

Secondly, due to the fact that only three samples (DW images acquired at three b-values) have been acquired, it is not enough to estimate the variables (alpha, S0, and diffusion coefficient) in the stretch-exponential models, but for mono-exponential model, it is able to estimate the two variables, S0 and D only using three samples. In fact, in our experience, the mono-exponential model is the only useful model over that range of b-values.

There is a fundamental limitation of the computed images generated from our T2-cDWI model, that is, we assume that all the diffusion signal at any b-values follows

the same model in the range of acquired b range (100 – 800 mm^2/s), but the fact is the true diffusion signal is unknown for us outside the range of acquired b-value range, it may follow mon-exponential model or it may have some undergoing kurtosis effect. We did not consider any complex diffusion effect and only used the simplest model that we could use, basically to generate some arterial diffusion weighted contrast. Therefore, the synthetic DW image at the extrapolated high b-values is only for visualisation purpose, and should not be used to predict what the true value is in the DW images.

4.5.2 Advantages of noise characteristics of T2-cDWI

In this chapter, the noise characteristics of the T_2-cDWI model have been derived through analytical approximations, and have been well validated through phantom experiments for a physiological range of ADC and T_2 values. It is interesting to find that the noise variance on T_2-cDWI images has decreased with increasing b-value and/or echo time for samples in the T_2 range of physiological tissues. This reciprocal relationship gradually became smaller than those observed on the acquired DW images in particular at high b-value and long echo times combinations. This indicates that improved SNR can be achieved by using synthetic DWI, rather than direct image acquisitions at high b/TE values. As b-values and echo times can be manipulated simultaneously using T_2-cDWI, it is feasible to enhance disease CNR by optimising the b-value and echo time for the disease/tissue of interest. In particular, a rise in the T_2-cDWI noise level was found at small b-value, which is due to the typically smaller number of signal averages at b = 0 s/mm^2, compared with non-zero b-values [126].

4.5.3 Clinical application of T2-cDWI

The clinical examples showed that T2-cDWI was able to independently vary the image contrast derived from T_2 and diffusion by computation of images at desired b-values and echo times. Compared with acquired high-b-value images, T_2-cDWI with a large b-value and small/zero TE provides efficient suppression of the T_2 shine-through effect, and results in higher contrast for identifying true impeded diffusion areas (e.g. tumour). Conversely, T_2-cDWI with a low b-value and a long echo time enhances areas with long T_2-relaxation (e.g. fluid, effusion, cystic disease, and

necrosis) since the signal from regions with shorter T_2 are effectively suppressed. Therefore, there is a greater degree of freedom in adjusting the image contrast by manipulating b-values and echo times independently with T_2-cDWI compared with conventional DW imaging. In this way, T2-cDWI may prove to be a useful clinical tool to enhance/eliminate the T_2 shine-through effect, thereby improving image contrast to enhance tumour detection. Although this has not been investigated in this study, the early proof of concept data appears promising. In the future prospective studies, this need to be investigated, for example, radiologists could review the conventional DWI image and T2-cDWI images separately using a four-point scale (4 = excellent, 3 = good, 2 = moderate, 1 = poor) to compare their roles in tumour detection.

T_2-cDWI would also be useful in a multiple centre setting. TEs and b-values in the multi-centres could be made equivalent for radiological reading, thus the impact of minor variations in acquisition protocols can be minimised.

In addition to aiding clinical image interpretation, T_2-cDWI may facilitate automated/semi-automated feature segmentation based on the enhanced CNR. Furthermore, the quantitative water T_2 values estimated from the T_2 and diffusion-weighted images may also be applied as independent measures for tumour classification using joint ADC-T_2 histograms.

4.5.4 Comparing T2-cDWI with other approaches

Other studies have investigated the use of exponential images to eradicate T_2 shine-through effects by removing the S_0 component for conventional cDWI [127; 128]. However, these images are associated with poor SNR and are not able to independently vary the relative contributions of both tissue diffusivity and T_2 relaxivity. Relaxation-corrected DWI [106] and short-TE cDWI [129] were used to correct for the T_2 shine-through effect; however, T_2-cDWI is able to provide synthetic images at any b-value and/or echo time. In another study, an ADC-dependent voxelwise cDWI (vcDWI) was proposed to improve SNR and reduce T_2 shine-

through effects [130], but without taking into account variations in tissue T_2-relaxation times.

4.6 Chapter summary

The T2-cDWI model takes into account both ADC and the T2-relxation time, it can be used to enhance or remove diffusion T2 contrast. This is achieved by acquiring additional T_2-weighted EPI images at different echo times. Using the identical EPI readout ensures that the geometry and B_0-related distortions are inherently matched between the T_2- and diffusion-weighted images. The clinical examples showed T2-cDWI was able to independently vary the image contrast derived from T_2 and diffusion, by computing images at desired b-values and echo times. In conclusion, T_2-cDWI has been shown to provide both objective and quantitative improvements in image noise and contrast. T2-cDWI appears to be a promising approach for improving image contrast and tumour detection using body diffusion-weighted MRI.

Some findings in this chapter were from the publication: Cheng, L., Blackledge, M.D., Collins, D.J., Orton, M.R., Jerome, N.P., Feiweier, T., Rata, M., Morgan, V., Tunariu, N., Leach, M.O. and Koh, D.M., 2016. T2-adjusted computed diffusion-weighted imaging: A novel method to enhance tumour visualisation. *Computers in biology and medicine*, *79*, pp.92-98.

5 Image segmentation in malignant pleural mesothelioma on DWI

5.1 Introduction

Malignant pleural mesothelioma (MPM) is difficult to measure radiographically due to its unique rind-like growth pattern. In addition to the existence of the solid tumours, pleural effusion is one of the most common findings in MPM patients, occurring in up to 74% of patients [3]. In diagnosis, staging, and treatment planning in MPM, CT is the routine imaging modality for MPM due to its wide availability and relatively low cost. The current standard method used in treatment effectiveness evaluation in MPM is the Modified Response Evaluation Criteria in Solid Tumour (modified RECIST) [40] using CT images. It measures tumour thickness perpendicular to the chest wall or mediastinum in two sites at three different levels on transverse images from a CT scan. The sum of these six measurements is defined as the pleural uni-dimensional measure and used to represent the tumour at a specific time point. Such simple size measurement criterion, limited to only six uni-dimensional changes of tumour during treatment, neglects the tumour shape can be highly complex in MPM. Current evidence shows that the modified RECIST is associated with a high degree of inter- and intra-observer variations in practical settings [4]. Volumetric analysis of MPM may minimise inter-observer variability which is highly desirable for treatment evaluation and follow-up observation. Unfortunately, manual contouring of MPM is a highly labour-intensive and time-consuming due to the thin, rind-like shape of MPM and the large number of slices in each image acquisitions. In addition, manually contouring heavily depends on the clinical experience of the radiologist and may be prone to large inter-observer variation. Therefore, there is an urgent need for the development of (at least) semi-automatic for MPM in order to (i) accelerate volumetric measurements and (ii) provide potentially accurate estimates of tumour burden.

In addition to the above considerations, CT has poor soft tissue contrast, limiting its used for detecting early local tumour extension. As explored in Chapter 3, the image contrast in DWI is sensitive to the net displacement of water molecules during thermal agitation (diffusion), and so in tissues where there is a greater hindrance to the

diffusion of water molecules, DWI signal can be higher when compared with tissues in which water is allowed to freely move. This contrast mechanism has shown considerable utility for the visualisation of cancer within the body [101], which is typically associated with a high cellularity (number of cells per unit volume) and can thus impede the diffusion of water within the interstitial space to greater extent than surrounding healthy tissue (when there is no T2 shine-through effect). A principle hypothesis of this thesis is that DWI can be used to generate exquisite contrast between MPM and healthy tissues including the lung and chest wall.

In this chapter, two semi-automatic methods for delineation of MPM are implemented on DWI images, namely: (i) the GrowCut algorithm [131], and (ii) the Random Walk algorithm. Both algorithms require the use of manually defined 'seeds' within foreground (MPM disease) and background regions within Diffusion Weighted MR-images.

There are three goals of this chapter:
1. To introduce and demonstrate the theory of the segmentation of MPM disease volume using GrowCut and Random Walk methods;
2. To implement the GrowCut and Random Walk segmentation to clinical diffusion-weighted MRI images;
3. To evaluate if GrowCut/Random Walk segmentation can achieve a good segmentation accuracy compared with the reference disease volume.

The chapter is organised as follows:
It starts with a description of the theory of image segmentation and how the mathematical models of the GrowCut and random walk are applied to the problem of image segmentation (**Section 5.2**). In **Section 5.3**, segmentation in 2D using the GrowCut and random walk methods are illustrated on some example DW images. Subsequently, a volumetric extension of the methods is presented on a clinical patient dataset in **Section 5.4**. And also, the applicability of the methods has been performed in a clinical MPM DWI cohort and the dice coefficients have been illustrated between the tumour volumes generated from semi-segmentation methods and the reference

tumour volume defined by manual segmentation. Finally, **Section 5.5** and **5.6** discuss and summarise the whole chapter.

5.2 Semi-automatic segmentation of malignant pleural mesothelioma

5.2.1 Basic Theory of Image Segmentation

Image segmentation is defined as the process of partitioning an image into a finite number of non-overlapping regions, where within each region, pixels are similar with respect to some characteristic or property, such as colour, intensity or texture. Given an image *I* and its domain Ω_I a K-class segmentation can be illustrated as the process of assigning a label k to every pixel belonging to the kth set within the domain: $S_k \subset \Omega_I$ (the union of all sets is the entire domain, $\Omega = \cup_{k=1}^{K} S_k$). Segmentation methods are typically used to find the objects and boundaries in the image where regions of interest are desired.

When the constraint that regions be connected is removed, then determining the sets S_k is called pixel classification, and the sets themselves are called classes. Pixel classification, rather than classical segmentation, is often a desirable goal in medical images, particularly when disconnected regions belonging to the same tissue class require identification. Determination of the total number of classes K in segmentation can be difficult. Often, the value of K is assumed to be known based on prior knowledge of the system being considered. In this chapter, a two-class segmentation (K = 2) is assumed to represent (i) mesothelioma disease, and (ii) all other (background) tissues. The dimensionality of a segmentation method refers to whether it is 2D (planar) or 3D (volumetric).

5.2.2 GrowCut

The GrowCut algorithm was developed as an interactive technique for multi-label segmentation of N-dimensional images, proposed by Vezhnevets and Konouchine in 2005 [131]. The segmentation strategy, which is modelled on the theory of cellular automata, captures and assigns labels to neighbouring pixels with similar statistical properties to the user-defined seed points. The GrowCut algorithm is relatively easy to implement and fast to compute, and supports multi-label segmentation within images of arbitrary dimensions. Moreover, GrowCut is able to achieve good segmentation in complex situations [131]. GrowCut based algorithms have been successfully implemented on many platforms, such as *3D Slicer* [133; 134], Matlab[15], Photoshop[16] and ImageMagick[17]. Some clinical studies have shown GrowCut has good performance in segmenting clinical diseases [135].

Cellular automata (CA)

A cellular automaton is a discrete model which consists of cells on a regular lattice (in image processing the cells are considered to represent pixels). Formally a cellular automaton can be defined as a triplet: $A = (S, N, \delta)$, where S is a non-empty cell state set, N is the cell neighbourhood system, and δ: $S^N \rightarrow S$ is the local transition function. This transition function changes the state of cell, S, at the current time step, is a function of the states of the neighbouring cells, S^N, at the previous time step [132]. Each cell, p, has a specific cell state set, S_p, of finite size. The simplest such state is the binary set, such that $S_p \in \{0,1\}$. The state set used in the application here has two elements corresponding to foreground and background. The neighbourhood system defines which cells are adjacent to a given cell. Examples of such neighbourhoods include the von Neumann and Moore neighbourhoods (Figure 5.1).

The von Neumann neighbourhood consists of the nearest four orthogonally adjacent cells to a given cell (i, j):

$N_{i,j} = \{(k, l) : |k - i| + |l - j| \leq 1\}$

[15] http://www.shawnlankton.com/2008/03/growcut-segmentation-in-matlab/
[16] http://www.growcut.com/
[17] http://im.snibgo.com/growcut.htm

whilst the Moore neighbourhood consists of the nearest eight adjacent cells surrounding a given central cell (i, j):

$N_{i,j} = \{(k,l) : |k-i| \leq 1 \; and \; |l-j| \leq 1\}$

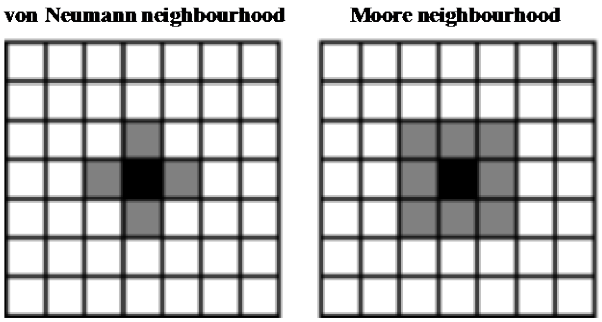

Figure 5.1: examples of two simple neighbourhoods used in the theory of cellular automata.

In the left image, the grey cells demonstrate the von Neumann neighbourhood for the black cell, whilst for the right image the grey cells depict the Moore neighbourhood for the black cell.

The GrowCut algorithm

For pixel p, the state set S_p can be expressed as a triplet $S_p = (l_p, \theta_p, \vec{C}_p)$, where l_p is the label of the pixel (representing (i) foreground/disease and (ii) background in this work), θ_p quantifies the 'confidence' that the current pixel p belonging to class l_p (set to the range $\theta_p \in (0,1)$ without loss of generality), and the cell feature vector $\vec{C}_p$ depicts the pixel value in terms of image intensity of colour (in this case $\vec{C}_p$ is a scalar representing the DW-image intensity).

An unlabelled image is initially considered labelled as "empty" for all pixels and their strength values are set to zero. In this application, the value of the cell feature vector C is the signal intensity of the pixel for medical images.

$$l_p = 0, \qquad \theta_p = 0, \qquad \vec{C}_p = SI_p$$

The Grow-cut algorithm is initialized by the user manually labelling a subset of pixels within the image (so-called ‘seeding’). These pixels are all initialised with the corresponding label and a confidence value of $\theta_p = 1$. All remaining, non-seeded pixels are given confidence values of $\theta_p = 0$. The algorithm proceeds by looping through each pixel in the image, where for each iteration, the pixel *p* is ‘attacked’ by its neighbours, q. The strength of the attack depends on both the confidence values of the neighbours θ_q and the difference in pixel value. If the strength of the attack is larger than the confidence of the pixel *p*, that pixel will change its label to the label of its attacking neighbour. The GrowCut algorithm will proceed to iteratively loop through all pixels until the labelling scheme converges to a stable solution Pseudo-code for the Grow-Cut algorithm is shown below [132]. Here p is a pixel in image *P*, q is a pixel in the neighbourhood of the pixel p: N(q). At step *t*, the label for pixel p is denoted as l_p^t, and the strength of the pixel as θ_p^t.

Pseudo code of GrowCut algorithm:

```
// For each cell p
for all p in image
    // Copy previous state
    l_p^{t+1} = l_p^t
    θ_p^{t+1} = θ_p^t
    // Neighbour pixels q try to attack the current cell p
    for all neighbours q
        if g(||C_p − C_q||_2) · θ_q^t > θ_p^t
            // Update state at p
            l_p^{t+1} = l_q^t
            θ_p^{t+1} = g(||C_p − C_q||_2) · θ_q^t
        end if
    end for
end for
```

A suitable choice of attacking strength function $g(x) \in (0, 1)$ is required. As suggested in the original GrowCut paper, this thesis uses the definition:

$$g(x) = 1 - \frac{x}{max\|\vec{C}\|_2}$$

where $max\|\vec{C}\|_2$ represents the absolute difference between the maximum and minimum signal intensities in the DW-image being segmented.

5.2.3 Random Walk

Random walker segmentation algorithm is an interactive segmentation method proposed by Leo Grady in 2006 [136], which is based on anisotropic diffusion from user-defined seeds, where the local diffusivity is a decreasing function of the image intensity gradient. Random walk segmentation determines the labels of unlabelled pixels by resolving the question: what is the probability that a random walker starting at each unlabelled pixel first reaches one of the pre-defined labels? After computing these probabilities for each pixel, the image segmentation will be obtained by assigning the label with the greatest probability to each pixel. Random walk segmentation can be rapidly computed by solving a spare linear system. More importantly, it is robust to weak or missing boundaries in noisy images by avoiding having the random walker cross sharp image intensity gradients, so it is an effective interactive way of segmenting difficult pixel maps. In the following subsection, the random walker image segmentation algorithm will be reviewed.

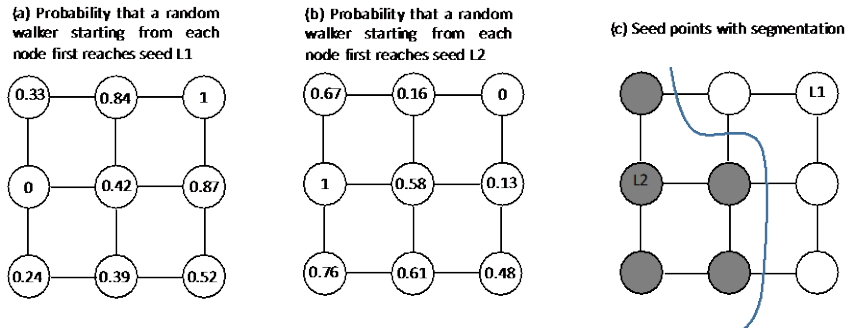

Figure 5.2: Illustration of the random walk-based segmentation for a 3x3 image of unit weights with two seed points representing two different labels (L1, L2).

Individual seeds are sequentially set to unity. The probability of a random walker starting at each of the unseeded nodes reaching the unity seed first

instead of the other seeds is then determined and given in the circles. Note that because of this the two probabilities (from the two seeds) for each node always sum to one. The nodes are classified based on which seed label yields the highest probability, as shown in (c).

Graph

An image can be modelled as a **graph G** with nodes and edges, and is defined as following

G = (V, E)

where graph **nodes** $v \in V$ correspond to the image pixels, and **edges** $e \in E \subseteq V \times V$ are connected by two neighbouring pixels, and will be assigned with a weight ω presenting the image intensity similarity between the two nodes.

Edge weights and degree

In Grady′s paper, a Gaussian weighing function [136] was used to compute the **weight** ω_{ij} for edge e_{ij} connecting nodes v_i and v_j:

$$\omega_{ij} = exp\left(-\beta\left(g_i - g_j\right)^2\right) \quad \textbf{(5.1)}$$

where β is the only free parameter that the user chooses, g_i and g_j are the image intensities at pixel i and j respectively. The weight is assumed positive on an undirected graph, that is, $\omega_{ij} > 0$, $\omega_{ij} = \omega_{ji}$. The weight ω_{ij} can be considered as a likelihood that a random walker will cross the edge e_{ij}, a small weight may mean that the random walk may be less likely to cross the edge while a large weight means more likely.

The **degree** of a node v_i is defined as the sum of the edge weight ω_{ij}, where the edges e_{ij} are those edges connecting v_i and its neighbouring nodes:

$$d_i = \sum \omega_{ij}$$

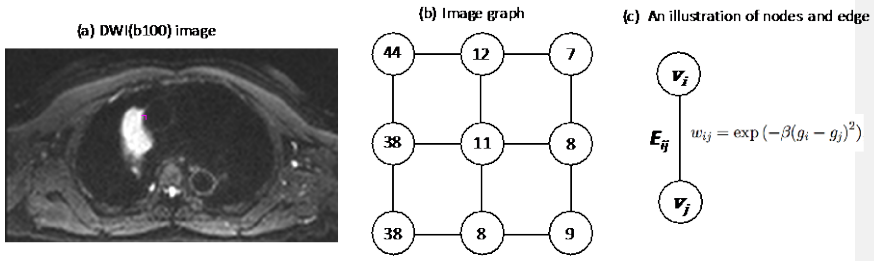

Figure 5.3**: (a) An DWI image acquired at b=100. The red ROI is 3*3 pixels square ROI. (b) The sub graph is generated from ROI in image (a), containing 9 nodes and 12 edges. (c). An illustration of the nodes and edge.**

Discrete Dirichlet problem

Previous studies [137] [138] have proved that finding the probability that each node sends a random walker to first reaches a seed point is equal to solving a combinatorial Dirichlet problem with given boundary conditions.

The **Dirichlet integral** is defined as follows for a field u and region Ω:

$$D[u] = \frac{1}{2}\int_{\Omega} |\nabla u|^2 \, d\Omega \qquad (\mathbf{5.2})$$

Harmonic function is a function that minimises the Dirichlet integral and it satisfies the Laplace equation, $\nabla^2 u = 0$.

Dirichlet problem is the problem to find a harmonic function which satisfies the Laplace equation for a given set of boundary conditions.

To solve the harmonic function u, the **combinatorial Laplacian matrix L_{ij}** is introduced:

$$L_{ij} = \begin{cases} d_i, & if\ i = j \\ -w_{ij}, & if\ \ v_i\ and\ v_j\ are\ adjacent\ nodes \\ 0, & ot\boxtimes erwise \end{cases} \qquad (\mathbf{5.3})$$

With all these definitions, the graph discrete version of Dirichlet integral (**combinatorial Dirichlet integral**) (**Eq.5.2**) is:

$$D[x] = \frac{1}{2}x^T Lx = \frac{1}{2}\sum_{e_{ij}\in E}\omega_{ij}\left(x_i - x_j\right)^2 \quad (\mathbf{5.4})$$

where x is the combinatorial harmonic function and minimizes Eq.5.10 to find the probabilities for all nodes. x_i is the probability that a random walker starting at node v_i first reaches a labelled seed. This combinatorial Dirichlet integral is the objective function in random walk segmentation and the likelihood for node v_i is estimated by minimizing the objective function on the basis of the labelled nodes.

After user pre-marked some seeds in the image, all the nodes in the graph are divided into two sets, V_M and V_U: $V_M \cup V_U = V$ and $V_M \cap V_U = \varnothing$. V_U contains all the unmarked nodes.V_M contains all the user-marked seed nodes regardless of their labels and they act as boundary conditions for the Dirichlet problem, as their probabilities that a random walker starting at a seed node reaches itself are one.

Without loss of generality, the matrix x and L are reordered as V_M in front of V_U as

$$x = \begin{bmatrix} x_M \\ x_U \end{bmatrix}$$

$$L = \begin{bmatrix} L_M & B \\ B^T & L_U \end{bmatrix}$$

where $x_M$and x_U are the probabilities of the marked seeds V_M and unmarked nodes V_U respectively. L_M corresponds to the parts of the matrix L describing the dependencies between all the marked seed points V_M while L_U is the part of L describing the relationships between all the unmarked nodes V_U. B is the part of the matrix L describing the coupling between the marked and unmarked nodes, while B^T describes the relationship between the unmarked nodes and the marked nodes.

Equation 5.4 is decomposed into:

$$D[x_U] = \frac{1}{2}\begin{bmatrix} x_M^T & x_U^T \end{bmatrix}\begin{bmatrix} L_M & B \\ B^T & L_U \end{bmatrix}\begin{bmatrix} x_M \\ x_U \end{bmatrix} = \frac{1}{2}\left(x_M^T L_M x_M + 2x_U^T B^T x_M + x_U^T L_U x_U\right) \quad (5.5)$$

Differentiating **Eq5.5** with respect to x_U, yields the random walk solution,

$$L_U x_U = -B^T x_M \tag{5.6}$$

Assume there are *K* classes marked seeds by the user, the probability of any node v_i belonging to a label, *s*, is denoted as x_i^s, and the sum of the probabilities at any node v_i for K classes labels is one, $\sum_s x_i^s = 1, \forall v_i \in V$.

Denoting an overall seed vector m^s for each label, s, at node $v_j \in V_M$ as

$$m_j^s = \begin{cases} 1, & if\ Q(v_j) = s \\ 0, & if\ Q(v_j) \neq s \end{cases}$$

where $Q(v_j)$ is a function representing the set of labels for the seed points, and $Q(v_j) = s$, $\forall v_j \in V_M$, such that $s \in Z$, $0 < s \leq K$.

Therefore, for label *s*, the solution to the combinatorial Dirichlet problem may be found by solving

$$L_U x^s = -B^T m^s \tag{5.7}$$

for one label,

$$L_U x_U = -B^T x_M \tag{5.8}$$

for all labels, where *X* has *K* columns taken by each x^s and *M* has columns given by each m^s.

In this work, there are two labels (K = 2), "foreground" and "background", and assign $x_m = 1$ for "Foreground" markers, and $x_m = 0$ for "Background" markers, the aim of random walk segmentation is to find the probability that the random walker starting at each unseeded pixel will reach a labelled "foreground" seed before a labelled "background" seed. This can be solved by using **Eq5.7**. If this probability is greater than 0.5, then this pixel is assigned with the label "foreground", otherwise, it is labelled as the background.

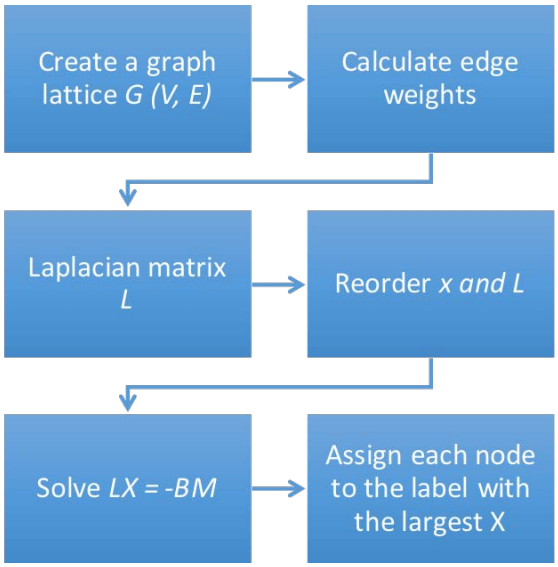

Figure 5.4: the workflow of Random walk segmentation

To summary, the steps of the random walk algorithm are:

I. Map the image intensities to the edge weights, ω_{ij}, in the lattice using **Eq. 5.1**;
II. Find Laplacian-based weights, ***L***, using **Eq. 5.3;**
III. Obtain the marked seeds, V_M, and reorder them according the K labels;
IV. Solve **Eq. 5.8** for the probability X;
V. Obtain the final segmentation by assigning the label with the maximum probability to each pixel.

5.2.4 Figure of Merits for performance evaluation: Dice coefficient

Performance evaluation of the segmentations is done by comparing the regions of interest (ROIs) obtained from both semi-automatic segmentation techniques (GrowCut and Random Walk) with the reference regions which were manually segmented. The volumes from both semi-automated methods and the reference images were all saved as binary images where the disease voxels are labelled as 1 and the remaining are 0, and the similarity of the two was compared using the Dice

Coefficient. The Dice Coefficient (D) measures the relative volume overlap between two binary volumes and it is calculated as follows:

$$D = \frac{2|A \cap B|}{|A| + |B|}$$

where $|A|$ and $|B|$ are the binary masks from either segmentation method and the reference image respectively, and $|A \cap B|$ is the union of two binary masks $|A|$ and $|B|$.

5.3 Applying GrowCut and random walk to 2D DWI images

5.3.1 GrowCut

GrowCut has been implemented in OsiriX (Pixmeo, Geneva, Switzerland) as a plugin developed by Dr. Blackledge at the ICR. This plugin is simple to install, and has a user-friendly interface to enable drawing and modifying the foreground and background seeds using the OsiriX brush tool. As seen in the tool interface in Figure5.5, there are 2D and 3D options for segmentation; 2D segmentation only uses four neighbouring pixels in the same slice, 3D segmentation extends to the neighbouring two slices with six neighbouring pixels in total (von Neumann neighbourhoods).

GrowCut segmentation in 2D is illustrated on a phantom and a mesothelioma patient in **Figure 5.5** and **Figure 5.6** respectively.

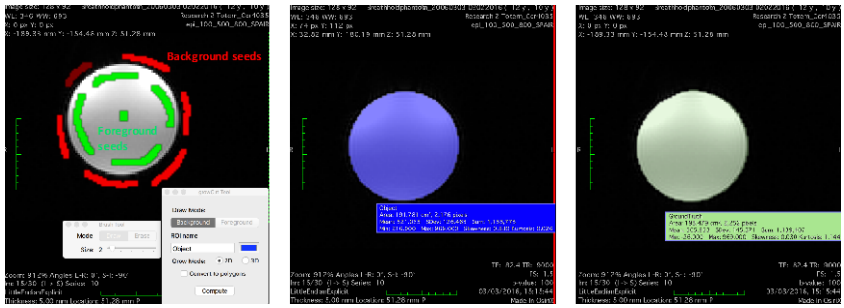

Figure 5.5: Illustration of the use of the GrowCut tool in OsiriX segmenting a phantom on a DWI (b = 100 s/mm^2) image.

The left-hand image shows the interface of GrowCut with the option to segment objects on 2D/ 3D images. The red represents the pre-defined background seeds and the green represents the foreground seeds. The middle image shows the result of 2D GrowCut segmentation and the right-hand image shows the ground truth.

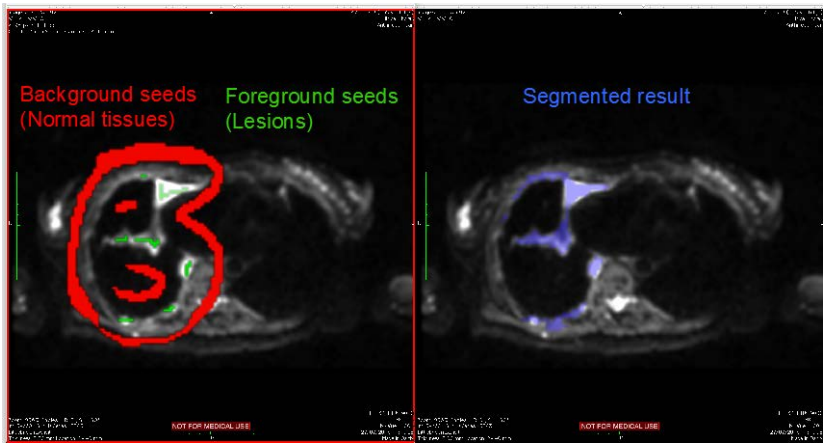

Figure 5.6: Demonstration of the implement of GrowCut segmentation tool on one axial slice of DWI (b =100 s/mm^2) image of a 64-year-old male patient with malignant mesothelioma in the right lung. In the left-hand side image, the foreground seeds (Green) were drawn in MPM lesions while the background

seeds (Red) in the normal tissues. The GrowCut segmentation outcome was shown in blue in right hand side image.

5.3.2 Random walk

In this work, the random walk segmentation has been implemented by mainly using a random walker function[18] available in Python using the scikit-image[19] library. An in-house plugin pyOsiriX[20] [123], developed by Dr. Blackledge in our team, enables to run the python script in Osirix Dicom Viewer (Pixmeo, Geneva, Switzerland).

The optimal beta value for segmentation

The edge weight defined in **Eq.5.1** plays an important role in the random walk segmentation algorithm, and requires the specification of β, which is the penalization coefficient for the random walker motion. This is the only free parameter that the user chooses and it specifies how hard for the random walker to cross the edge connecting the two nodes in the graph. The larger beta is, the harder to cross.

To find an optimal value for β in the 2D segmentation, we evaluated the proposed RW algorithm on DWI (b = 100s/mm^2) images with a PDMS phantom, from which contains thirty slices with manual segmentations are used as the ground-truth. For each slice, the RW segmentation was applied based on the drawn seeds with beta from 0 to 5000, and the Dice coefficient was calculated at each beta value. The ground-truth, seeds, and segmentation outcomes of one example slice (Slice 15) were illustrated in **Figure 5.7**. The mean Dice coefficient of all the thirty slices was plotted against each beta in **Figure 5.8**. The overall performance of the Random walk is good as all the Dice coefficients are over 0.9, particularly in the range of Beta= (1000, 2800)

[18] http://scikit-image.org/docs/stable/api/skimage.segmentation.html - skimage.segmentation.random_walker
[19] https://scikit-image.org/
[20] https://sites.google.com/site/pyosirix/home

with the Dice coefficient over 0.97. The best performance is achieved when beta = 2400.

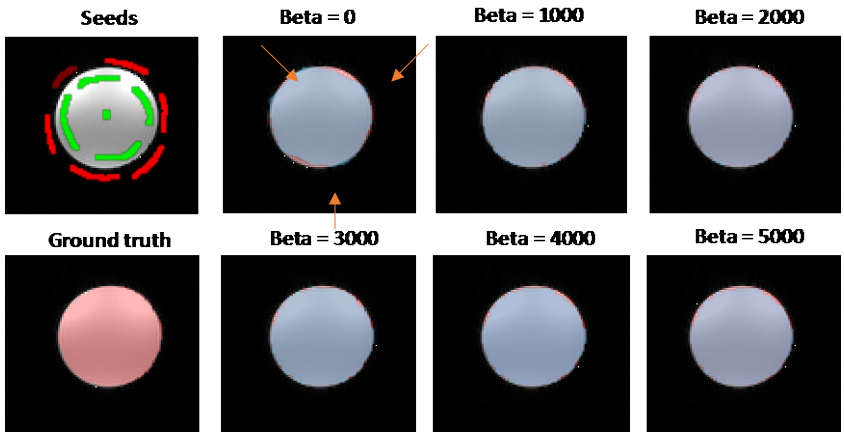

Figure 5.7: The upper-left corner shows the seeds for the Random walk segmentation of a phantom on a DWI (b = 100 s/mm^2) image (slice number 15) (Red: Background; Green: Foreground)); The lower-left corner shows the manually defined ground truth ROI. The remaining images are the images with the segmented outcome at different beta values from 0 to 5000 overlaid on the ground truth segmentation (Red).

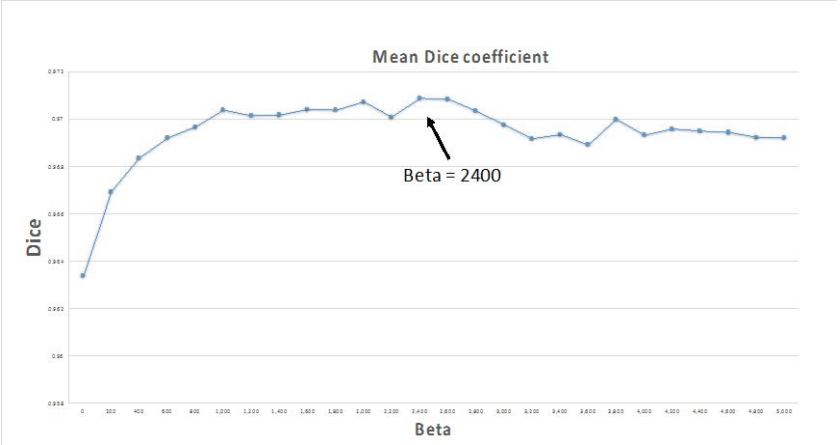

Figure 5.8:The plot of the mean dice coefficient of thirty slices of the DWI images against beta when using the Random walk tool to segment the phantom is 2D. The overall performance of the Random walk is good as all the Dice coefficients are over 0.9, particularly in the range of Beta= (1000, 2800) with the Dice coefficient over 0.97.

5.4 Repeatability of GrowCut and Random walk segmentations

Section 5.3 has illustrated how the two semi-automatic segmentation methods have been applied on the 2D DWI image to acquire the tumour region, while how well they perform repeatedly is still unknown, so the aim of this section is to investigate the repeatability of the two semi-automatic segmentation methods on 2D DWI images. In this study, the DWI images of 10 MPM patients have been used (details of these patients and scan protocol can be found in Chapter 7). The seeds, including back- and fore-ground seeds drawn on the normal tissue and tumour tissue respectively, have been manually drawn on the thirtieth slice at the mean b-value 100 images[21], then GrowCut or Random Walk segmentation were applied with the seeds to acquire the

[21] b100 s/mm^2 images were chosen as both solid tumour and pleural effusions had the highest signal intensities whilst maintaining good disease/background contrast among all DW images.

disease regions. The repeatability of tumour volume in the two measurements was evaluated by using the Bland-Altman method [142]. The Coefficient of Variation (CV) [143] of the log-transformed of the volumes was used to measure the repeatability of the disease volumes:

$$CV = 100\% \times \sqrt{\exp\left(\left(\sum d^2\right)/2N\right) - 1}$$

where d is the difference of the log-transformed paired measurements and N is the number of patients.

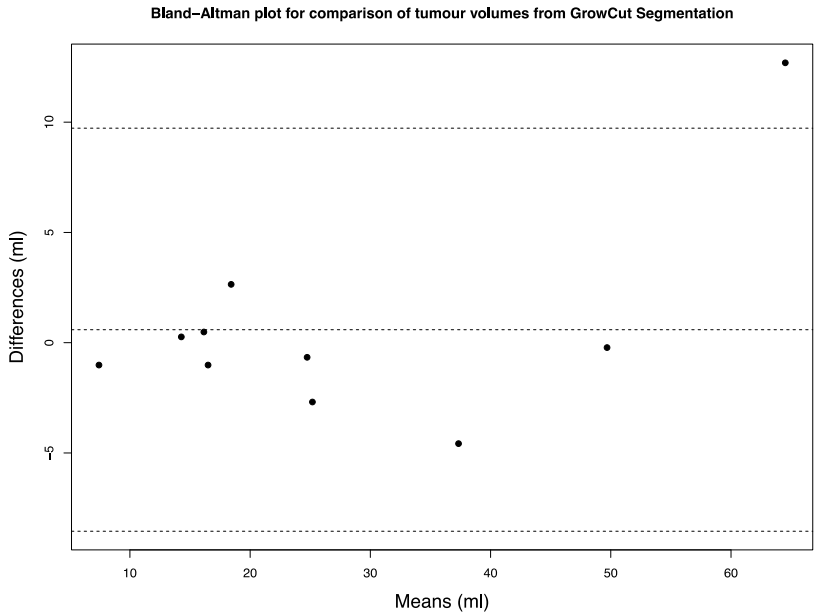

Figure 5.9: Bland Altman plots for comparison of the tumour volumes generated from GrowCut segmentation. Horizontal middle dash line in the plot represents the mean difference (bias) and the two dash lines are the 95% limits of agreement (LoA).

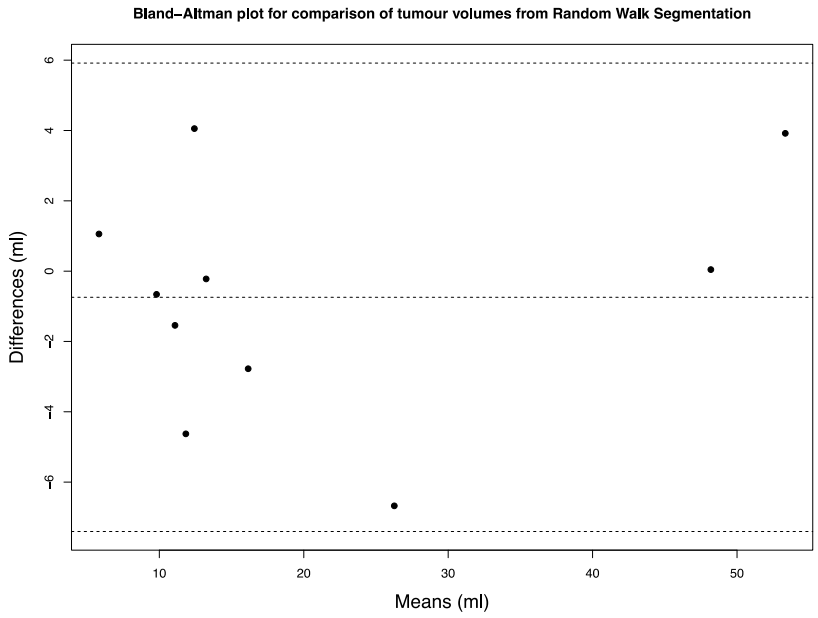

Figure 5.10: Bland Altman plots for comparison of the tumour volumes generated from Random Walk segmentation. Horizontal middle dash line in the plot represents the mean difference (bias) and the two dash lines are the 95% limits of agreement (LoA).

Figure 5.9 and **5.10** shows the Bland-Altman plots to evaluate the variability of the tumour volume acquired from GrowCut and Random Walk. CVs of the tumour volumes is 7.4 (95% confidence intervals (CIs): 5.2 - 13.1) and 14.6 (CI: 10.2 - 25.9) for GrowCut and Random Walk segmentations, respectively, which indicates a good repeatability of the two semi-automatic segmentations. In particular, GrowCut features smaller CVs Random Walk. The ICC (95% CI) is very good for both methods, with 0.985 (0.945-0.996) for GrowCut and 0.954 (0.837 – 0.9880) for Random Walk.

Discussion:

In terms of tumour burden on the 2D images, the repeatability of the whole tumour from both segmentation methods is good. The worse case of the CV (Random Walk) is only 14.6%, which indicates very good repeatability of the semi-segmentation methods. Comparing bwtween the two methods, the CV of Random Walk is two

times higher than that of GrowCut, and also the bias and limits of agreement for GrrowCut are lower compared to the Random Walk, which means GrowCut have a higher repeatability than Random Walk method in this cohort. Low CVs and 95% LoA mean that both of our methods are highly repeated when applying on 2D DWI images, which offers good clinical tools for radiologists to evaluate the tumour burden of MPM in a fast and highly repeatable way.

5.5 Applying GrowCut and Random Walk to 3D DWI images

In Section 5.3, image segmentation was applied on the 2D DW image, where the connectivity of a 2D lattice is the 4-connected case (such as the von Neumann neighbourhood shown in Figure 5.1) without considering the information from neighbouring slices. When segmenting the full volume the simplest connectivity of a 3D lattice, the 6-connected case, is used, where extra information will be collected from the nearest slices containing the seeds. In this section, a volumetric extension of the two segmentation methods is applied on the DWI images of 10 mesothelioma patients (details of these patients can be found in Chapter 7). Two volumes-of-interest (VOIs), V_{GC} and V_{RW}, were acquired by respectively applying the GrowCut and Random Walk with the same initial seeds in 3D. The reference VOI, V_R has been acquired through manual segmentation by the author who had over four years in the field of imaging pleural mesothelioma. The dice coefficients of segmented volumes (V_{GC} and V_{RW}) against the reference volume V_R were calculated for each patient. DWI imaging was performed on a 1.5T MR scanner (Avanto, Siemens Healthcare, Erlangen, Germany) using the sequence parameters shown in **Table 7.3**.

An example patient (Patient 8) (**Figure 5.9**) both methods have good performances but there are slight differences (shown by arrow). The Dice coefficients of this patient are good for both segmentation methods, which is 0.78 for the Random Walk segmentation and 0.82 for the GrowCut segmentation.

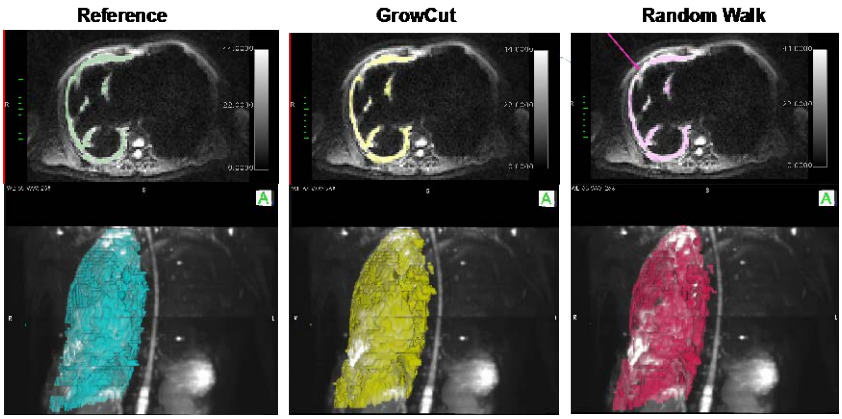

Figure 5.11: The reference, GrowCut segmentation outcome, and Random walk segmentation outcome shown in one example image slice (Upper row) and in full volumes in Maximum intensity projection (MIP) of DWI (b = 100 s/mm^2) images (Lower row).

The results of Dice coefficient for each patient are shown in **Figure 5.10**. The average Dice coefficients of the V_{GC} and V_{RW} against V_R is 0.81 and 0.80, respectively and the range of Dice coefficient are 0.76 – 0.92 and 0.75 – 0.88 for GrowCut and Random Walk methods, respectively, indicating good agreements between the semi-segmentation volumes and the reference volume. GrowCut has slightly higher Dice values in the eight out of ten patients than Random Walk, however, this should be further investigated in the future study with a larger patient cohort.

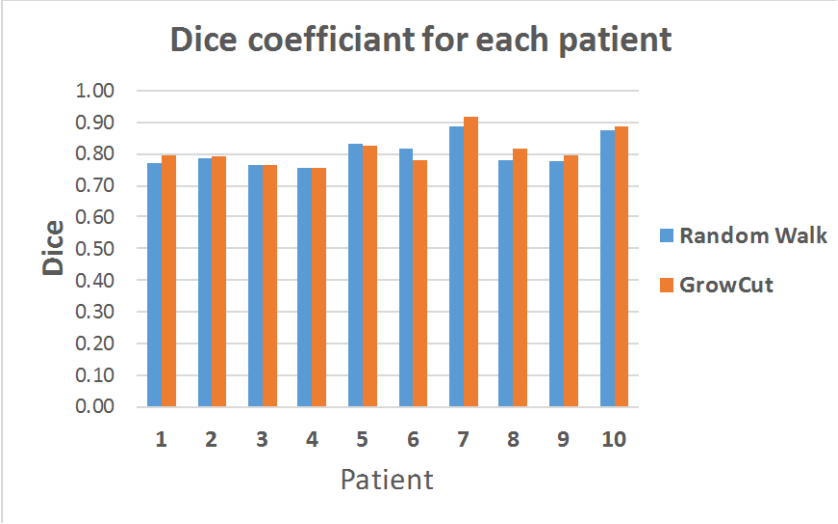

Figure 5.12: Dice coefficient of GrowCut and Random Walk segmentations against the reference for each patient.

5.6 Discussion

In this chapter, two semi-automatic segmentation methods, GrowCut and Random Walk segmentations, have been introduced to acquire the whole disease volume of MPM on Diffusion-weighted images, including solid disease and pleural effusion. To our knowledge, this is the first study to apply semi-automatic segmentation on the DW images of mesothelioma patients.

The two methods have been successfully implemented on the 2D and 3D DWI images using the in-house developed plugins in the OsiriX DICOM Viewer. There are two reasons we chose to apply segmentation in OsiriX: firstly, Osirix is a very powerful medical image viewing tool; it has a user-friendly interface and it is very easy for radiologists to view DICOM images, draw/save ROIs and make a report etc. Foremore, OsiriX enables imaging processing by using pre-installed plugins, such as ADC estimation, T2 estimation, image segmentation/ registration. When using the GrowCut segmentation plugin, the user can draw and erase the fore- and back-ground

seeds using the brush tool provided by OsiriX and thus generate 2D or 3D segmentations automatically by clicking "Compute" in the GrowCut panel. Random walk segmentation has been achieved by running the python scripts via the pyOsirix plugin and is also highly automatic with only one free parameter pre-set by the user. In order to find out the optimal parameter β, the performance of Random walk segmentation at different β values has been evaluated by DICE coefficient. The results showed high accuracy of RW segmentation in the range of β from 0 to 5000, with the best performance at 2400.

The two semi-automatic segmentations have been extended into the 3D domain to acquire the volume of the mesothelioma disease. After being successfully applied on ten clinical cases with the same initial seeds, both methods have been shown to have a good performance and an accuracy. The high Dice coefficients in the clinical data mean high accuracy of segmented volumes, indicating it is available to apply both methods into the clinical application.

There are a number of limitations of this study should be addressed, firstly, there are some drawbacks with the design of the reference volumes for all the patients in this chapter: (a). The operator of the manual segmentation of the reference volume is the author of this thesis instead of a radiologist; (b) the reference volume has only been applied by one operator without repeated measures; (c) the operator was not blind to the results of the semi-segmentation. The reason for (a) and (b) is that it is too time consuming to do the manual contouring for all the patients due to the fact that the MPM has irregular rind shapes and a large extent in the thorax, for example, in this cohort the tumour shows over at least forty or fifty slices in the DWI images for most of the patients, so it is impossible to find a radiologist who is happy to do all the manual segmentations apart from their heavy clinical works or to apply repeated measures. Furthermore, although the operator is not a trained radiologist, she has gained massive knowledge and experience in the area of MPM imaging and was well trained in contouring of MPM, thus it was the sub-optimal option. We admit this is the fundamental limitation in our study and needs to be investigated in the future study. For (c), even though the operator was not blind to the semi-automatic segmentations, the time interval between the semi-automatic segmentations and the manual segmentation is more than two years for all the patients, which was long

enough that we could consider them as independent measurements [Mark Beresford, JMRI, 2006].

Secondly, both semi-automatic methods require the initial seeds defined by the user, but this chapter did not investigate how these seeds affect the segmentation outcome and how to achieve good segmentation outcomes with seeds on a small number of image slices. Currently, it is still time consuming of drawing seeds to be applied in clinical studies. One possible future work can explore the influence of initial seeds on the segmentation outcome, and investigate how many slices with initial seeds are sufficient to produce a full volume segmentation.

Thirdly, the repeatability analysis has only been applied on one 2D images by the same observer while it lacks the repeatability analysis on 3D images with various observers , which should be tested in the future work. Lastly, this study did not correct the partial volume effect. Generally, the partial volume effect is quite small for most segmentations, but as the MPM disease is rind-like and has a large extent in the thorax, there may be more partial volume voxels present than in most segmentation problems (e.g. for segmenting round-like tissues, such as prostate, or liver tumour).

5.7 Chapter Summary

The two semi-automatic segmentation, GrowCut and Random walk, have been successfully applied on the diffusion-weighted image of MPM patients to estimate the MPM disease burden. The ten clinical cases showed both methods can achieve good performances and accuracies compared with the reference disease volumes. In the next Chapter, automatic classification methods will be investigated to classify the solid tumour from the pleural effusion based their different properties.

6 Tumour classification in malignant pleural mesothelioma

6.1 Introduction

In MPM patients, the presence of pleural effusion is common [139] and unilateral exudative pleural effusions can be extracted by pleural aspiration, therefore, the solid tumour in MPM is the key factor for tumour progression and response of anti-tumour treatments, so it is important to separate the solid mesothelioma tumour from the pleural effusion within the whole MPM disease which can be acquired by image segmentation (Chapter 5).

Diffusion weighted MRI allows quantification of the Apparent Diffusion Coefficient (ADC), which is a direct measure of the local rate of diffusion within tissues at each voxel location within the image (see Chapter 3 for full information). The ADC value quantified from DWI has been shown to reflect tissue cellularity. There is great need to conduct clinical trials that explore the role of tumour classification from the derived ADC measurements as predictive, prognostic and response biomarkers for MPM. A hypothesis of this thesis is that ADC values provide a robust, automatic methodology for discriminating between solid tumour and pleural effusion in MPM, thus providing quantification of the heterogeneous nature of the cancer. Tools for evaluation of these metrics do not currently exist in the clinic, but if found to be of clinical value, could have considerable impact for the management of patients with MPM.

In previous studies using diffusion-weighted imaging, solid tumour in malignant pleural mesothelioma or pleural effusions as analysed by manually drawing round-shaped or free-hand regions-of-interests (ROIs) within the solid tumours or pleural effusions on multiple image slices [2; 81; 85]. As only disease from a few slices instead of the whole volume is taken into account, evaluation depends on the clinical experience of the radiologist and it has lower inter- and intra- observer agreements and worse repeatability in ADC values [140]. Drawing the whole tumour volume manually has higher repeatability but is too time- and labour-consuming [140], hindering its application in daily clinical practice. Therefore, there is an urgent need for easily applied approaches to get an accurate estimate of the volume of solid

tumour. Given the MPM disease, including solid tumour and pleural effusion, has already been segmented in Chapter 5, the purpose of this chapter is to investigate methodologies to classify solid tumour from pleural effusion, and demonstrate the feasibility on example clinical dataset.

In Section 6.2, a classic threshold method will be used on ADC maps (fitted from weighted-least square and least squire algorithms) of the segmented disease volume, to automatically classify solid tumour and pleural effusions. The repeatability of this method will also be tested. In Section 6.3, a novel automatic clustering method, Gaussian Mixture model, will be investigated to classify the solid tumour within the whole disease volume from the pleural effusion based on diffusion and R2 properties. Some clinical results will be illustrated.

6.2 Global threshold using ADC map estimated from weighted-least square fitting

6.2.1 Introduction

Water diffusion in tissues has been shown to be inversely related to tissue cellularity and the integrity of cell membranes [20; 21; 23], which could be detected by DWI as the mechanism of DWI contrast is based on the differences in the mobility of water between tissues. ADC calculated from different b-value DWI images quantitatively show the degree of water mobility in tissues [2]. In malignancy, the tumour cell density is normally higher than normal tissue or plural effusions, so there is a greater barrier to the movement of extracellular water molecules (restricted water diffusion) in mesothelioma tumour. Due to this reason, it usually has lower ADC compared with areas with free water (e.g. pleural effusion) or normal tissues [141]. Thus, it is possible to classify solid cellular disease from the pleural effusions by evaluating the ADC values. Gill et al. [2] evaluated the ADC values of three histological subtypes of MPM in 50 patients with diffusion-weighted 3T MRI. The mean ADC values of MPM were calculated by a single blinded observer drawing three circular region-of-interests placed in the centre of the tumour tissue on b-750 DWI images. The mean ADC values for epithelioid, biphasic and sarcomatoid were $(1.31 \pm 0.15)*10^{-3}$, $(1.01 \pm 0.11)*10^{-3}$ and $(0.99 \pm 0.07)*10^{-3}$ mm^2/s, respectively. The ADC range of the MPM in this study is between 0.88 $*10^{-3}$ mm^2/s and 1.62 $*10^{-3}$ mm^2/s. Coolen et al. [81] also calculated the mean ADC of the lesions from the manually drawn ROIs on the high b-value DWI images in the cohort of 12 mesothelioma patients. The mean ADC of malignant pleural disease (MPD) was $(1.40 \pm 0.33)*10^{-3}$ mm^2/s (range: 0.8 – 2.0, $*10^{-3}$ mm^2/s) and cases where the mean ADC was between 1.52 and 2.00 $*10^{-3}$ mm^2/s may have a higher chance being wrongly diagnosis. The ADC values of two types of pleural effusion have been investigated by Inan et al. showing that exudative effusion has a significant lower ADC than transudative effusion: the mean ADC

values for the exudative and transudative effusions were 3.3±0.7 and 3.7±0.3 (× $10^{-3}mm^2/s$) respectively [85].

Studies in MPM suggest that the ADC may serve as a surrogate imaging biomarker to differentiate solid tumour and pleural effusions. To the knowledge of the author, a global threshold of ADC estimated from the weighted-least-square (wls) model or least-square model (ls) has not been previously used to classify solid tumour and pleural effusion and there is no published data investigating the ADC of pleural effusion and solid tumour in a patient cohort. In this study, a global ADC threshold ($2*10^{-3}$ mm^2/s) has been applied to whole MPM disease ADC metrics acquired from the semi-automatic segmentation (described in the Chapter 5) to classify solid tumour and pleural effusion.

There are two aims of this study,
(i) to evaluate if there is any significant difference between the results (tumour volume and apparent diffusion coefficient metrics) by using the two fitting models (wls vs. ls);
(ii) to evaluate the repeatability of tumour volume and apparent diffusion coefficient metrics using a combination of 3D semi-automatic segmentation and global thresholding of ADC in malignant pleural mesothelioma.

6.2.2 Method and materials

Patient population

This single centre, non-randomised imaging study has been approved by the institutional Research and Ethics committee. Eight patients with histopathologically proven MPM were enrolled in the prospective clinical trial between September 2015 and August 2017. The written informed consent from every patient was acquired before starting the study and patient information was anonymised before analysis.

Table 6.1:The patient cohort in this study

Patients	8

Male	6
Female	2
Age (mean (range))(Years)	68.7 (62 -77)
Male	70.1 (62-77)
Female	63.5 (63-64)
Disease Site	
Left lung	1
Right lung	7
Two baselines scan time intervals	1 hour – 7 days

Imaging protocol

All patients underwent DWI scans twice (interval between 1 hour and 7 days) before commencement of treatment. DWI images were acquired by using single-spin echo EPI on a 1.5T scanner (MAGNETOM Avanto, Siemens Healthcare, Erlangen, Germany) with two body-array surface receiver coils and a spine matrix. Two imaging volumes were used to cover the whole chest with 30 axial slices per volume. All the DWI images were acquired under free breathing; The overall acquisition time was 12 min.

Table 6.2: the parameters in the DWI protocol in this study

Parameter	**Value**
Sequence	Single-shot EPI
Coil	Body array coil
Breathing	Free breathing
Fat-suppression technique	SPAIR
Slice orientation	Axial
Phase-encode direction	Antero-posterior
Diffusion gradient scheme	Single spin echo
Diffusion-encoding scheme	Orthogonal
b-value (s/mm^2)	100/500/800

Parallel imaging	GRAPPA = 2
Ref. line	30
Repetition time (ms)	8100
Echo time (ms)	82
Number of signal averages (NSA)	4 (Not averaged)
Slice thickness (mm)	5
Gap slice (mm)	0
Number of slices per volume	30
pixel size (mm × mm)	3 × 3
Field of view	380 × 273
Acquired Matrix	128 × 92
Readout bandwidth (Hz/pixel)	1860
Echo-train length	1
partial Fourier factor	6/8

ADC fitting

When using a spin-echo echo-planar imaging (SE-EPI) sequence, the signal intensity for a given voxel in the DWI image is modelled as a mono-exponential function of b-value by fitting to the equation:

$$S(b) = S_0 \exp(-b \times ADC)$$

The S_0 and ADC maps were estimated from the acquired DWI images with two models: the weighted-least-square fitting and non-weighted least square fitting.

The ADC_{wls} maps were calculated by fitting weighted square to the 36 data sets (assuming isotropic diffusions at three diffusion gradient directions in the four repeated scans) for three b-values.

The ADC_{ls} maps were estimated by fitting Least square to the mean DWI images which were obtained by averaging the 12 data sets (four repeated series and three diffusion directions) at each b-value;

The values of S_0 and ADC were constrained to be positive values in the fitting procedure and all ADC maps were created using the in-house developed plug-in based on OsiriX DICOM reviewer (Pixmeo, Geneva, Switzerland).

Image analysis

1. The ADC_{wls} maps were calculated by fitting weighted square to the 36 data sets (assuming isotropic diffusions at three diffusion gradient directions in the four repeated scans) for three b-values while the ADC_{ls} maps were estimated by fitting Least square to the mean DWI images which were obtained by averaging the 12 data sets (four repeated series and three diffusion directions) at each b-value;

2. The total disease including both solid tumour and pleural effusions was segmented by using a 3D semi-automatic tool described in Chapter 5 with back- and fore-ground seeds drawn on the normal tissue and tumour tissue respectively on the mean b-value 100 s/mm^2 images. b100 s/mm^2 images were chosen as both solid tumour and pleural effusions had the highest signal intensities whilst maintaining good disease/background contrast among all DW images.

3. Segmented ROIs were then transferred to calculated mean ADC maps. Solid tumours and pleural effusions were classified below and above an ADC threshold of 2000*10^{-6}mm^2/s respectively within the whole tumour volume for each patient. A threshold ADC of 2000 is chosen is based on the above-mentioned literature.

Figure 6.1 illustrates the workflow of this study.

4. The repeatability of parameters (mean/ median ADC, and tumour volume) of the whole tumour and solid component in the two baseline measurements was evaluated

by using the Bland-Altman method [142]. The median ADC values from all pixels in the tumour volumes were used to reduce the sensitivity to outliers.

The Coefficient of Variation (CV) [143]of the log-transformed data (ADC/volumes) was used to measure the repeatability of the parameters:

$$CV = 100\% \times \sqrt{\exp\left(\left(\sum d^2\right)/2N\right) - 1}$$

where d is the difference of the log-transformed paired baseline measurements and N is the number of patients.

6.2.3 Results

In the two pre-treatment baseline scans of one example MPM patient, segmented whole tumour regions (blue region) are shown on the low b-value diffusion-weighted images while the solid tumours and pleural effusions classified by a global ADC threshold value are shown in red and green respectively on the ADC maps (Figure 6.2). It is shown that segmented whole tumour regions (Blue areas) at the axial slice showed a good visual match with both the low b-value diffusion-weighted images and the ADC maps in the repeated pre-treatment scans. The classified solid tumours and the pleural effusion regions are highly reproducible between the two pre-treatment baseline scans. There is little visual difference between the ADC_{ls} and ADC_{wls} maps.

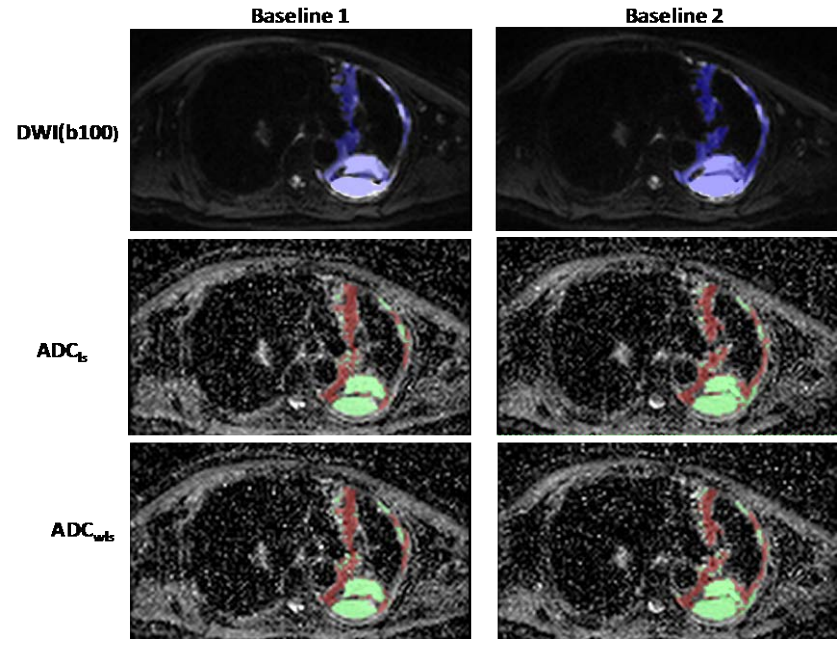

Figure 6.2: The two columns stand for the images from two pre-treatment baseline scans. Segmented whole tumour regions are shown in blue on the low b-value diffusion-weighted images.

The solid tumours and pleural effusions classified by a global threshold value are shown red and green respectively on the ADC maps. ADC_{ls}: ADC maps from the least-square fitting; ADC_{wls}: ADC maps from the weighted least squared fitting).

Figure 6.3 shows the bar plots of the paired baseline volume of solid tumour and pleural effusion for each patient by fitting to (A.) the least square and (B.) the weighted-least-square models. The total length of each bar represents the volume of the whole disease including solid tumour and effusion for one patient.

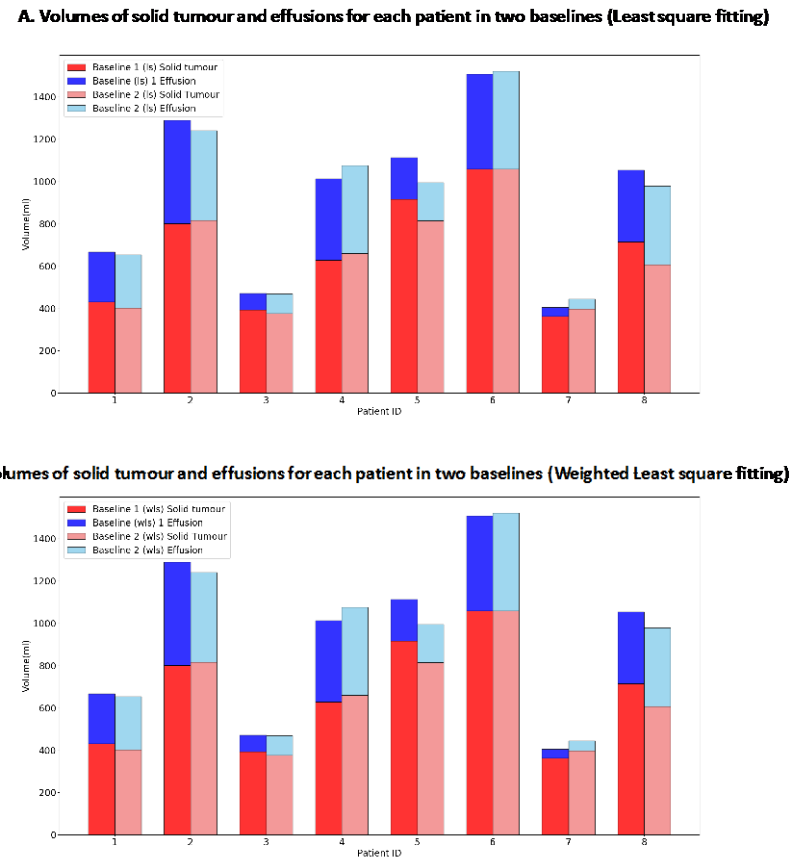

Figure 6.3: Bar plots of the paired baseline volumes of solid tumour and pleural effusion for each patient by fitting to (A.) the least square and (B.) the weighted-least-square models.

The height of each bar represents the volume of disease (solid tumour plus effusion), and the colour subdivision represents different components: red/pink stands for solid tumour and blue/light blue stands for effusion components.

Figure 6.4 shows the bar plots of (A.) mean and (B.) median ADC values of solid tumour for each patient by fitting to the least square and the weighted-least-square models in the paired baseline. In the bar plots both the mean ADC and the median ADC of the solid tumour from the two fitting models in the two baseline scans show similar values for each patient.

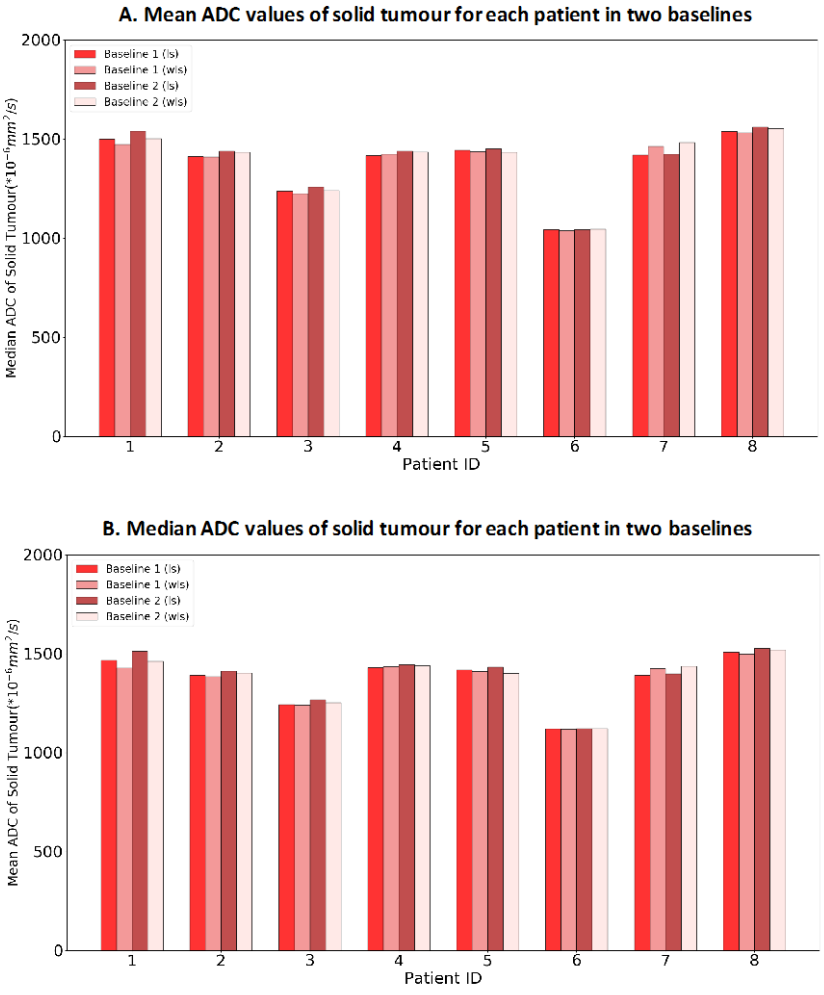

Figure 6.4: Bar plots of the paired baseline (A.) mean and (B.) median ADC values of solid tumour for each patient by fitting to the least square and the weighted-least-square models.

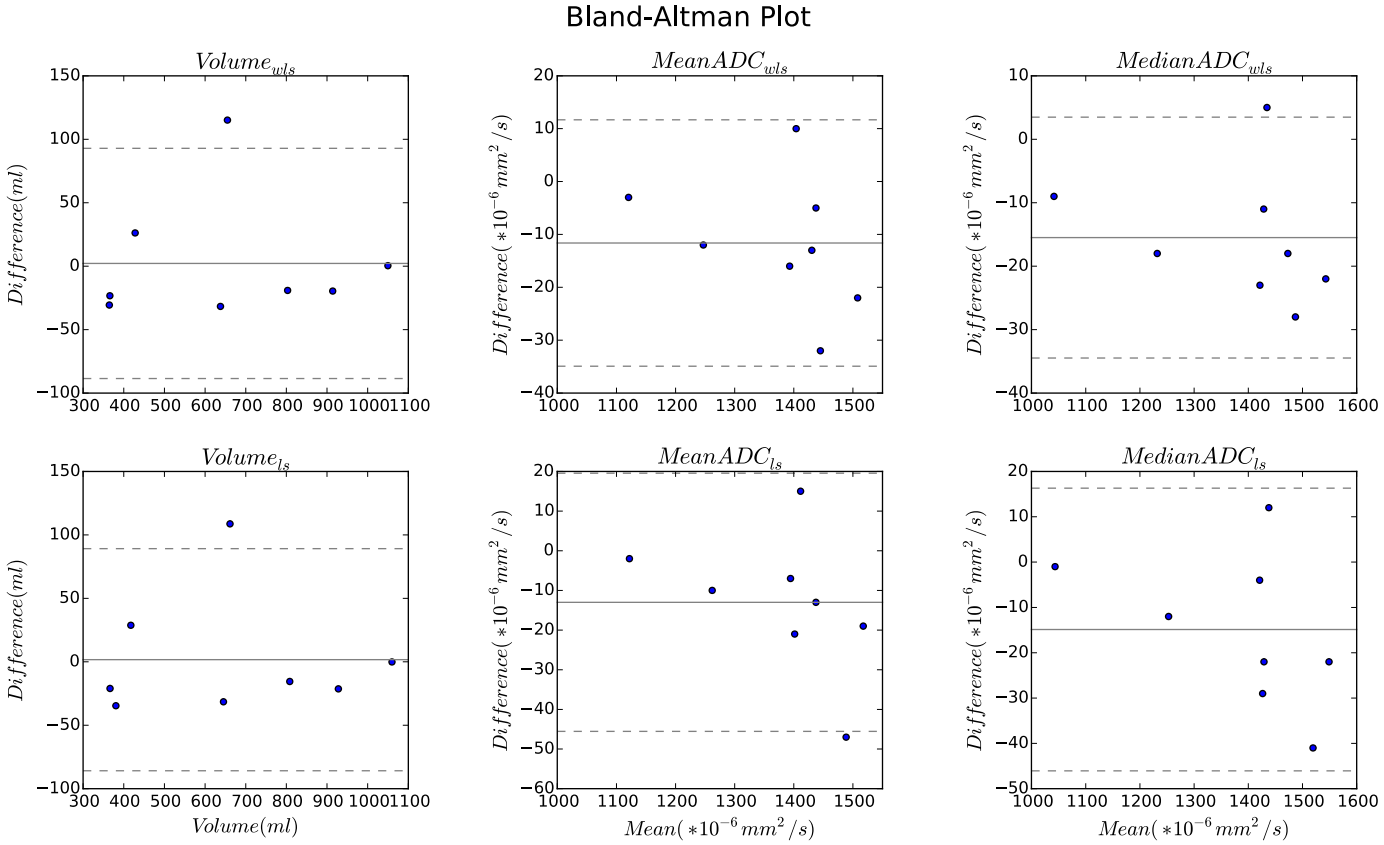
Bland-Altman Plot
$Volume_{wls}$
$MeanADC_{wls}$
$MedianADC_{wls}$
$Volume_{ls}$
$MeanADC_{ls}$
$MedianADC_{ls}$
$Difference(ml)$
$Difference(*10^{-6}mm^2/s)$
$Volume(ml)$
$Mean(*10^{-6}mm^2/s)$

Figure 6.5: The Bland-Altman plots derived from the (1st column) volume, (2nd column) the median ADC and (3rd column) the mean ADC of the solid tumour in two repeated baseline scans. The first-row plots are derived from ADC fitting by the weighted-least-square while the second row from the least-square.
Horizontal slid line in the plots represents the mean difference and the two dash lines are the 95% limits of agreement of the difference.

The average baseline values of the volume and ADC (median/mean) for the solid tumour are summarized in **Table 6.3**. The mean volume of the solid tumour was 612 ml (least-square fitting) and 606 ml (weighted-least-square fitting). With regard to ADC, the mean ADC values of the solid tumour of the eight patients are around $1370*10^{-6}mm^2/s$ for both least-square and weighted-least-square fittings.

Table 6.3: the average baseline volume and ADC (median, mean) values for the whole disease, solid tumour and the effusion.

	Average baseline value					
	Whole Disease		Solid tumour		Effusion	
	LS	WLS	LS	WLS	LS	WLS
Volume (ml)	856	856	612	606	219	230
Median ADC ($*10^{-6}mm^2/s$)	1604	1615	1376	1373	2426	2433
Mean ADC ($*10^{-6}mm^2/s$)	1690	1699	1374	1368	2490	2507

In **Table 6.4** the paired t-tests[22] showed no systematic differences between the two pre-treatment baseline volume of the MPM solid tumour from least-square and weighted least fitting methods ($p > 0.05$). There is bias for the median ADC of solid tumour from both fitting models and for mean ADC values acquired from the weighted least square model.

[22] The normality test (Shapiro-Wilk test) was applied to all the parameters before applying the t-test, and the results of Shapiro-Wilk test are

- volume calculated from WLS (W = 0.85785, p=0.1143),
- median ADC calculated from WLS (W= 0.88627, p=0.216),
- mean ADC calculated from WLS (W=97831, p=0.954),
- volume calculated from LS (W = 0.88545, p=0.212),
- mean ADC calculated from LS (W= 0.95481, p=0.7594),
- median ADC calculated from LS (W=0.98518, p= 0.9839).

It shows that the three parameters (volume, median ADC, mean ADC) calculated from either LS or WLS are all normally distributed, so t-test is able to be applied then.

Table 6.4: the t-test results of the repeatability study. Green numbers mean the p values of the t-test are larger than 0.05 while red means p-value is smaller than 0.05 (All of the values have passed the normality test before applying the t-test).

	Solid tumour	
	LS	WLS
Volume	0.98	0.98
Median ADC	0.03	0.003
Mean ADC	0.07	0.03

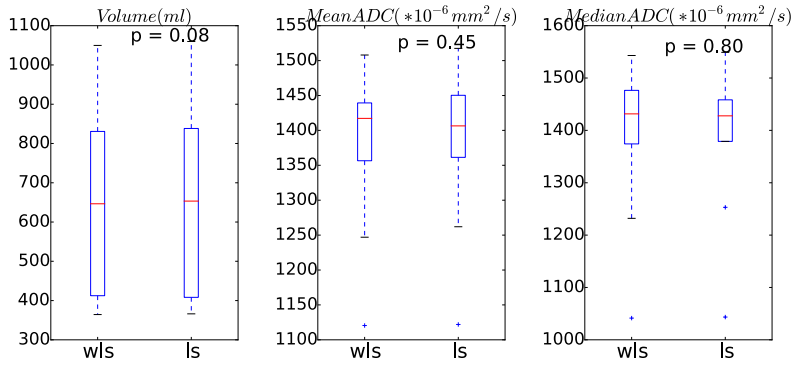

Figure 6.6: Box plots of the mean values of volume, median ADC, and mean ADC of the solid tumour in the two baselines acquired from two methods (wls, ls) in all patients.

CVs of ADC (mean and median) and tumour volumes and their 95% confidence intervals (CIs) are illustrated in **Table 6.5**. The biggest CV for volume, mean ADC and median ADC calculated from two pre-treatment measurements are 7.7%, 1.8% and 2.0%, respectively and this table indicates a very good repeatability of this study. In particular, the ADC measures feature smaller CVs than the volume. The median

ADC of the solid tumour fitted from the weighted-least-square model has the lowest CV of 0.5 among all the parameters.

Table 6.5: Coefficient of variations of the tumour volume and ADC and their 95% confidence interval.

	Coefficient variation (%, with 95 % CI)					
	Whole Disease		**Solid tumour**		**Effusion**	
	LS	WLS	LS	WLS	LS	WLS
Volume	**4.1** (2.8, 7.9)	**4.1** (2.8, 7.9)	**5.4** (3.7, 10.4)	**5.6** (3.8, 10.7)	**7.7** (5.2, 14.7)	**7.7** (5.2, 14.9)
Median ADC	**1.7** (1.1, 3.2)	**1.8** (1.2, 3.5)	**0.8** (0.5, 1.6)	**0.5** (0.3, 1.0)	**1.6** (1.1, 3.0)	**1.4** (0.9, 2.6)
Mean ADC	**1.9** (1.3, 3.7)	**2.0** (1.3, 3.8)	**1.0** (0.7, 2.0)	**0.6** (0.4, 1.3)	**1.3** (0.9, 2.5)	**1.3** (0.9, 2.6)

Table 6.6: The individual limits of agreement (LoA) for solid tumour

	Individual Limits of Agreements (LoA) of Solid tumour (%)	
	LS	WLS
Volume	(-13.9, 16.2)	(-14.3, 16.7)
Median ADC	(-1.2, 3.3)	(-0.3, 2.5)
Mean ADC	(-2.8, 2.9)	(-0.9, 2.6)

Table 6.6 shows the individual limits of agreement (LoA) of solid tumour in volume, median and mean ADC.

6.2.4 Discussion

In this study, a novel method that combines 3D semi-automatic segmentation (GrowCut) and global thresholding of ADC estimated from two fitting models has been investigated on clinical malignant pleural mesothelioma patients and the

repeatability of tumour volume and ADC parameters acquired have been evaluated in the two pre-treatment scans.

In our study, the mean ADC (from both least-square and weighted-least-square fittings) of the solid tumour in this repeatability study is around $1.37*10^{-3}mm^2/s$, which corroborates well with the values from the published studies[140]. Gill et al. [2] calculated that the mean ADC values for epithelioid, biphasic and sarcomatoid were $(1.31 \pm 0.15) *10^{-3}$, $(1.01 \pm 0.11)*10^{-3}$ and $(0.99 \pm 0.07)*10^{-3}$ mm^2/s, respectively. Coolen et al. [81] also calculated the mean ADC of malignant pleural disease (MPD) was $(1.40 \pm 0.33)*10^{-3}$ mm^2/s. It is notable that mesothelioma volumes in this two studies were acquired by manually drawing circles/ROIs on several slices of the high b-value DWI images, which will lead to a smaller ADC estimate of the solid tumour than that from volumetric estimate [140].

In terms of tumour burden and ADC, the repeatability of the solid tumour and whole tumour is good. The worst case (top of range at 95% confidence interval) of the CV is only 14.9%. The whole procedure, including data acquisition, segmentation and ADC thresholding, has very low CoV, which indicates very good repeatability for imaging thoracic area which involves motion effect from breathing. Comparing to the repeatability study in whole body DWI, the CoV of mean/ median ADC [144] is 2-3 times higher than our results. Low CVs (0.5 to 7.7%) and 95% LoA mean that our methodology will be more sensitive to treatment effects or disease heterogeneity. This method offers a clinical tool for radiologists to evaluate the tumour burden of MPM in a fast and highly repeatable way.

When comparing the results from the two fitting methods, there is very small difference between the results from the Weighted-least-square fitting and least-square fitting, although weighed-least-square fitting may result in a smaller standard deviation of the tumour ADC, and may provide us a higher degree of confidence of the ADC, especially at the edge pixels of the tumour.

In this study, we chose ADC $=2000*10^{-6}mm^2/s$ as the threshold to include definite solid tumour and probable semi-solid disease states. However, this may cause a bias of the solid tumour ADC value and may also cause heavier partial volume effect,

specially for our case where solid tumour and pleural effusion have very different ADC values. Different threshold values should be tested in future studies.

There are several limitations of this pilot study: firstly, this study has a small sample size and a larger patient cohort will be investigated in future studies. Secondly, the repeatability study is a single observer study, and should be tested by multiple observers. Besides, the observer in the study was not blind to the two baseline segmentation results and may also affect the final results. Thirdly, the volumes of the solid tumour and pleural effusion were not validated as it is not possible to obtain pathological validation. At last, this study did not consider the partial volume effect.

In conclusion, there is no significant difference between the results from the two fitting models. The classification of solid tumour by using a 3D semi-automatic segmentation method and a global ADC threshold shows excellent repeatability of mean and median ADC estimates and tumour volume in the diffusion-weighted imaging using both least square and weighted least square fitting.

Some findings in this section were from the publication: Cheng, L., Blackledge, M.D., Collins, D.J., Tunariu, N., Orton, M.R., Leach, M.O. and Koh, D.M., Assessment off Repeatability of Disease Burden and ADC estimates in Malignant Pleural Mesothelioma using Diffusion Weighted Imaging. ***ISMRM (Hawaii), 2017***

6.3 Gaussian Mixture modelling using ADC and R2

6.3.1 Introduction

In **Chapter 4** T_2-adjusted Computed Diffusion-Weighted MRI (T_2-cDWI) has been shown to provide improved contrast between disease and background tissues, and facilitates total disease segmentation [117]. It also provides the additional R_2 map (or T_2) for more information. Gaussian distribution is a widely used continuous probabilistic representation, and it provides a useful way to estimate uncertainty of the data. It is easy to compute and interpret. Because of both practical and theoretical benefits, Gaussian mixture modelling of voxelwise estimates of within-tumour ADC and transverse relaxation rate (R_2) may offer a viable method to characterise disease heterogeneity. The purposes of this study were to investigate this novel methodology to assess disease heterogeneity in mesothelioma, and demonstrate its utility on some clinical dataset.

6.3.2 Theory of Gaussian mixture model (GMM) in One dimension

The Gaussian probability density function p(x) of given one dimensional data x, is given by

$$p(x) = \frac{1}{\sqrt{2\pi}\sigma} exp\left\{-\frac{(x-\mu)^2}{2\sigma^2}\right\}$$

Where μ is the mean, σ^2 is variance, σ is the standard deviation.

For given data $\mathbf{x}_i$, i = 1⋯ N, which are samples from a probability distribution p(x), the basic assumption of GMM is that p(x) is modelled by a sum of K Gaussians.

$$p(x) = \sum_{k=1}^{K} w_k \, p_k(\boldsymbol{x}|\theta_k)$$

where w_n is the weight factor for the *n*th component where $0 < w_k < 1$ and $\sum_{k=1}^{K} w_k = 1$. $p_k(\boldsymbol{x}|\theta_k)$ are the GMM components and $p_k(\boldsymbol{x}|\theta_k)$ in one dimension are given by

$$p_k(x_i|\theta_k) = \frac{1}{\sqrt{2\pi\sigma^2}} e^{-\frac{(x_i-\mu_k)^2}{2\sigma_k^2}}$$

$$\theta_k = (\mu_k, \sigma_k)$$

where μ_k is the mean value of class k, σ^2 is the variance of class k.

Maximum Likelihood Estimation using the EM algorithm

Likelihood function is the probability of an observation given the model parameters and is the joint probability of all the data. Under the assumption of independent observations x_i, the joint likelihood function for θ can be written as,

$$L(\theta|x) = \prod_{i=1}^{N} p(x_i|\theta)$$

i indicates one particular observation x_i among multiple observations of x.

The likelihood function of a Gaussian mixture model with K components is shown as following:

$$L(\theta|x) = \prod_{i=1}^{N} p(x_i|\theta) = \prod_{i=1}^{N} \sum_{k=1}^{K} \frac{w_k}{\sqrt{2\pi\sigma^2}} e^{-\frac{(x_i-\mu_k)^2}{2\sigma_k^2}}$$

where $\theta = \{\theta_n\}$ for n = 1,⋯, K and x= $\{x_i\}$ for i = 1,⋯, N, which corresponds to the probability to observe the given samples x_i if independent and identically distributed random variables are assumed.

The larger likelihood indicates the better model parameters fit to the data, to maximize the likelihood function of a mixture model, the Expectation-Maximum (EM) Likelihood Estimation algorithm [145] is widely used to estimate the parameters of the model especially when part of the data can be considered to be incomplete, or hidden. In a Gaussian mixture model with K components, $w_n, \mu_n \; and \; \sigma_n$ are the parameters to be determined.

$$\hat{\theta} = \arg \max \; L(\theta|x) = \arg max \prod_{i=1}^{N} p(x_i|\theta)$$

The logarithm of the likelihood function, log-likelihood, is often used instead of the likelihood function in the process of maximum likelihood estimation. The logarithm function is monotonically increasing, so the log-likelihood function achieves its maximum value at the same points as the likelihood function.

$$\arg\max_{w,\theta} L(\theta|x) = \arg\max_{w,\theta} \ln\{L(\theta|x)\}$$

Weight factors can be considered as prior probabilities for the classes while the posterior probability (Responsibility), p_{ik}, for each data point i, can be calculated from the Bayes rule:

$$p_{ik} = P(k|x_i) = \frac{p(k)p(x_i|k)}{p(x_i)} = \frac{w_k p_k(x_i|\theta_k)}{\sum_{m=1}^{K} w_m p_m(x_i|\theta_m)}$$

The Expectation-Maximization algorithm is an iterative optimisation method which is used to find the maximum of the likelihood of the GMM and estimate the GMM parameters, and it is illustrated in the following three steps:

Step 1: Initialization of the GMM parameter.
In the initialization of GMM, model parameters need to be assigned firstly. K-means clustering is a very common method for GMM initialization and to get some hard-labels on the data. In this proposed method, the mean values of the two classes will be manually chosen by the user based on the distribution of the data.

Step 2: Expectation step (E-step).
In the Expectation step (E-step), the probability of each data point belonging to every class will be calculated with the initial GMM parameters.

Step 3: Maximization step (M-step): Re-estimate the Component Parameters
With the calculated posterior probabilities (i.e. soft labels) from E-step, the GMM parameters will be re-estimated and updated (Weight factor, mean and variance of every class).

The E-step and M-step will be repeated until convergence.

6.3.3 Methods and materials:

Patients population

This single centre, non-randomised imaging study has been approved by the institutional Research and Ethics committee. Five patients with histopathologically proven MPM were enrolled in the prospective clinical trial between September 2015 and August 2017. The written informed consent from every patient have been acquired before starting the study and patient information was anonymised before analysis.

One example patient underwent two repeated baseline scans (four days apart) before commencement of treatment while two patients were scanned before, 4 weeks and 12 weeks after anti-tumour treatment.

MR image acquisition

In this study diffusion- and T2-weighted images were acquired using 1.5T Magnetom Avanto (MAGNETOM Siemens Healthcare, Erlangen, Germany) (Details of the sequences parameters are shown in **Section 4.3.2**). The overall acquisition time is about 30 min.

Image processing

1. Computed DWI images with b = 150 s/mm^2 and echo time 20 ms (in-house software [123]) are generated using T_2-cDWI descripted in **Chapter 4**. These parameters were chosen such that the two components of MPM had similar signal intensities whilst maintaining good disease/background contrast.

2. The total disease volume including solid tumour and pleural effusion was segmented using a semi-automatic tool (in-house plugin based on the GrowCut algorithm [131] descripted in Chapter 5) on T_2-cDWI (b=150, TE = 20) images.

3. ROIs were reviewed by a senior radiologist and then transferred to calculated ADC and R_2 maps, jointly estimated from the diffusion- and T_2-weighted data [146].

4. Two-dimensional scatter plots of ADC/R_2 voxel values were generated and a 2-

class Gaussian Mixture Model was applied to the global multivariate data, using the Expectation Maximization (EM) algorithm for parameter estimation [147].

5. Following estimation of these multi-modal probability distributions, deriving the posterior probability, P_{ij}, of a voxel i belonging to each class C_j, allowed construction of tissue classification maps and calculation of proportional disease volume of each class.

6. The volume (absolute and percentage) and the mean function parameters (ADC, R_2) of each class was calculated.

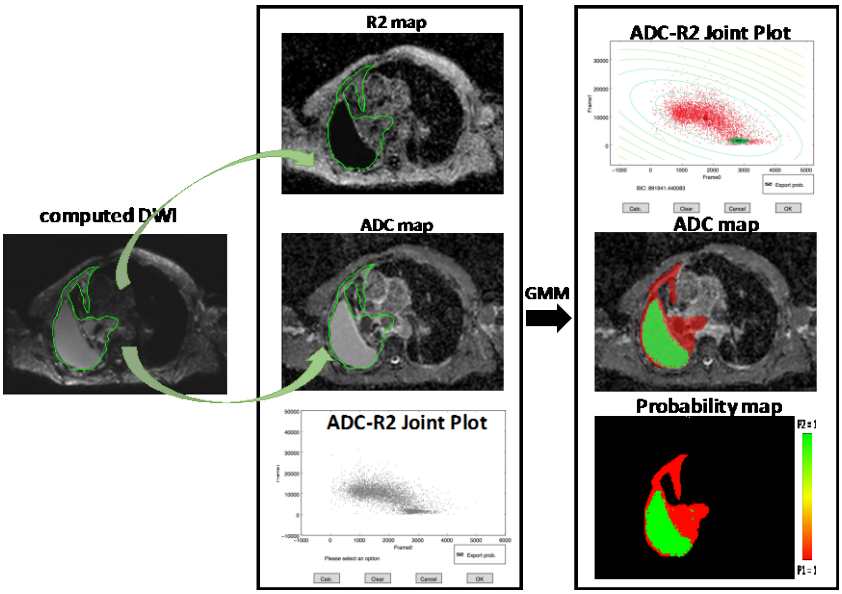

Figure 6.7: Illustration of the data processing. The left-hand image is the synthetic image at b of 150 s/mm^2 and TE of 20 ms with the green contour of MPM whole disease acquired by GrowCut segmentation; On the right-hand column, the red stands for the solid tumour and the green colour stands for pleural effusions.

6.3.4 Results

Patient 1:

Figure 6.8 has shown the repeated pre-treatment baseline scans (four days apart) for a 74-year-old male MPM patient. The regions of solid tumour and pleural effusion, shown in red and green respectively on the ADC and R_2 maps, are with similar shapes between the two baselines. Maps of the posterior probabilities of the two classes (C1: solid disease; C2: pleural effusion) are shown on a red-green colour scale: the red colour means the pixel has a probability100% belong to class C1, solid disease, while the green Class C2, pleural effusion. Yellow stands for the pixel has an equal probability (50%) belonging to each class. It has been seen that the two pre-treatment baseline data for the patient have very similar shapes of ADC/R_2 distribution on the joint histogram. The contour lines in the last columns shows that the joint ADC-R_2 data sets are both well fitted by GMM with two Gaussian distributions. (mean vectors shown on the figure). In addition, regions and their probability maps show a high correspondence between the two baseline studies. The percentage differences of ADC, R_2 and volume of the solid disease (class 1) in the two baselines are 3%, -5.3% and 4.2% respectively.

The proportional volumes of the two classes have < 6% difference in the two pre-treatment baseline scans (**Table 6.7**), suggesting a repeatable method.

Table 6.7: ADC and R_2 values for the cluster centres in Gaussian distributions and the absolute and percentage volumes for Patient 1 with repeated pre-treatment scans.

Patient 1				
	Baseline 1		Baseline 2	
Class	1	2	1	2
ADC ($*10^{-6}$ mm^2/s)	1782	3272	1840	3261
R2 (s^{-1})	11.3	3.2	10.7	3.0
Volume (ml)	898	390	936	306

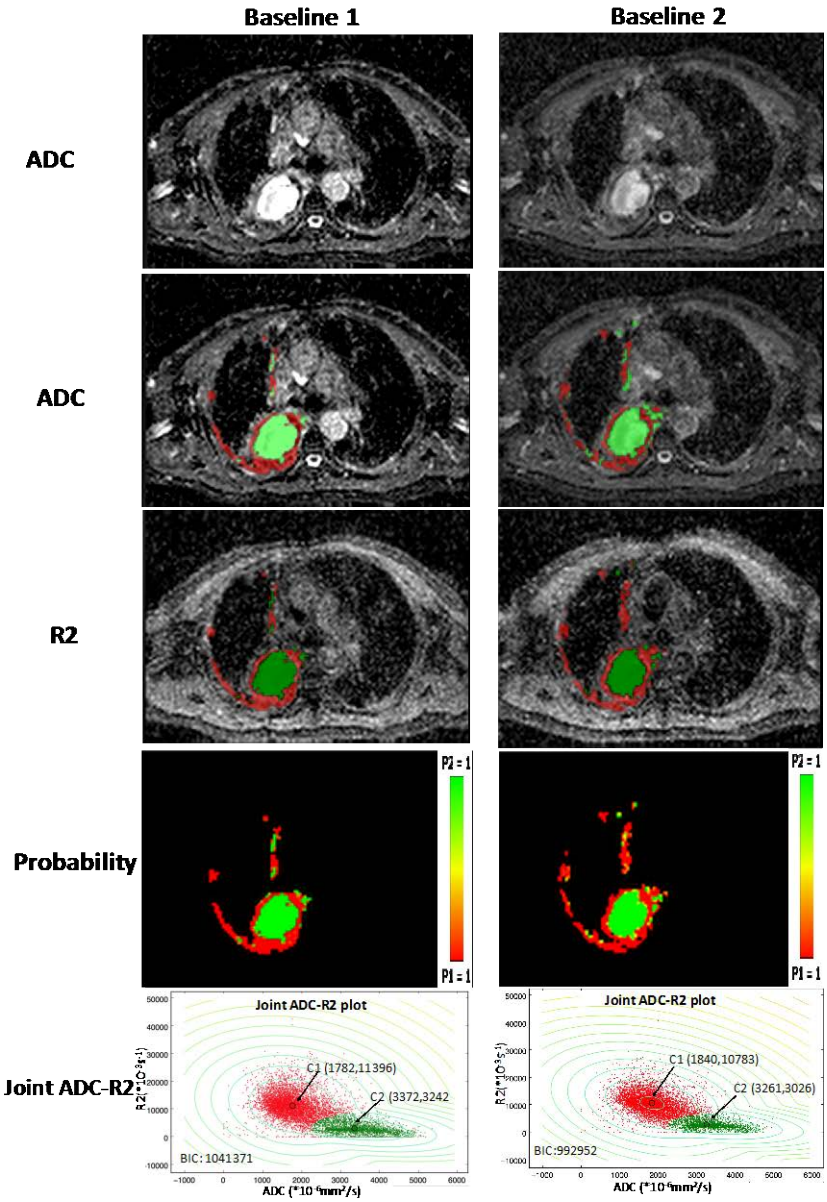

Figure 6.8: A 74-year-old male MPM patient with two pre-treatment scans (four days apart).

Rows are (Up to down) ADC maps; ADC maps with overlaid classes, R2 maps with overlaid classers: solid tumour (C1, Red); pleural effusion (C2, Green);

overlay colours represent the cluster with highest posterior probability for each voxel; scatter plots showing properties of the two clusters. The red colour means the pixel has a probability100% belong to class C1, solid disease, while the green Class C2, pleural effusion. Yellow stands for the pixel has an equal probability (50%) belonging to each class.

Patient 2:

When comparing the pre-treatment, and 4-week post-treatment in **Figure 6.9**, scatters have very similar distributions on the joint ADC-R_2 plots. The volume and function parameters of two classes have a very small difference between two scans, indicating this patient has no treatment response at the early stage (4 weeks).

When comparing between the pre-treatment and 12 weeks post-treatment, there is an obvious difference in the tumour shape showing on the ADC maps (**Figure 6.9**): both the solid tumour and the pleural effusion have decreased volume after 12 weeks treatment (**Table 6.8**).

On the joint ADC-R_2 scatter plot, the joint parameter distribution becomes less dispersion, with less scatter observed on the left corner of the joint scatter plot. There was a visible change of the centre of solid disease (cluster 1) to right, with 18% increment in the mean ADC from 2018 to 2381 $*10^{-6}$ s/mm^{-2} (**Figure 6.9** and **Table 6.8**). These changes in the tumour volume and the ADC parameters of the patient at 12 weeks post-treatment may indicate an effective treatment response at a later stage. In terms of R2 orT2, both of the two classes have very small change between the two scans. (**Figure 6.9**).

Table 6.8: The changes in volume and functional information (ADC, R2) of the two classes (solid tumour and pleural effusion) of Patient 2 before and after treatment.

Patient 2						
	Pre-treatment		4 weeks Post-treatment		12 weeks Post-treatment	
Class	1	2	1	2	1	2
ADC ($*10^{-6}$ mm^2/s)	**2018**	3600	**2036**	3576	**2381**	4075
R2 (s^{-1})	13.0	1.5	12.5	1.3	11.9	1.4
Volume (ml)	774	684	817	866	330	491
% Volume	53	47	49	51	40	60

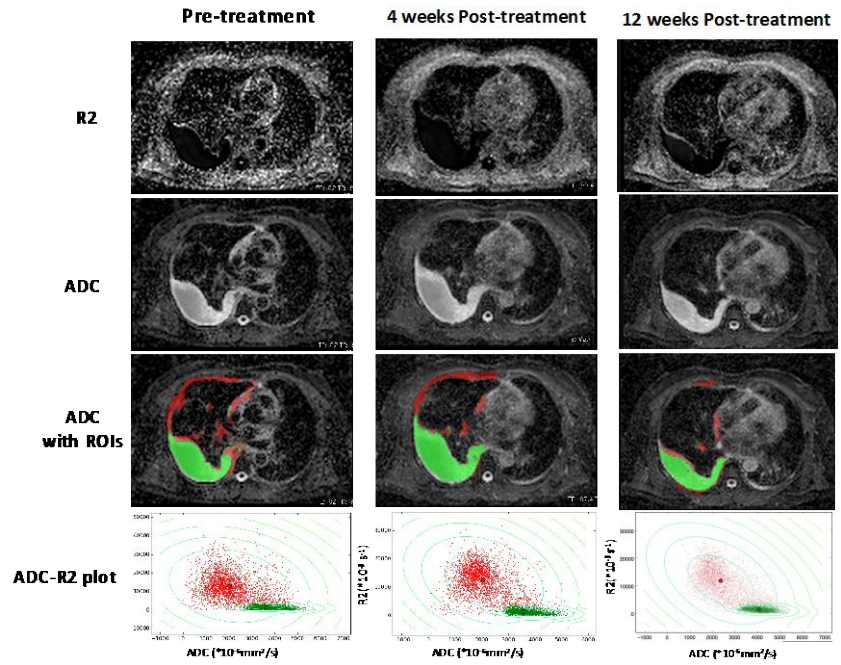

Figure 6.9: Example Patient 4 with pre-treatment, 4-week and 12-week post-treatment scans.

Rows (Up to down): R2 maps; ADC maps; ADC maps with overlaid classes: solid tumour (C1, Red); pleural effusion (C2, Green); scatter plots showing properties of the two clusters (colours represent maximum a-posteriori classification for each voxel).

Patient 3:

Figure 6.10 shows that the ADC-R_2 joint distribution after treatment changed with increased dispersion, and increasing scatters are observed on the left corner of the joint histogram, which represents more pixels in class 1 were associated with lower ADC and lower R2 after 4 weeks of the treatment. In addition, there was a visible shift of the centre of cluster 1 (solid tumour) to the lower left on ADC-R_2 plots in **Figure 6.10**, which means ADC decreased from 1538 to 1411 $*10^{-6}$ s/mm^{-2} while R_2 from to 13.6 to 12.3 s^{-1}(**Table 6.9**). After treatment, both the absolute and proportional volume of class 1 (solid disease) increased while the pleural effusion decreased (**Table 6.9**).

Table 6.9: The changes in volume and functional information (ADC, R2) of the two classes (solid tumour and pleural effusion) of Patient 3 before and after treatment.

	Patient 3			
	Pre-treatment		4 weeks Post-treatment	
Class	1	2	1	2
ADC ($*10^{-6}$ mm^2/s)	**1538**	1889	**1411**	1948
R2 (s^{-1})	**13.6**	10.7	**12.3**	10.5
Volume (ml)	381	481	494	317
% Volume	**44**	**56**	**61**	**39**

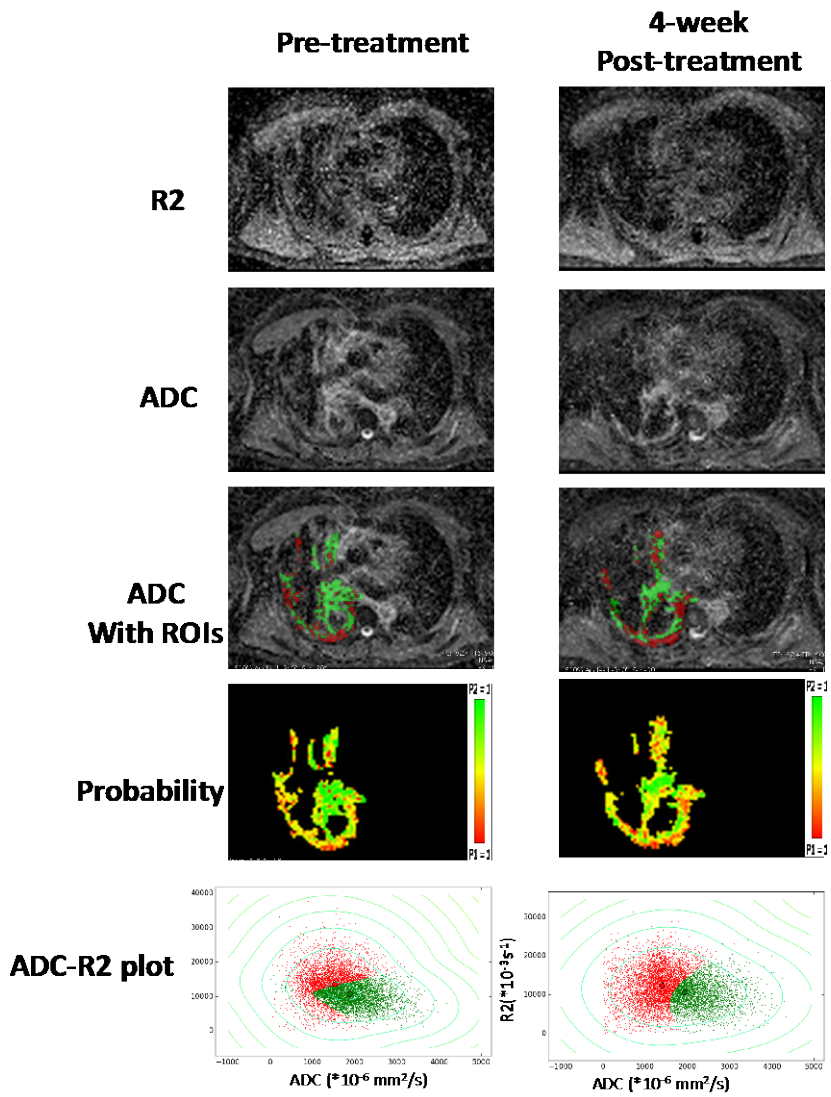

Figure 6.10: A 61-year-old female MPM patient with pre- and post-treatment scans 4 weeks apart.

Rows (Up to down): R2 maps; ADC maps; ADC maps with overlaid classes: solid tumour (C1, Red); pleural effusion (C2, Green); posterior class probability

map; scatter plots showing properties of the two clusters (colours represent maximum posterior classification for each voxel).

6.3.5 Discussion

In order to characterise the heterogeneity of MPM and achieve the classification of solid tumour, Gaussian mixture modelling using ADC and R_2, has been investigated and applied on three MPM clinical cases. This method can provide additional quantitative functional information for disease characterisation compared with using only a single parameter, especially the two functional maps, ADC and R2 maps, are inherently matched.

These example cases have demonstrated that it is possible to assess disease heterogeneity by using joint ADC/R2 modelling combined with a semi-automatic segmentation tool on T2-cDWI. This method may be used to observe changes in the mean ADC and R2 values after treatment within a disease volume for each tissue class independently and evaluate the heterogeneous treatment response.

Our hypothesis in this study is that there are two different components (solid tumour and pleural effusions), so GMM works well on the data, which has two non-overlapping components (Patient 2), and the GMM classification does not work well on data with only one class, or two overlapping classes due to noise or partial volume effect. This is one reason that GMM is not chosen in the clinical trial in Chapter 7.

There are several limitations of this pilot study: firstly, this study has a very small patient cohort and further investigation of the model should be performed in a larger clinical cohort. Secondly, the outcome of the study was not verified the reason is that it is not possible to obtain pathological validation.

The Gaussian mixture modelling methodology using ADC and R2 has been investigated to characterised heterogeneity for patients with malignant pleural

mesothelioma and can provide additional quantitative functional disease response characterisation compared with using only a single parameter.

Some findings in this section were from the publication: Cheng, L., Blackledge, M.D., Collins, D.J., Tunariu, N., Jerome, N.P., Orton, M.R., Morgan, V.A., Leach, M.O. and Koh, D.M., Characterisation of disease heterogeneity in malignant pleural mesothelioma using mixture modelling of ADC and R2. ***ISMRM (Singapore), 2016***

7 Treatment effect evaluation in malignant pleural mesothelioma using DWI

7.1 Introduction

Previous studies have shown that ADC reflects tissue cellularity [21] and increases in response to effective anti-tumour treatment. Chapter 6 has investigated that the DWI volumetric method combining GrowCut and the global ADC thresholding method could provide us two potential response biomarkers in a highly repeated way – the total solid tumour volume (TTV) and the median ADC of the segmented tumour volume. To our knowledge, no study has investigated if the changes in TTV and median ADC of malignant pleural mesothelioma derived from DWI have any relationship with response assessed by CT modified RECIST, or patient overall survival in patients treated with chemotherapy (carboplatin/cisplatin and pemetrexed). In this chapter, the DWI volumetric method (Section 6.2) will be applied to the clinical MPM patients. The **primary objective** of this chapter was to measure post-chemotherapy changes in the total solid tumour volume (TTV) and median ADC of patients with malignant mesothelioma. Changes were compared between two different patient cohorts, responding and non-responding patients, which were defined using CT modified RECIST. In addition, a number of **secondary objectives** were investigated:

1. To compare the pre-treatment TTV/median ADC values between responding and non-responding patients with post-treatment TTV or median ADC values.
2. To assess whether there is any relationship between the pre-treatment TTV/median ADC values (and changes in these parameters at 4 and 12 weeks) with overall survival.

7.2 Materials and methods

7.2.1 Study Design

DWI scans were performed before treatment, at 4 weeks post-treatment and 12 weeks post treatment (carboplatin/cisplatin and pemetrexed); CT scans were performed before treatment and 12 weeks post-treatment. Treatment response was defined using modified RECIST criteria, and DWI parameters (TTV and median ADC) were estimated where data was available.

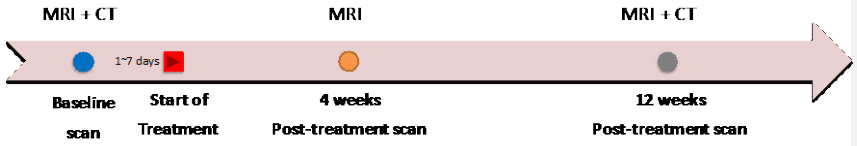

Figure 7.1: An illustration shows the timing of the mesothelioma study when the imaging and treatment were performed.

7.2.2 Patient Population

This prospective, single centre, non-randomised imaging study was approved by the institutional Research and Ethics committee. Patient eligibility criteria are shown in **Table 7.1**; 22 patients with histopathologically proven MPM were enrolled in the clinical trial between May 2015 and November 2017. Written informed consent from every patient was acquired before they were enrolled on the study, and patient information was anonymised before analysis.

Table 7.1: Patient Eligibility

Inclusion Criteria	Exclusion Criteria
▪ 18 years of age or older ▪ Histopathological proven malignant mesothelioma ▪ Previously treatment naïve suitable for 1st line standard chemotherapy ▪ Measurable disease by CT modified RECIST	▪ Contraindications to MR imaging (e.g. cardiac pacemaker, cochlear implant) ▪ Unable to tolerate MRI examination (e.g. claustrophobia)

In total, 22 patients were enrolled in the trial, and 4 patients withdrew consent after baseline measurement, providing 18 evaluable patients including 7 patients who had only two MRI scans (baseline + 4 weeks post-treatment). For the 18 evaluable patients, the median interval between the post- and baseline- CT scans was 9 weeks (the range: 5.9 ~ 12.3 weeks), while the median interval between 4-week-post-tresatment and baseline MRI scans was 4.2 weeks (range: 2.9 ~ 6.1 weeks). 11 patients completed the full protocol of three MRI scans (baseline scan, 4-week, and 12-week post-treatment scans) and the interval between 12-week-post-treatment and baseline MRI scans is 12.3 weeks (range: 9.6~15.1 weeks). Patient demographics are presented in Table 7.2.

Table 7.2: Patient demographics for this study

Patients	22
Male	19
Female	3
Age (years±standard deviation (range])	65.9 ± 6.5 (52 -78)
Male	66.6 ± 6.6 (52-78)
Female	60.5 ± 3.8 (57-64)
Disease Site	
Left lung	6
Right lung	16

7.2.3 Image acquisition

CT acquisition

CT scans according to standard of care were performed on a LightSpeed 16 CT scanner (GE Medical Systems) in the axial plane. The image size was 512 x 512 pixels, with available reformatted slice-thickness of 1mm, 1.25mm, 2mm, 2.5mm, or 5mm. Pixel spacing was between 0.68*0.68mm^2 and 0.88*0.88mm^2 for all patients.

MRI acquisition

All MRI scans were performed on a 1.5T MR scanner (Magnetom Avanto, Siemens Healthcare, Germany) with body array coils. All patients were imaged in the Head-first supine position. Anatomic MR imaging included the transverse T1- weighted 3D FLASH Breath-hold technique with fat selective prepulse (VIBE) (Breath-hold; TR/ TE 2.39/0.78 ms; slice thickness 5.0 mm; number of signals averaged 2; FoV read 380 mm; Pixel size, 1.5× 1.5 mm; Number of slices: 52), 3D coronal T2-weighted SPACE acquisitions (Free breathing with navigator; TE/TE 3500/100; slice thickness, 3.0 mm; number of signals averaged, 1.4 ; FoV read, 360 mm; pixel size, 1.8 × 1.9 mm; Number of slices: 60/64), coronal dynamic T2-weighted trufi sequence (TR/TE 3.02/1.51ms; Pixel size: 0.7×0.7 mm; Number of slices: 1). The full MR imaging protocol used in the trial is demonstrated in detail in the Appendix.

The diffusion-weighted sequence has been optimised to improve the image quality in imaging MPM and the parameters are shown in **Table 7.3**. Axial DW images were acquired with fat suppression and a free-breathing single shot spin-echo EPI sequence with auto-calibrating parallel imaging technique. The total time for DWI acquisition was 11 minutes.

Table 7.3: Parameters of the DWI sequence

Parameters	Values	Parameters	Values
Sequence	Single-shot EPI	**Coil**	Body array coil
Breathing	Free breathing	**Fat-suppression technique**	SPAIR
Slice orientation	Axial	**Phase-encode direction**	Antero-posterior
Diffusion gradient scheme	Single spin echo	**Diffusion-encoding scheme**	Orthogonal
b-value (s/mm^2)	100/500/800	**Parallel imaging**	GRAPPA = 2
Ref. line	30	**Repetition time (ms)**	8100
Echo time (ms)	82	**Number of signal averages (NSA)**	4 (separated)
Slice thickness (mm)	5	**Slice gap(mm)**	0
Number of slices per volume	30	**Pixel size (mm × mm)**	3 × 3
Field of view	380 × 273	**Acquired Matrix**	128 × 92
Readout bandwidth (Hz/pixel)	1860	**Echo-train length**	1
partial Fourier factor	6/8		

The free-breathing technique was chosen as most MPM patients suffer from thoracic pain and are unable to hold their breath so that breath-hold DWI acquisitions are too long to be uncomfortable and unfeasible. Navigator-controlled DWI, has not shown advantages over multiple averaged free breathing DWI in estimation of ADC in abdomen [148]. Multiple signal averages (N=4) were used to average the signal over physiological motion so as to reduce breathing artefacts and increase the image SNR and CNR.

Due to spatial non-linearities in the diffusion-encoding gradients [149], the extent of the imaging volume along the scanner (z axis) was limited to 25 cm to reduce bias in ADC estimates. However, mesothelioma usually extends over a large volume in the thorax, therefore, two imaging stations (30 slices per station, with each covering a range of 150 mm) were acquired sequentially at the isocentre of the scanner to cover the entire thoracic cavity and diaphragm and improve B0-field uniformity in each station.

b-values were chosen at 100, 500, 800 s/mm^2: a b-value of 100 s/mm^2 was chosen to reduce intravascular water perfusion effects, whilst maximum b-values of 800 to 1000 s/mm^2 are common in body applications [150], and a b-value of 800 s/mm^2 was chosen to reduce eddy current distortion. An extra intermediate b-value of 500 was included to ensure ADC estimates could still be obtained following a rise in ADC after treatment.

Diffusion gradients were applied sequentially in three orthogonal axes to generate three sets of DW images per b value, so the DWI image at each b-value would have 12 datasets (3 directions, 4 signal averages). Assuming isotropic diffusion within tumours, these data were used to optimize ADC fitting by using weighted least squire algorithm (Chapter 6) or be averaged for improving image signal-to-noise ratio for image segmentation (Chapter 5).

The Generalized Autocalibrating Partially Parallel Acquisition (GRAPPA) technique was used to reduce susceptibility-related distortions.

7.2.4 Image and data analysis

7.2.4.1 CT modified RECIST analysis

A radiologist with 5-year experience in CT performed modified RECIST measurements [40] before treatment and at 12-week after treatment. In each patient, six measurements were acquired in total, two at any particular level of the thorax at three different levels at least 1cm apart from each other (**Figure 7.2**). These measurements were then summated to produce the total tumour size. These

measurements were acquired at similar levels and positions in each patient at baseline and 12-week post-treatment CT studies.

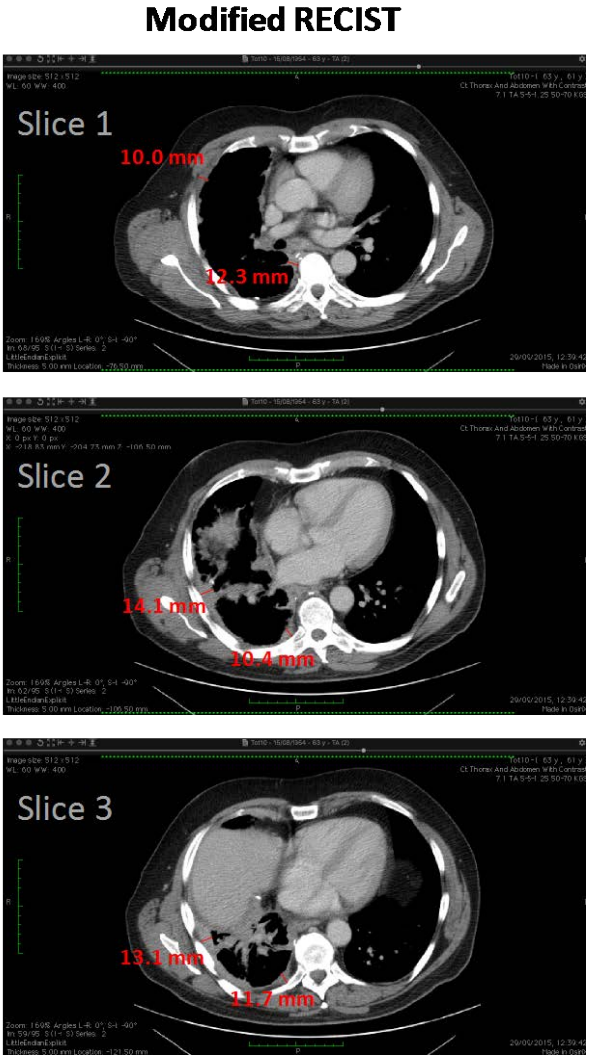

Figure 7.2: Tumour measured based on modified RECIST for a 61-year-old male patient at a baseline CT scan. The tumour was measured in two positions on three transverse images of the CT scan which are at least 10mm apart. The sum of the six measurements for this patient, 71.6 mm, is the total measurement for baseline CT scan.

The total tumour measurement was acquired on the baseline (B) and 12 weeks post-treatment CT scans (P), and the tumour changes between the two visits were calculated as

$$Difference = \frac{P - B}{B} \times 100\%$$

Tumour response is defined in **Table 7.4**: Complete disease (CR) was identified when all lesions were no longer visible on CT, with no evidence of tumour elsewhere. Partial response disease (PR) was defined as minimum 30% decrease in the total tumour measurement at the 12-week post-treatment scan. Stable disease (SD) was defined as the change of the tumour measurement between 30% decrease and 20% increase. Progressive disease (PD) was defined as an increase of at least 20% in the total tumour measurement at the 12-week post-treatment scan.

Table 7.4: treatment response criteria using modified RECIST

	Responder		Non-responder	
Tumour response	Complete disease	Partial response	Stable disease	Progress disease
Change (%)	-100	-100 to -30	-30 to 20	>20

7.2.4.2 DWI analysis

Image process steps:

1. To improve the SNR and CNR on the DWI image, the mean DWI images at each b-value were acquired by averaging four series and three diffusion directions DWI images. ADC maps were estimated by fitting Least square to the mean DWI image.

2. The total disease volume including both the solid tumour component and pleural effusions was segmented by using a 3D semi-automatic tool, GrowCut (described in the Chapter 5), with background and foreground seeds drawn on the normal tissue

and tumour tissue respectively on the mean b = 100 s/mm^2 images. These images were chosen as both solid tumour and pleural effusions demonstrated similar signal intensities whilst maintaining good disease/background contrast among all DW images.

3. Segmented ROIs were reviewed by a radiologist and then transferred to the ADC maps (see **Figure 7.3**). Solid tumours were classified below an ADC threshold of 2000*10^{-6}mm^2/s within the whole tumour volume for each patient (discussed in Chapter 6).

4. The parameters (median ADC, and tumour volume) of the solid tumour in the baseline, 4 weeks and 12 weeks post-treatment measurements were calculated. The changes in the volume of solid tumours were measured at 4-week post-treatment and 12-week post-treatment time points to show changes in tumour burden. A significant effect is defined as the percentage changes in the tumour volume beyond the cohort limits of Agreement (LoA), which was calculated from the baseline repeatability study (Chapter 6).

5. The patient outcome evaluated by volume and ADC were compared to that evaluated by the modified RECIST criteria.

7.3 Results

7.3.1 Treatment evaluation

7.3.1.1 Treatment assessment using modified RECIST on CT

The cohort treatment response of the 18 patients in this study evaluated by modified RECIST on CT images is summarised in the Table and the response of each individual patient is shown in **Table 7.5** with more details of per-patient response presented in **Table 7.6**. According to modified criteria, only three patients in this cohort (Patient 10, Patient 15, and Patient 18) responded to the chemotherapy treatment while the remaining 15 patients did not.

Table 7.5: Overall response evaluated by modified RECIST on the clinical data

Response Category	Response		No.	%	%
Responder	Complete response	(CR)	0	0	16.7
	Partial response	(PR)	3	16.7	
Non-responder	Stable disease	(SD)	12	66.6	83.3
	Progressive disease	(PD)	3	16.7	
Total No.			18	100	100

Table 7.6: Patients outcome evaluated by Modified RECIST on CT for 18 evaluable patients who have undergone two CT scans and at least two MRI scans.

Patient No.	Sum of tumour lengths on CT1 (mm)	Sum of tumour lengths on CT2 (mm)	(%) change	Response
1	110.6	107.8	-2.5	SD
2	121.6	125.6	3.3	SD
3	71.7	97.4	35.8	PD
4	70.9	75.8	6.9	SD
5	82.5	74.9	-9.2	SD
6	132.6	147.7	11.4	SD
7	134.3	135.2	0.7	SD
8	66.5	61.5	-7.5	SD
9	91.8	102.7	11.9	SD
10	85.0	41.1	-51.7	PR
11	98.5	80.4	-18.4	SD
12	103.1	102.9	-0.2	SD
13	73.6	130.3	77.1	PD
14	91.3	118.0	29.2	PD
15	92.0	54.3	-41	PR
16	62.9	64.9	3.2	SD
17	131.5	104.3	-20.7	SD
18	89.5	51.9	-42	PR

7.3.1.2 Treatment assessment using DWI

Figure 7.3 shows an example with significant decrease in the tumour volume at both 4 weeks and 12 weeks post-treatment.

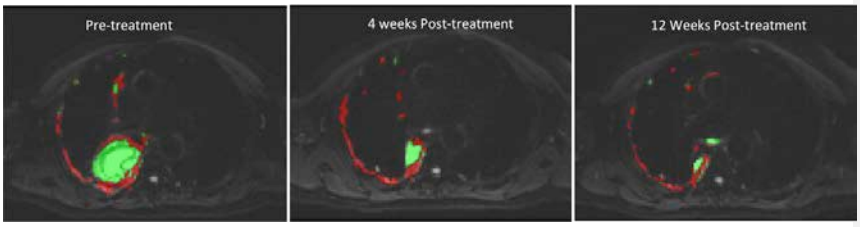

Figure 7.3: DWI images (b=100mm^2/s) of a 75-year-old male MPM patient in pre-treatment, 4 weeks and 12 weeks post-treatment scans. The red regions on the b100 images represent the classified solid tumour while the green shows the pleural effusions.

(a.) Total volume of solid tumour

The total volume of solid tumour for each patient in different time point was shown in the bar plot in **Figure 7.4** (The detail information of each patient is shown in Appendix 4 and 6), note that Patient 12-18 did not have 12 weeks post treatment MRI scan.

Figure 7.5 shows the percentage changes in solid tumour volume for each patient at 4 weeks post-treatment (V2) and 12 weeks post-treatment DWI scans (V3) compared with the baseline data (V1). The individual limit of agreement (LoA) (-13.9%, 16.2%) was calculated from the Bland-Altman statistics. The responders, defined as the percentage changes in volume is smaller than the lower LoA (-13.9%), are Patient 1, 2, 5 and 10.

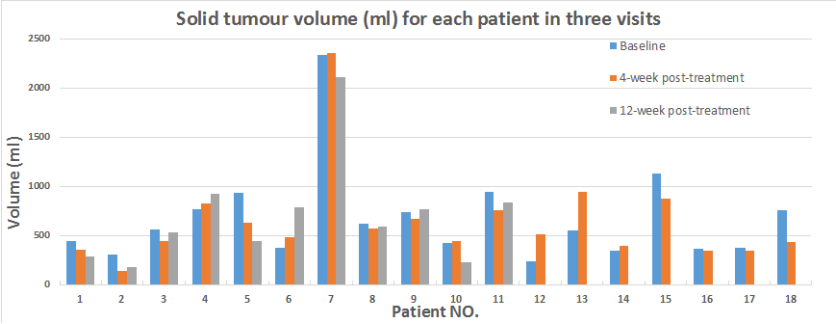

Figure 7.4: Bar plots of the solid tumour volumes for each patient at three time points (Pre-treatment, 4 weeks and 12 weeks post-treatment).

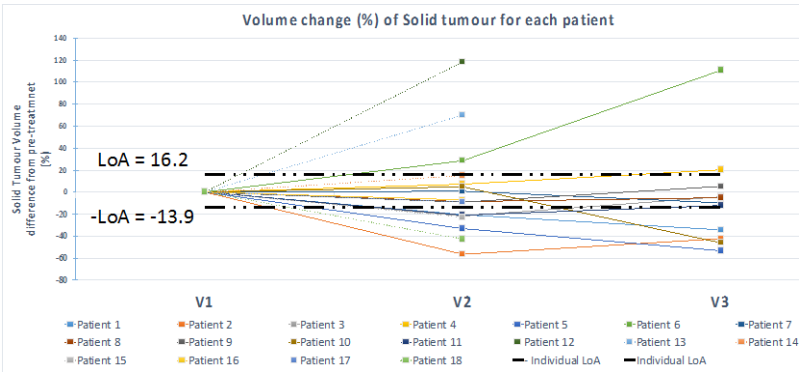

Figure 7.5: the percentage changes in solid tumour volume for each patient compared with the baseline data (V1 means baseline, V2 means 4 weeks post-treatment, and V3 means 12 weeks post-treatment).

The individual limit of agreement (LoA) was calculated from the Bland-Altman statistics (Chapter 6). One criterion of DWI volumetric method for defining responding patients is that the percentage changes in volume is smaller than the lower LoA.

(b.) Median ADC of the solid tumour

Figure 7.6 shows the median ADC values of solid tumour at three time points of MR measurement for each patient in the cohort (The detail information of each patient is shown in Appendix 5 and 7), note Patient 12-18 only has baseline and 4-week post-treatment MRI scans and did not undergo the 12-week post-treatment MRI scan.

Figure 7.7 shows the percentage changes in the median ADC of solid tumour for each patient at 4 weeks post-treatment (V2) and 12 weeks post-treatment DWI scans (V3) compared with the baseline data (V1). The individual limit of agreement (LoA) (-1.2%, 3.3%) was calculated from the Bland-Altman statistics in **Section 6.2**.

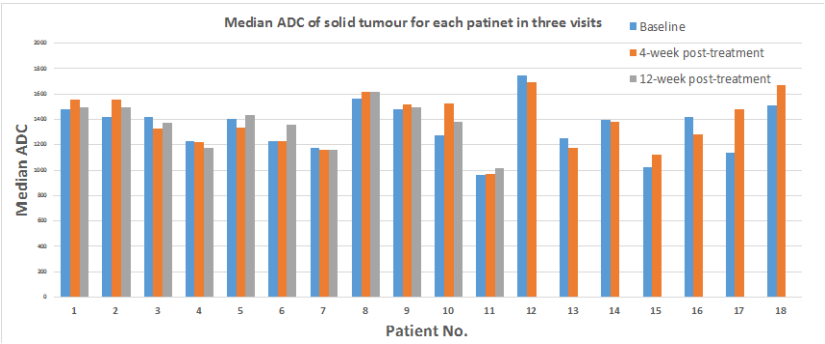

Figure 7.6: Bar plots of the median ADC (*10^{-6}mm^2/s) of solid tumour for each patient at three time points (Pre-treatment, 4 weeks and 12 weeks post-treatment).

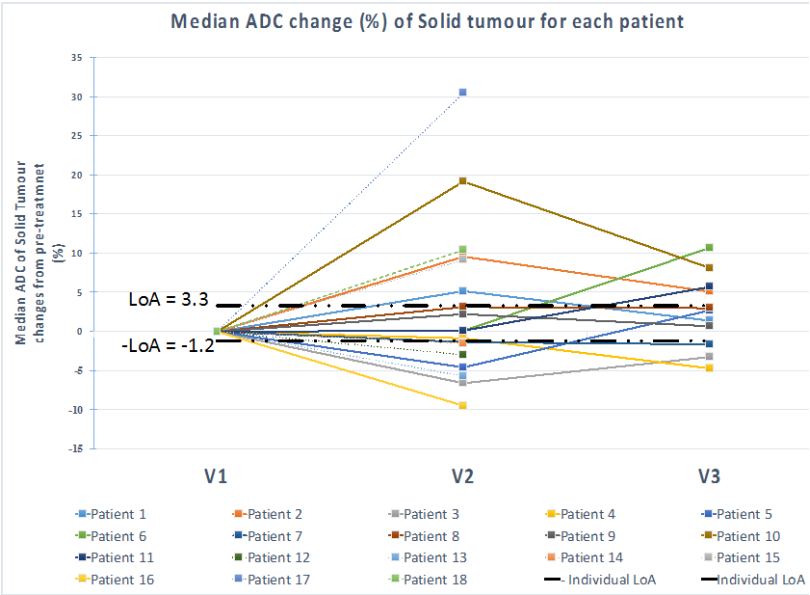

Figure 7.7: The percentage changes of median ADC in solid tumour for each patient compared with the baseline data (V1 means baseline, V2 means 4 weeks post-treatment, and V3 means 12 weeks post-treatment).

The individual limit of agreement (LoA) was calculated from the Bland-Altman statistics (Chapter 6). One criterion of DWI volumetric method for defining responding patients is that the percentage changes in median ADC of solid tumour is larger than the higher individual LoA.

(c) Volume and median ADC of solid tumour

The changes in volume and median ADC of solid tumour at 12 weeks post-treatment compared with the baseline data for the 11 patients are correlated with the treatment outcome defined by the modified RECIST criteria in **Table 7.7**.

When using the volume methods on DWI to define the responding patient, there are two criteria:

(i) the percentage change in volume of solid tumour is smaller than the lower individual LoA;

(ii) the percentage change in median ADC of solid tumour is larger than the upper individual LoA.

Patient 2, and 10 are treatment responders according to the DWI volumetric criteria: Patient 10 matches the outcome of the modified RECIST criteria, while Patient 2 does not. The remaining 9 patients are all evaluated as non-responders by volume-based DWI method and the mRECIST (**Table 7.7**).

Table 7.7: A table correlating the changes (%) in median ADC and tumour volume at 12 weeks post-treatment with outcome by mRECIST[23].

Patient No.	% change in tumour volume (12 weeks)	% change in median ADC (12 weeks)	Patient Outcome*	mREICST Outcome
1	-34.2	+1.4	+	+
2	-42.2	+5.1	−	+
3	-4.4	-3.2	+	+
4	+20.3	-4.7	+	+
5	-53.2	+2.7	+	+
6	+131	+10.7	+	+
7	-9.7	-1.6	+	+
8	-4.9	+3.0	+	+
9	+5.3	+0.7	+	+
10	-46.0	+8.1	−	−
11	-12.0	+5.7	+	+

*+ = Non-responder, - = responder

(d) Evaluation the Cohort

Figure 7.8 shows of the percentage change in the volume/ median ADC values over the patient cohort at 4 weeks (V2) and 12 weeks (V3) post-treatment compared with the baseline DWI. The plots show there is no significant treatment response effect of

[23] Note that Patient No. 12 -18 did not undergo 12-week post-treatment MRI scans so their data at 12-week time point is missing.

the whole cohort using volume or median ADC values at either 4-week or 12-week post-treatment DWI scan.

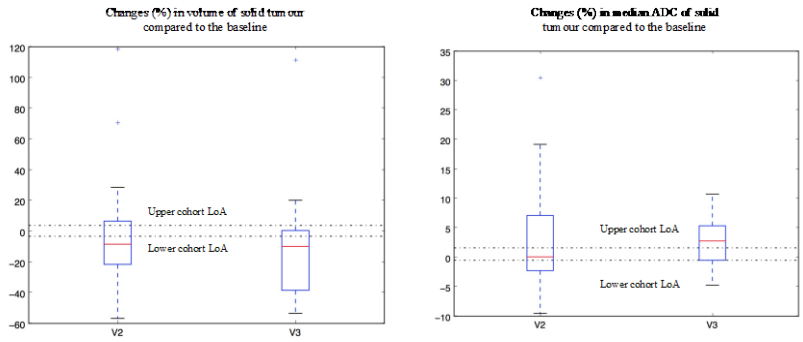

Figure 7.8: boxplots of the difference between (Left plot) the volume/ (Right plot) median ADC values over the patient cohort and the baseline value at each time point (V2 means 4 weeks post-treatment, while V3 means 12 weeks post-treatment).

The horizontal red lines are the medians; the ends of the boxes show the lower and upper quartiles (25th and 75th percentiles). The horizontal dashed lines represent the cohort Limit of Agreement as established using Bland-Altman statistics. No significant differences between post-treatment values and baseline cohort values were found.

7.3.1.3 Responders vs. Non-responders in DWI

Figure 7.9 shows the boxplots of volume changes (%) at two post-treatment scans for the responder and non-responder groups, which are defined by modified RECIST criteria. As the relative change of volumes at 4 weeks for the non-responder group is not normal distribution as shown by Shapiro-Wilk test (W = 0.854, p=0.020), Wilcoxon test has been used and the p value is 0.3 for the data in the left figure, which means there is no significant difference between the responder group and non-responder group in the change (%) of volume of the solid tumour at 4-week post treatment.

Figure 7.10 shows the boxplots of median ADC changes (%) at two post-treatment scans for the responder and non-responder groups, which are defined by modified RECIST criteria. As the relative change of ADC at 4 weeks for the non-responder group is not normal distribution as shown by Shapiro-Wilk test (W = 0.774, p=0.002), Wilcoxon test has been used and the p value is 0.027 for the data in the left figure, which means there is significant difference between the responder and non-responder groups in the change (%) of median ADC of the solid tumour at 4-week post treatment.

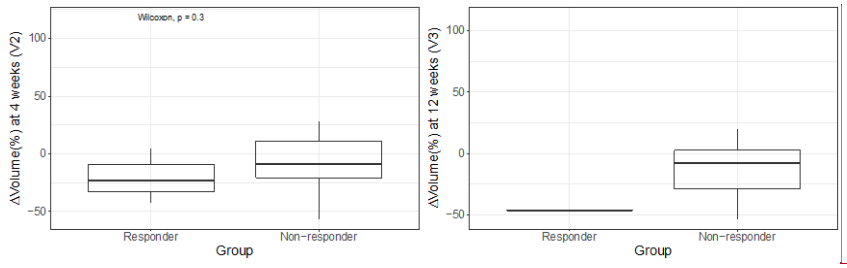

Figure 7.9: Boxplots of volume changes (%) at (Left) 4 weeks post treatment and (Right) 12 weeks posttreatment for the responder group and Non-responder group defined by modified RECIST criteria.

The horizontal lines are the medians; the ends of the boxes show the lower and upper quartiles (25th and 75th percentiles). The p value is 0.3 for the data in the left plot, which means the changes (%) of volume of the solid tumour in the responder group were not significantly different from those of non-responder group.

Commented [MOU2]: justify use of parametric statistical tests, e.g. via Shapiro-Wilk. If required, re-analyse using nonparametric test

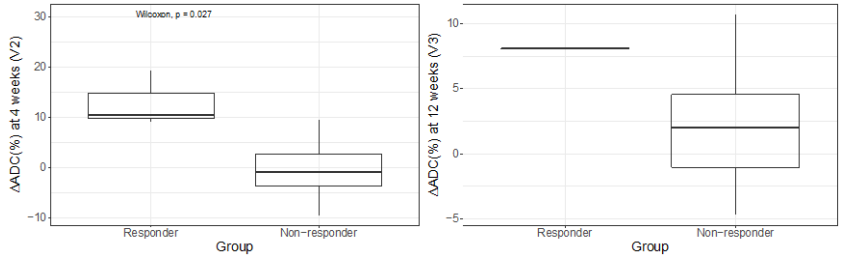

Figure 7.10: Boxplots of median ADC changes (%) at (Left) 4 weeks post treatment and (Right) 12 weeks posttreatment for the responder and Non-responder group (The two groups are defined by modified RECIST criteria).

The horizontal lines are the medians; the ends of the boxes show the lower and upper quartiles (25th and 75th percentiles). The *p* value is 0.027 for the data in the left plot, which means the changes (%) of median ADC values of the solid tumour in the responder group were significantly higher than those of non-responder group.

7.3.1.4 Correlations between mRECIST and DWI (TTC, ADC)

There is a moderate positive correlation between the mRECIST size change and the solid tumour volume change in post-treatment DWI images (either 4 weeks or 12 weeks), where the calculated Pearon's correlation coefficient *r* is 0.4 and 0.459 respectively (**Figure 7.11**).

Percentage of size changes in mRECIST and percentage of solid tumour volume changes

There is a moderate positive correlation between the mRECIST size change and the volume change of solid tumour in either 4 weeks or 12 weeks post treatment DWI images, where the calculated Pearon's correlation coefficient *r* is 0.4 and 0.436 respectively (**Figure 7.11)**

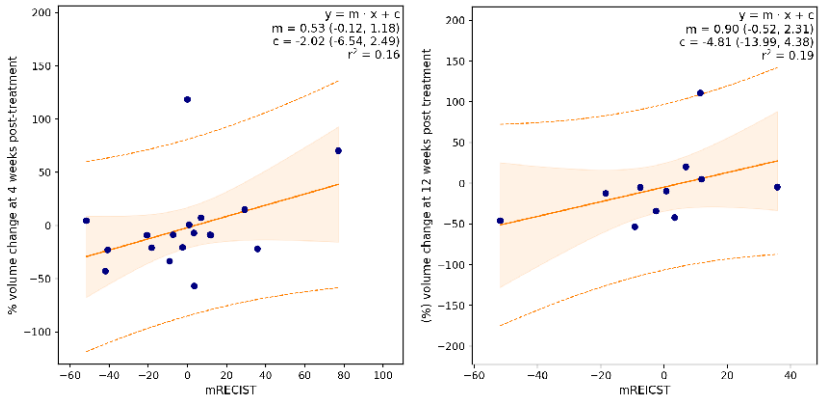

Figure 7.11: Comparison between the mRECIST size changes (%) and the changes (%) in the volume of solid tumour on DWI at different time point, 4 weeks post-treatment (Left) and 12 weeks post-treatment (Right).

There is a moderate positive correlation between the mRECIST size change and the volume change of solid tumour in either 4 weeks or 12 weeks post treatment DWI images.

Percentage of size changes in mRECIST and percentage of solid tumour median ADC changes

There is a moderate negative correlation between the mRECIST size change and the percentage change of solid tumour median ADC in post-treatment DWI images (either 4 weeks or 12 weeks), where the calculated Pearon’s correlation coefficient *r* is -0.574 and - 0.510 respectively (**Figure 7.12**).

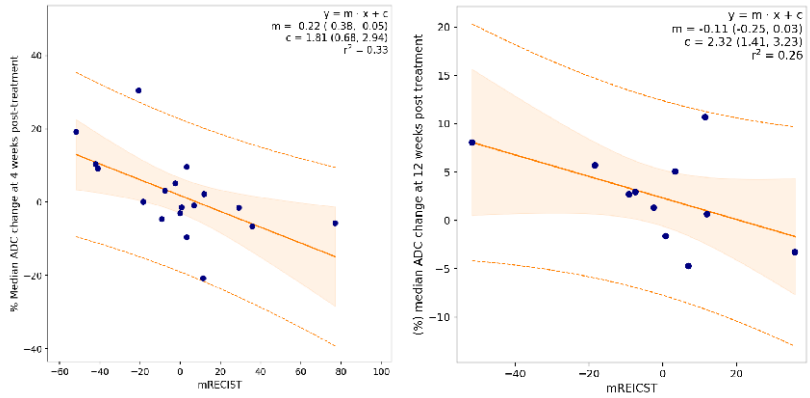

Figure 7.12: Comparison between the mRECIST size changes (%) and the changes (%) in the median ADC of solid tumour on DWI at different time point, 4 weeks post-treatment (Left plot) and 12 weeks post-treatment (Right plot).

There is a moderate negative correlation between the mRECIST and change (%) of median ADC at either 4 weeks or 12 weeks post treatment.

Percentage of changes in solid tumour median ADC and volume

There is a weak negative correlation between the percentage change in volume and the percentage change of median ADC of solid tumour in 4-week post-treatment DWI images, where the calculated Pearon's correlation coefficient *r* is -0.23.

There is a strong negative correlation between the volume change (%) and median ADC change (%) in solid tumour at the 12-week post-treatment scan (r = - 0.69) (Exclude one outlier Patient 6) (**Figure 7.13**).

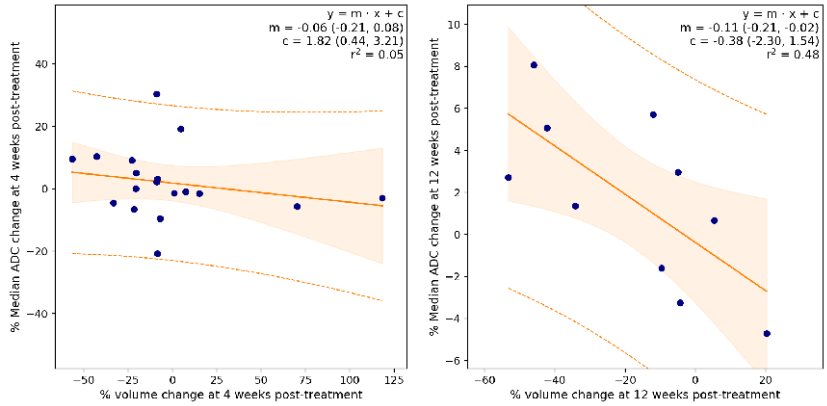

Figure 7.13: Comparison between the change (%) in solid tumour volume and the changes (%) in median ADC of solid tumour on DWI at different time point, 4 weeks post-treatment (Left plot) and 12 weeks post-treatment (Right plot).

There is a weak negative correlation between the volume change (%) and median ADC change (%) in solid tumour at the 4-week post-treatment scan (*r* = -0.23). And there is a strong negative correlation between the volume change (%) and median ADC change (%) in solid tumour at the 12-week post-treatment scan (r = - 0.69) (Exclude one outlier Patient 6)

7.3.2 Prediction overall survival using pre-treatment values

The median overall survival (OS) from starting the treatment was 48.21weeks (8.00 – 108.29 weeks). Of 18 patients, there were 17 observed deaths.

Figure 7.14 indicates that the there is no correlation between the pre-treatment solid tumour volume and the overall survival (r = 0), while there is a strong positive correlation between the pre-treatment median ADC of solid tumour and the patient overall survival (r = 0.609).

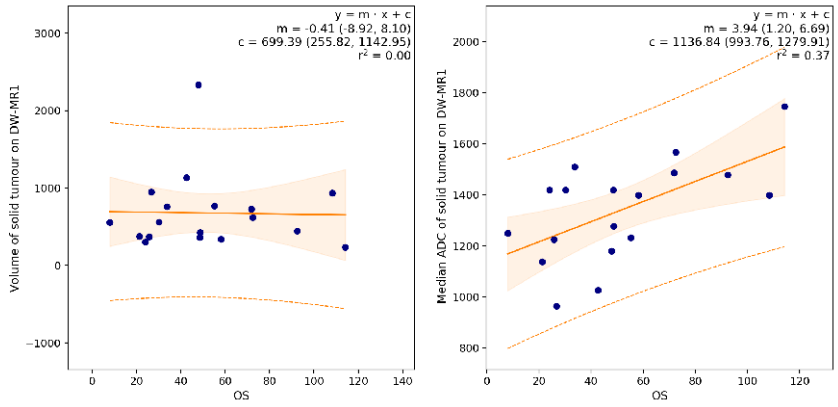

Figure 7.4: The comparison between the volume (Left)/ the median ADC (Right) of solid tumour at pre-treatment and the patient overall survival (OS) (Unit: week).

There is no correlation between the pre-treatment solid tumour volume and the overall survival (r = 0), while there is a strong positive correlation between the pre-treatment median ADC of solid tumour and the patient overall survival (r = 0.609).

7.4 Discussion

In this chapter, volume based DWI has been successfully applied on the clinical MPM patients. The treatment effect of a MPM cohort after chemotherapy has been evaluated by two methods: the modified RECIST using CT, and the volumetric method using DWI images.

7.4.1 Treatment evaluation

According to the modified RECIST criteria on the 12 weeks post-treatment CT, there are only three responders (Patient 10, 15, and 18) in this cohort, and 15 non-responders. Among all the 18 patients, seven patients (Including patient 15 and 18) did not complete the 12-week post-treatment MRI scan, therefore, there was only one

responder (Patient 10) among 11 patients evaluable for the volumetric method on 12-week post-treatment DWI.

When using the DWI volume criteria[24] to evaluate the treatment effect of the patients at 12 weeks (**Table 7.7**), there are 9 non-responders and 2 responders (Patient 2 and Patient 10, see **Table 7.7**), among which only one patient (Patient 2) was at variance with the CT results, while 10 out of 11 patients were in consistence with the modified RECIST criteria.

When evaluating the whole cohort (**Figure 7.8**), no significant difference in the volume (or median ADC) was found between post-treatment (either 4 weeks or 12 weeks) or baseline scans, which means the cohort has a heterogeneous response to the chemotherapy treatment.

7.4.1.1 Responders vs. Non-responders at early DWI follow-up (4 weeks)

It has been found that after 4 weeks after treatment the responder group (n=3) had a significantly ($p<0.05$) larger change (%) in the median ADC of the solid tumour than the non-responder group (n = 15) (**Figure 7.10**). This verifies our hypothesis that a successful anticancer treatment may cause the ADC of tumour to increase and it also indicates that the change in median ADC at early follow-up may be a good biomarker to differentiate the responder and non-responder. This is clearly helpful for the optimal treatment management of MPM as patients who do not respond to this treatment could be offered other available treatments at an early time point. The changes in solid tumour volume did not have significant difference ($p>0.05$) in the two groups.

[24] When using the volume criteria from DWI, there are two conditions should be filled:
(i) the percentage change in volume is smaller than the lower individual LoA;
(ii) the percentage change in median ADC is larger than the upper individual LoA

7.4.1.2 Correlations between treatment biomarkers

mRECIST vs. ADC change

There was a moderate negative correlation between the percentage change of solid tumour ADC in post-treatment scans (both 4 and 12 weeks) with the size change evaluated by mRECIST on CT at 12 weeks in the cohort, as the Pearson's correlation coefficient *r* is -0.574 at 4 weeks and -0.510 at 12 weeks (**Figure 7.12**).

This indicates that the percentage change of median ADC may be a good biomarker of evaluating the treatment as mRECIST is the standard method of treatment evaluation. This needs a larger cohort to verify it.

Changes in Volume vs. Changes in ADC of solid tumour

There is a strong negative correlation (r = -0.69) between the percentage change in the solid tumour ADC with the change in volume at 12 weeks from baseline in the cohort. This matched our hypothesis that an increase in ADC may be related to a decrease in the tumour volume. At the early follow-up, this correlation was weak (*r* = -0.22) (**Figure 7.14**).

7.4.2 Prediction of the overall survivals using pre-treatment data

The pre-treatment median ADC of the solid tumour has a strong positive correlation with the overall survival, which means the pre-treatment median ADC may be a good biomarker to predict the patient overall survival before the chemotherapy treatment. This should be verified in prospective studies with a larger patient cohort in the future.

7.4.3 Limitations

There are some limitations of this study: firstly, this clinical study has a very small patient cohort (18 evaluable patients), among which there are three patients responding to the treatment according to the modified RECIST. In these three responders, only one responder had undergone all three MRI scans, and makes it impossible to make a comparison between responder and non-responder groups using the 12-week post-treatment DWI data. Thus, a valid comparative analysis between

the two groups using the DWI volumetric approach remains for more available data from the responding patients. Secondly, the modified RECIST measurements were performed by one radiologist and inter-observer variance was not determined.

7.4.4 Chapter summary

The volume-based DWI analysis is the first study to date to have estimated the total solid tumour burden and evaluated the treatment effectiveness for malignant pleural mesothelioma patients following chemotherapy treatment using diffusion-weighted imaging. The results show this method appears as a prognostic and response biomarker in evaluating response and predicting patient survival. The total volume and the median ADC of the solid tumour in mesothelioma assessed with DWI have been shown to have a moderate correlation with CT measurements. Furthermore, the median ADC of solid tumour may have the potential to optimise the treatment management and improve care of mesothelioma patients receiving chemotherapy treatment by identifying responders at an early follow-up time point. It is also promising that the pre-treatment ADC values of the solid tumour in MPM may be used to predict patient survival. Further evaluations of DWI as a prognostic and response biomarker in prospective cohorts of patients is needed.

8 Conclusions

The principle objective of this PhD project was to investigate the potential of diffusion-weighted MRI for assessing chemotherapy treatment response of malignant pleural mesothelioma patients. The followings have been done to achieve the goal:

- Development of T_2-cDWI to improve DWI image contrast for MPM.
- Development of volumetric analysis method for MPM solid tumour.
- Exploration of parameters (solid tumour volume and median ADC) derived from DWI images for the evaluation of MPM treatment response.

Key results of this thesis are summarised in Section 8.1 and Section 8.2 discusses areas for the future outlook.

8.1 Summary of results

8.1.1 Enhancement of the image contrast

In malignant pleural mesothelioma, the presence of pleural effusion is common and pleural effusions have relatively high signal intensity on DWI images due to the T_2 shine-through effect, which may lead to image misinterpretation. T_2-adjusted computed DWI has been proposed in Chapter 4 to generate synthetic images at any chosen b-value and echo time, and it allows to adjust T_2- and diffusion-contrast independently. This has been achieved by acquiring additional T_2-weighted EPI images at different echo times. Using the identical EPI readout ensures that the geometry and B_0-related distortions are inherently matched between the T_2- and diffusion-weighted images. An optimal T_2-cDWI protocol has been proposed, and an analytical model has been derived for the noise properties in the proposed T_2-cDWI protocol, and validated using a diffusion test-object. The phantom experiments showed that measured image noise in T_2-cDWI of the phantom conformed to the analytical model. Besides, it demonstrated that from optimised imaging protocols T_2-cDWI at high computed b-value/TE combinations achieves lower noise compared

with conventional DWI. In clinical cases, T_2-cDWI has been shown to manipulate image contrast derived from T_2 and diffusion by computation of images at desired b-values and echo times: using high b-values and short TEs is able to overcame T_2 shine-through effects and lead to enhanced image contrast for identifying true impeded diffusion areas, such as solid tumour, compared with conventional high-b-value DW images. Conversely, employing low b-value and long TE could enhance areas with long T2-relaxation, such as pleural effusions, while suppress solid tumour components which have shorter T_2. Therefore, there is a greater degree of freedom in adjusting the image contrast by manipulating b-values and echo times independently with T_2-cDWI compared with conventional DW imaging. In this way, T2-cDWI may prove to be a useful clinical tool to enhance/eliminate the T_2 shine-through effect, thereby improving image contrast to enhance tumour detection. Clearly, this has to be investigated in future prospective studies, but the early proof of concept data appears promising.

8.1.2 Volumetric analysis method of MPM solid tumour using DWI

Tumour volume is a pivotal parameter in the assessment of MPM treatment response, which is crucial in optimal management of chemotherapy treatment at an early follow-up time point. A major aim of this project was to establish a more objective and accurate volumetric method enabled by quantitative analysis of the total solid tumour burden. This has been practically demonstrated by using semi-automatic segmentation of the MPM whole disease volume including pleural effusions and solid tumour areas (Chapter 5) followed by tumour classification of only solid tumour components (Chapter 6).

In chapter 5, two semi-automatic segmentation methods, GrowCut and Random Walk segmentations, are the first time to date being applied on diffusion-weighted images to estimate the MPM disease burden, including solid disease and pleural effusion. The two methods have been successfully implemented on the 2D and 3D DWI images using the in-house developed plugins in the OsiriX DICOM Viewer, which has a user-friendly interface and enables image processing by using pre-installed plugins. After the user defines fore- and back-ground seeds in OsiriX, it is highly automatic to generate 2D or 3D segmentations of the target with maximum one pre-set parameter.

In order to find out the optimal free parameter β for random walker, the performance of 2D Random walk segmentation at different β values has been evaluated by DICE coefficient. The results showed a highest accuracy of 2D RW segmentation achieved at β=2400. The two semi-automatic segmentations have been extended to the 3D domain to acquire the volume of the mesothelioma disease. After being successfully applied on ten clinical cases with the same initial seeds, both methods have been shown to have a good performance and an accuracy compared with the reference defined by the radiologist, while GrowCut has higher Dice coefficients than RW segmentation among the patient cohort, suggesting it is more suitable for our application and this is why it is chosen to be applied in the following chapters.

In Chapter 6, two automatic classification methods, the classical global thresholding and Gaussian mixture modelling, have been investigated to classify solid tumour from pleural effusions based on their different properties. When using our novel method that combines 3D semi-automatic (GrowCut) segmentation and global ADC thresholding, the results have shown excellent repeatability of mean and median ADC estimates and tumour volume in the diffusion-weighted imaging. In addition to these main contributions, ADC maps fitted from two different algorithms, the least square and weighted least square fitting, also have been used and compared, and the results have shown that both methods have excellent repeatability in the parameters and no significant difference between results from the two fitting models. The second classification method, the Gaussian mixture modelling method using ADC and R_2, has been the first to date applied on MPM clinical cases to characterise the heterogeneity of malignant pleural mesothelioma and achieve the classification of solid tumour component. The novelty of this method is mainly on the provision of additional quantitative functional information for disease characterisation compared with using only a single parameter, especially the two functional maps are inherently matched. The performance of this approach has been demonstrated on three available cases, and reliable results are achieved under the condition that mesothelioma disease has solid tumour and pleural effusions components, but the method may not be robust otherwise. The latter might be caused by partial volume effect, low image SNR etc. This can be investigated in the future work and might be improved by a more adaptable hypothesis, and / or imaging denoising.

In summary, this job has demonstrated substantial contributions for providing a robust volume-based analysis for evaluation of treatment response in lung mesothelioma using diffusion-weighted imaging.

8.1.3 Patient treatment evaluation

Currently, modified RECIST applied on CT images remains the most widely used method to assess MPM treatment response in clinical practice, mainly due to its easy implementation. However, compared with CT imaging, the advantages of diffusion-weighted imaging are the avoidance of radiation, higher soft tissue contrast, and additional functional information, therefore, one aim of the project is to investigate the potential of assessing tumour changes using DWI in malignant pleural mesothelioma patients and further assess the applicability of our DWI method with modified RECIST in a wider clinical context. In Chapter 7, diffusion-weighted imaging has been applied on 18 MPM patients in reasonably short image acquisition times (~12 minutes), thus the treatment response of the patient cohort has been assessed using two methods, the widely used mRECIST criteria and the proposed volumetric DWI method. The results have shown that the total volume and the median ADC of the solid tumour in MPM assessed by the proposed volume-based DWI method have a moderate correlation with CT measurements, indicating that this method can be used to suggest equivalents of the modified RECIST criteria in the volume space and tumour volume and ADC are potential response biomarkers in evaluating response of MPM. Furthermore, the median ADC of solid tumour may have potentials to optimise the treatment management of mesothelioma patients receiving chemotherapy treatment by identifying responders at an early follow-up time point, this might need to be further investigated in the future studies with a larger patient cohort. It is also promising that the pre-treatment ADC values of the solid tumour in MPM may be used to predict patient survival, and may indicate a good prognostic biomarker in predicting patient survival. Diffusion-weighted imaging with volume-based analysis provides good insight into potential volume response criteria and in the future, it has the potential to be implemented in routine clinical practice for MPM treatment evaluation.

8.2 Future work

8.2.1 Methodology improvements

This PhD project has focused on the development of a clinical protocol to acquire high quality DWI images for MPM patients and the development of volumetric methods to evaluate changes in DWI data after chemotherapy treatment. These goals have been achieved considerably well, given the challenges and constraints described in the methodology chapters, yet there are still improvements for the future investigations. First of all, due to the low incidence rate, only 18 evaluable patients have been recruited among which only 11 have undergone all the planned scans. As only 1 out of 11 patients would be classified as ‘responder’ and the rest ‘non-responders’, it is unable to do statistical analysis of treatment response at 12 weeks post-treatment. Therefore, a larger patient cohort is needed in the further work. It would also be helpful to collect more patients with additional T2-cDWI images which provides improved lesion contrast. It may enable better image segmentation and this can be investigated in a larger patient cohort. Secondly, most of the image post processing in this project has been performed via running python scripts in Osirix platform. In order for such techniques to be used more conveniently for radiologists, it would be necessary to make a user-interface panel that incorporates multiple functions such as T2-cDWI, image segmentation and classification on OsiriX. The easy use of interface panel may encourage radiologists wide use of volume-based DWI analysis and help it become feasible in the future clinical routine.

8.2.2 Image denoising

One challenge in applying DWI images in the thorax is the low SNR mainly due to the rather prolonged echo time and signal loss arising from the diffusion weighting. While higher b-values experience lower SNR, the diffusion and perfusion both attenuate the signal in lower b-value regions [5]. Therefore, there is a great need to remove the image noise and improve the SNR of the thoracic DWI images. Denoising is particularly important for image segmentation, as its performance degrades dramatically in the presence of noise and induces bias.

A potential approach, Principal component analysis (PCA) is a technique suitable for estimation problems where the aim is to generate a low rank (i.e. low dimensionality) representation of the input. As the name implies, PCA is a decomposition technique that represents the data as a sum of principle components, which are derived from the eigenvectors and eigenvalues of the covariance matrix of the input data. The eigenvalues give the data variance along the direction of the corresponding eigenvectors, and so it follows that components with larger variance should represent the salient features of the input data, while those containing less variance are mainly associated with artefacts or noise. Denoising can be achieved by discarding components with small eigenvalues since these will contain little salient information.

One example case of MPM patient has been shown using local PCA on DWI images (**Figure 8.1**). The result of local PCA shows the superior performance of local PCA and the correct estimate of matrix rank, here the salient features of the image remained intact, both morphology and contrast. In particular, the images at b-value of 800 s/mm^2, where the tumour has low SNR signal, does not affect the algorithm performance and the contrast and the anatomical features have been preserved. To our understanding, this is mainly due to the fact that the chosen rank contains the information from the high SNR, and those info are replaced for the entire patched.

In the future studies, the performance of the local PCA and other state-of-the-art methods, such as Non-Local Total Variation (NLTV), can be investigated on the thoracic DWI images in a patient cohort, and the impetus is to improve the confidence on the DWI image segmentation of mesothelioma from the perspective of improved signal-to-noise ratio. Further investigations of image segmentation based on the denoisd images might also be an interesting research area.

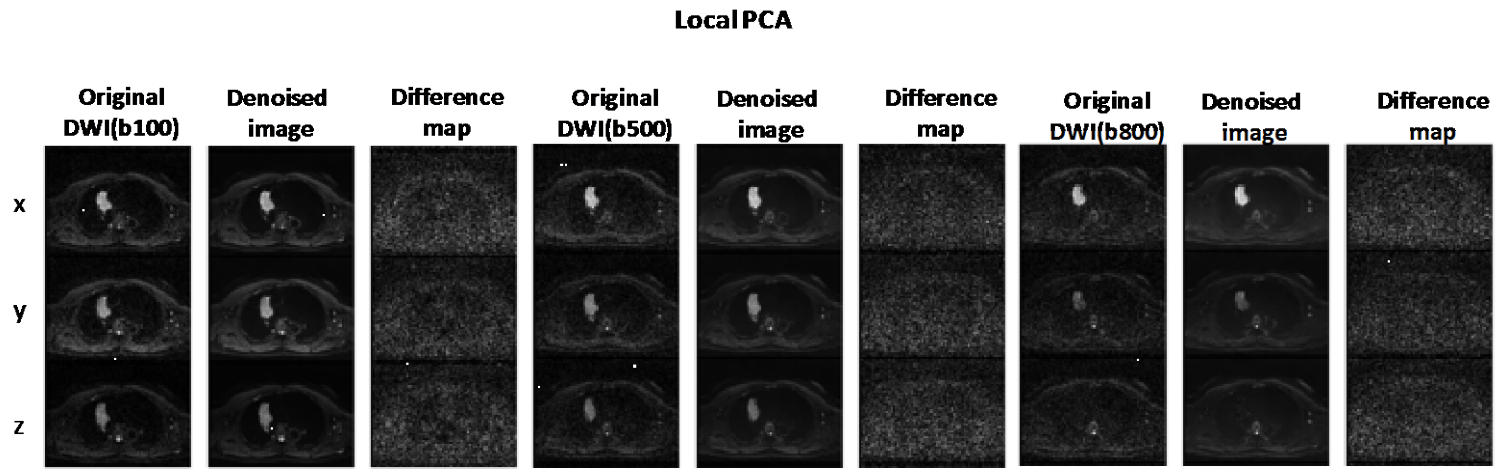

Figure 8.1:The performance of local PCA on DWI images of a 77-year-old male MPM patient acquired at different b-values.

The column 1, 4, and 7 are the original DWI acquired at three b-values at different gradient directions, the column 2, 5, and 8 are the corresponding denoised images using local PCA and the column 3, 6, and 9 are the estimated difference map between the original and the denoised images (the residual error).

8.2.3 Image segmentation

One shortcoming of the image segmentation methods used in this work is that both need initial user input and manual modification of the segmented volumes, which is still time intensive for radiologists. The performance of image segmentation should be improved to face the trade-off between time efficient and reliable quantification. It would be interesting to examine the performance of different automatic algorithms in image segmentation if they have high reproducibility and low inter-observer variability. Approaches, such as Markov random field, neural network etc. are potentially adaptable to the case in hand, and can be calibrated to face the challenges such as intensity inhomogeneity and various induced biases and noisy data. Yet the question of "whether the advantage of one to the other is clinically relevant?" remains unexplored. The key parameter, however, is a set of metrics to be employed in such comparisonal analysis to appraise image segmentation algorithms in a comprehensive manner than concluding based on one single merit (such as Dice coefficient in this study). In addition, it is also necessary to extend the considerations to other aspects of image segmentation, such as methodology robustness to noise and thin structures, speed and computational complexity. This line of research requires the tandem investigation of both parties, algorithm developer and the radiologist in order to improve the confidence in the segmentation outcome and achieve a high level of interpretable delivery.

Appendix 1: New International staging system for diffuse malignant pleural mesothelioma

	Stage	Definition
T1	T1a	Tumour limited to the ipsilateral parietal pleura, including mediastinal and diaphragmatic pleura: no involvement of the visceral pleura.
	T1b	Tumour involving the ipsilateral parietal pleura, including mediastinal and diaphragmatic pleura; scattered foci of tumour also involving the visceral pleura.
T2		Tumour involving each of the ipsilateral pleural surfaces (parietal, mediastinal, diaphragmatic, and visceral pleura). Involvement of diaphragmatic muscle. Confluent visceral pleural tumour (including the fissures) or extension of tumour from visceral pleura into the underlying pulmonary parenchyma.
T3		Describes locally advanced but potentially resectable tumour. Tumour involving all of the ipsilateral pleural surfaces (parietal, mediastinal, diaphragmatic, and visceral pleura) with at least one of the following features: Involvement of the endothoracic fascia. Extension into the mediastinal fat. Solitary, completely resectable focus of tumour extending into the soft tissues of the chest wall. Nontransmural involvement of the pericardium.
T4		Describes locally advanced technically unresectable tumour. Tumour involving all of the ipsilateral pleural surfaces (parietal, mediastinal, diaphragmatic, and visceral) with at least one of the following features: Diffuse extension or multifocal masses of tumour in the chest wall, with or without associated rib destruction. Direct transdiaphragmatic extension of tumour to the peritoneum. Direct extension of tumour to the contralateral pleura. Direct extension of tumour to one or more mediastinal organs.

Appendix 1: New International staging system for diffuse malignant pleural mesothelioma

		Direct extension of tumour into the spine. Tumour extending through to the internal surface of the pericardium with or without a pericardial effusion, or tumour involving the myocardium.
N	Lymph nodes	
	NX	Regional lymph nodes cannot be assessed.
	N0	No regional lymph node metastases
	N1	Metastases in the ipsilateral bronchopulmonary or hilar lymph nodes.
	N2	Metastases in the subcarinal or ipsilateral mediastinal lymph nodes, including the ipsilateral internal mammary nodes.
	N3	Metastases in the contralateral mediastinal, contralateral internal mammary, ipsilateral, or contralateral supraclavicular lymph nodes.
M	Metastases	
	MX	Presence of distant metastases cannot be assessed.
	M0	No distant metastasis.
	M1	Distant metastasis present.
Stage I	Ia	T1aN0M0
	Ib	T1bN0M0
Stage II	T2N0M0	
Stage III	Any T3M0	
	Any N1M0	
	Any N2M0	
Stage IV	Any T4	
	Any N3	
	Any M1	

Data from Rusch VW, Group TIMI. A proposed new international TNM staging system for malignant pleural mesothelioma from the International Mesothelioma Interest Group. Chest 1995;108:16

Appendix 2: The revised Brigham and Women′s Hospital surgical staging system for malignant pleural mesothelioma

Stage No.	Definition
I	Disease confined within capsule of the parietal pleura: ipsilateral pleura, lung, pericardium, diaphragm, or chest wall disease limited to previous biopsy sites.
II	All of stage I with positive intrapleural (N1) lymph nodes.
III	Local extension of disease into chest wall or mediastinum; heart or through diaphragm, peritoneum; with or without extrapleural (N2) or contralateral (N3) lymph node involvement
IV	Distant metastatic disease.

Data from DJ Sugarbaker, Flores RM, Jaklitsch MT, et al. Resection margins, extrapleural nodal status, and cell type determine postoperative long-term survival in trimodality therapy of malignant pleural mesothelioma: results in 183 patients. J Thorac Cardiovasc Surg 1999; 117(1):5

Appendix 3: Guideline and cheeksheet of the clinical mesothelioma study

TOTEM Mesothelioma Study CCR4035
MRI Guideline & Checksheet

Visit Details

Research Site: ☐ **Scanner:** ☐ **Date:** ☐

Study/Visit ID: ☐ **Start Time:** ☐ **End Time:** ☐

Patient Details

Patient Name: .....**Hospital ID:** .....

DOB: .....**Weight (kg):** .....

Pathology: .....**Lesion location:** .....

Scanning Protocol: TOTEM CCR4035

Diffusion Weighted MR Imaging Guidelines:

General Comments

The aim of this study is to compare the median total tumour volume (TTV) and global apparent diffusion coefficient (gADC) at 4 and 12 weeks after treatment with pre-treatment values in lung mesothelioma. The scans are acquired at three time points: pre-treatment, at 4 and 12 weeks after treatment.

For the patients enrolled in this clinical trial, we aim to standardize the methods used across imaging equipment. The patients should be scanned on the AVANTO MRI scanner with the same imaging parameters (described below), in order to eliminate the variability between the measurements and to assess the reproducibility of the measurements.

Patient Preparation

Please give full explanation to the patient and inform then about vibration and sound levels during some of the scans. Complete the MRI safety questionnaire, per institutional standard, the approximate length of the scanning session and the importance of keeping still. Ensure that the patients visit the toilet before entering the

scan room, remove all metallic objects and ask the patient to change into a hospital gown.

Patient Positioning

The patient positioning should be kept unchanged throughout the duration of the trial.

a) The patient should be positioned supine (on his/ her back) on the magnet bed, with the arms close to the body.
b) A "whole body coil" must always be used for the radiofrequency (RF) transmission. The same body array coil (A/B) should be used across visits in the same position.
c) Please, make sure that the coil is positioned tightly across the patient to restrict respiratory motion.

Check-sheet and sequence details:

Comments

- The patients should be at least 1 week away from any previous intervention.
- There will be no intervention between scans.
- Scans acquired at three time points (pre-treatment, at 4 and 12 weeks after treatment)

Set-up

- Patient Position: Arms down and pulled in close to the body
- Head: Pillow or use of holder structure
- Coils: Body array coils "A" or "B" (full lung coverage)

Protocol page
Protocols Path Directory:

A. Localisers

1. Localizerchest

3-plane localizer
free-breathing

2. t2_trufi_localizer_bh

Orientation	Axial, sagittal, coronal	**Respiratory Control**	Breath-hold on inspiration
TR (ms)	3.61	**TE (ms)**	1.81
Slice Thickness (mm)	6	**Number of Slices**	5 per orientation

B. Morphological Sequences

3. 3D T1-weighted (fl3d_vibe_tra)

Orientation	Axial	**Respiratory Control**	Breath-hold on inspiration
TR (ms)	2.39	**TE (ms)**	0.78
Slice Thickness (mm)	5	**Number of Slices**	52
FoV read (mm)	380	**Acquired Pixel Resolution (mm)**	1.5 x 1.5

4. 3D T2-weighted (t2_3D_COR_space)

Orientation	Coronal	**Respiratory Control**	Free-breathing with navigator
TR (ms)	N/A	**TE (ms)**	100
Slice Thickness (mm)	3	**Number of slices**	60
Fat Suppression	IR	**NSA**	2
FoV read (mm)	360	**Acquired Pixel Resolution (mm)**	1.9 x 1.9
Any changes performed?			

C. Dynamic Sequence

5. Dynamic T2_weighted T2 (t2_trufi_COR_FB)

Orientation	Coronal	**Respiratory Control**	Free-breathing
TR (ms)	3.02	**TE (ms)**	1.51
Slice Thickness (mm)	6	**Number of slices**	1
NSA		1 with 60 measurements	
FoV read (mm)	360	**Acquired Pixel Resolution (mm)**	0.7 x 0.7
Any changes performed?			

D) Diffusion Sequences

All functional imaging slices to be centred on the same slice; seek radiological input.

6. epi_100_500_800_SPAIR

Note: *Use sequence 6 (SPAIR) first. If the fat suppression is not good, use sequence 7 (epi_100_500_800_IR).*

Orientation	Axial	**Respiratory Control**	Free-breathing
TR (ms)	≥ 8000	**TE (ms)**	82
Slice Thickness (mm)	5	**Number of slices**	≤40
Fat Suppression	SPAIR	**NSA**	4
FoV read (mm)	380	**Acquired Pixel Resolution (mm)**	3 x 3
Diffusion Mode	Orthogonal	**b-values (s/mm^2)**	100, 500, 800
*Run the sequence four times. Copy centre of slices and adjust volume from **scan 3*** *30-40 slices are proposed; besides, two scanning volumes are suggested.*			
TR			
Number of slices			
Number of stacks			
FoV (phase %)			
Acquisition time			
Any changes performed?			

7.epi_100_500_800_IR

***Note**: <u>This measurement is optional.</u>*

Orientation	Axial	**Respiratory Control**	Free-breathing
TR (ms)	≥ 8000	**TE (ms)**	70.8
Slice Thickness (mm)	5	**Number of slices**	≤40
Fat Suppression	STIR (TI: 180ms)	**NSA**	4
FoV read (mm)	380	**Acquired Pixel Resolution (mm)**	3 x 3
Diffusion Mode	3 Scan Trace	**b-values (s/mm^2)**	100, 500, 800
Run the sequence four times. Copy position from DWI sequence *Copy centre of slices and adjust volume from scan 3.* *30-40 slices are proposed; besides, two scanning volumes are suggested.*			
TR			

Number of slices	
Number of stacks	
FoV (phase %)	
Acquisition time	
Any changes performed?	

E) Diffusion T2 Sequences

8. epi_0_SPAIR

*Use the same location and parameters (except TE and b value) as **scan 6**).*
*Run the sequence with different echo times (*82, TE_{min}, TE_{max}*)*

Orientation	Axial	**Respiratory Control**	Free-breathing
TR (ms)	≥ 8000	**TE (ms)**	TE_{min}, 82, TE_{max}
Slice Thickness (mm)	5	**Number of slices**	≤40
Fat Suppression	SPAIR	**NSA**	4
FoV read (mm)	380	**Acquired Pixel Resolution (mm)**	3 x 3
Diffusion Mode	Orthogonal	**b-values (s/mm^2)**	0
TR			
Number of slices			
Number of stacks			
FoV (phase %)			
Acquisition time			
Any changes performed?			

9. epi_0_IR

***Note**: <u>This measurement is optional, only run it when sequence 7 is used.</u>*
Use the same centre and parameters (except TE and b value) as scan 7).
*Run sequence with different echo times (*70.8ms, TE_{min}, TE_{max}*)*

Orientation	Axial	**Respiratory Control**	Free-breathing
TR (ms)	≥ 8000	**TE (ms)**	TE_{min}, 70.8, TE_{max}
Slice Thickness (mm)	5	**Number of slices**	≤40
Fat Suppression	SPAIR	**NSA**	4
FoV read (mm)	380	**Acquired Pixel Resolution (mm)**	3 x 3
Diffusion Mode	3 Scan Trace	**b-values (s/mm^2)**	0
TR			
Number of slices			

Number of stacks	
FoV (phase %)	
Acquisition time	
Any changes performed?	

Complete the Lab book for this patient visit	

Data Archive:

- Clinical Images to PACS…… ☐
- Archive to Clinical Disc (record disc number) …… ☐
- Non-anonymised study to trial disc, leave in folder with completed checksheet . ☐
- Anonymise dataset: **TOTxx_yy_Z (x = patient, y = visit, Z = site tag)** eg TOT01_01_RMH…… ☐
- Anonymised data sent for central analysis ……..... . ☐

Until online system is working please refer to trial coordinator for correct method.

Appendix 4: The volume of the solid tumour at baseline and 12 weeks post treatment.

Patient No.	Solid tumour Volume on DW11 (ml)	Solid tumour Volume on DW13 (ml)	Absolute difference (ml)	%difference
1	442.3	291	-151.3	-34.2
2	304.8	176.1	-128.7	-42.2
3	560	535.6	-24.4	-4.4
4	768.3	924	155.7	20.3
5	936.3	437.8	-498.5	-53.2
6	373.7	788	444.3	131
7	2333.7	2108	-225.7	-9.7
8	621.2	590.6	-30.6	-4.9
9	729.6	768.5	38.9	5.3
10	425.7	229.8	-195.9	-46.0
11	947.9	833.9	-114.0	-12.0

Appendix 5: The median ADC of the solid tumour at baseline and 12 weeks post treatment.

Patient No.	Median ADC of solid tumour on DWI1 ($*10^{-6}mm^2/s$)	Median ADC of soild tumour on DWI3 ($*10^{-6}mm^2/s$)	Absolute difference ($*10^{-6}mm^2/s$)	% difference
1	1478	1498	20.0	1.4
2	1419	1491	72.0	5.1
3	1419	1373	-46.0	-3.2
4	1231	1173	-58.0	-4.7
5	1399	1437	38.0	2.7
6	1225	1356	131	10.7
7	1179	1160	-19.0	-1.6
8	1567	1613.5	46.5	3.0
9	1486	1496	10.0	0.7
10	1277	1380	103.0	8.1
11	964	1019	55.0	5.7

Appendix 6: The volume of the solid tumour at baseline and 4 weeks post treatment.

Patient No.	Solid tumour Volume on DW-MR1 (ml)	Solid tumour volume on DW-MR2 (ml)	Absolute difference (ml)	% difference
1	442.3	351.4	-90.9	-20.6
2	304.8	132.3	-172.5	-56.6
3	560	438.1	-121.9	-21.8
4	768.3	825	56.7	7.4
5	936.3	624.4	-311.9	-33.3
6	424.4	388	-36.4	-8.6
7	2333.7	2354	20.3	0.9
8	621.2	568.4	-52.8	-8.5
9	729.6	664.8	-64.8	-8.9
10	425.7	445.8	20.1	4.7
11	947.9	751.5	-196.4	-20.7
12	235.6	514.4	278.8	118.3
13	554.8	944.5	389.7	70.2
14	340.3	391.7	51.4	15.1
15	1133.7	874.7	-259	-22.8
16	363.3	338.1	-25.2	-6.9
17	376.6	343.3	-33.3	-8.8
18	761.8	435.8	-326	-42.8

Appendix 7: The median ADC of the solid tumour at baseline and 4 weeks post treatment.

Patient No.	Median ADC of solid tumour on DW-MR1 ($*10^{-6}mm^2/s$)	Median ADC of soild tumour on DW-MR2 ($*10^{-6}mm^2/s$)	Absolut difference ($*10^{-6}mm^2/s$)	% difference
1	1478	1554	76	5.1
2	1419	1555	136	9.6
3	1419	1325.5	-93.5	-6.6
4	1231	1220	-11	-0.9
5	1399	1335	-64	-4.6
6	1192.5	945	-247.5	-20.8
7	1179	1163	-16	-1.4
8	1567	1616	49	3.1
9	1486	1519	33	2.2
10	1277	1522	245	19.2
11	964	965	1	0.1
12	1746	1694	-52	-3.0
13	1250	1179	-71	-5.7
14	1398	1377	-21	-1.5
15	1026	1120	94	9.2
16	1419	1284	-135	-9.5
17	1137	1483	346	30.4
18	1509	1666	157	10.4

Bibliography

Uncategorized References

1 Robinson BW, Lake RA (2005) Advances in malignant mesothelioma. New England Journal of Medicine 353:1591-1603

2 Gill RR, Umeoka S, Mamata H et al (2010) Diffusion-weighted MRI of malignant pleural mesothelioma: preliminary assessment of apparent diffusion coefficient in histologic subtypes. American Journal of Roentgenology 195:W125-W130

3 Broncano J, García-Velloso MJ, Martin-Noguerol T, Luna A (2014) Functional imaging of malignant pleural mesothelioma and other pleural and chest wall lesionsFunctional Imaging in Oncology. Springer, pp 751-770

4 Armato SG, Oxnard GR, MacMahon H et al (2004) Measurement of mesothelioma on thoracic CT scans: A comparison of manual and computer-assisted techniques. Medical Physics 31:1105-1115

5 Le Bihan D, Breton E, Lallemand D, Aubin M, Vignaud J, Laval-Jeantet M (1988) Separation of diffusion and perfusion in intravoxel incoherent motion MR imaging. Radiology 168:497-505

6 Tsao AS, Wistuba I, Roth JA, Kindler HL (2009) Malignant pleural mesothelioma. Journal of Clinical Oncology 27:2081-2090

7 Sugarbaker DJ, Flores RM, Jaklitsch MT et al (1999) Resection margins, extrapleural nodal status, and cell type determine postoperative long-term survival in trimodality therapy of malignant pleural mesothelioma: results in 183 patients. The Journal of thoracic and cardiovascular surgery 117:54-65

8 Knuuttila A, Halme M, Kivisaari L, Kivisaari A, Salo J, Mattson K (1998) The clinical importance of magnetic resonance imaging versus computed tomography in malignant pleural mesothelioma. Lung Cancer 22:215-225

9 Lansberg MG, Albers GW, Beaulieu C, Marks MP (2000) Comparison of diffusion-weighted MRI and CT in acute stroke. Neurology 54:1557-1561

10 Plathow C, Klopp M, Thieke C et al (2008) Therapy response in malignant pleural mesothelioma-role of MRI using RECIST, modified RECIST and volumetric approaches in comparison with CT. European radiology 18:1635-1643

11 Rusch VW (1995) A proposed new international TNM staging system for malignant pleural mesothelioma. From the International Mesothelioma Interest Group. Chest 108:1122-1128

12 Opitz I, Kestenholz P, Lardinois D et al (2006) Incidence and management of complications after neoadjuvant chemotherapy followed by extrapleural pneumonectomy for malignant pleural mesothelioma. Eur J Cardiothorac Surg 29:579-584

13 Butchart EG, Ashcroft T, Barnsley WC, Holden MP (1976) Pleuropneumonectomy in the management of diffuse malignant mesothelioma of the pleura. Experience with 29 patients. Thorax 31:15-24

14 Sugarbaker DJ, Garcia JP, Richards WG et al (1996) Extrapleural pneumonectomy in the multimodality therapy of malignant pleural mesothelioma. Results in 120 consecutive patients. Annals of surgery 224:288

15 Sugarbaker DJ, Jaklitsch MT, Bueno R et al (2004) Prevention, early detection, and management of complications after 328 consecutive extrapleural pneumonectomies. The Journal of thoracic and cardiovascular surgery 128:138-146
16 Maziak DE, Gagliardi A, Haynes AE, Mackay JA, Evans WK, Group CCOPiE-bCLCDS (2005) Surgical management of malignant pleural mesothelioma: a systematic review and evidence summary. Lung cancer 48:157-169
17 Lang-Lazdunski L, Bille A, Lal R et al (2012) Pleurectomy/decortication is superior to extrapleural pneumonectomy in the multimodality management of patients with malignant pleural mesothelioma. Journal of Thoracic Oncology 7:737-743
18 Vogelzang NJ, Rusthoven JJ, Symanowski J et al (2003) Phase III study of pemetrexed in combination with cisplatin versus cisplatin alone in patients with malignant pleural mesothelioma. Journal of clinical oncology 21:2636-2644
19 Frauenfelder T, Tutic M, Weder W et al (2011) Volumetry: an alternative to assess therapy response for malignant pleural mesothelioma? Eur Respir J 38:162-168
20 Malayeri AA, El Khouli RH, Zaheer A et al (2011) Principles and applications of diffusion-weighted imaging in cancer detection, staging, and treatment follow-up. Radiographics 31:1773-1791
21 Koh D-M, Collins DJ (2007) Diffusion-weighted MRI in the body: applications and challenges in oncology. American Journal of Roentgenology 188:1622-1635
22 Kang H, Lee HY, Lee KS, Kim J-H (2012) Imaging-based tumor treatment response evaluation: review of conventional, new, and emerging concepts. Korean Journal of Radiology 13:371-390
23 Matoba M, Tonami H, Kondou T et al (2007) Lung Carcinoma: Diffusion-weighted MR Imaging—Preliminary Evaluation with Apparent Diffusion Coefficient 1. Radiology 243:570-577
24 Razek A (2011) Diffusion magnetic resonance imaging of chest tumors. Cancer imaging: the official publication of the International Cancer Imaging Society 12:452-463
25 Bonomo L, Feragalli B, Sacco R, Merlino B, Storto ML (2000) Malignant pleural disease. European journal of radiology 34:98-118
26 Truong MT, Viswanathan C, Godoy MB, Carter BW, Marom EM (2013) Malignant Pleural Mesothelioma: Role of CT, MRI, and PET/CT in Staging Evaluation and Treatment ConsiderationsSeminars in roentgenology. Elsevier Science, pp 323-334
27 Cardinale L, Ardissone F, Gned D, Sverzellati N, Piacibello E, Veltri A Diagnostic Imaging and workup of Malignant Pleural Mesothelioma.
28 Gill RR, Gerbaudo VH, Jacobson FL et al (2008) MR imaging of benign and malignant pleural disease. Magnetic resonance imaging clinics of North America 16:319-339
29 Benamore R, O'Doherty M, Entwisle J (2005) Use of imaging in the management of malignant pleural mesothelioma. Clinical radiology 60:1237-1247
30 Hierholzer J, Luo L, Bittner RC et al (2000) MRI and CT in the differential diagnosis of pleural disease. CHEST Journal 118:604-609

31 Heelan R, Rusch V, Begg C, Panicek D, Caravelli J, Eisen C (1999) Staging of malignant pleural mesothelioma: comparison of CT and MR imaging. AJR American journal of roentgenology 172:1039-1047

32 Patz Jr E, Shaffer K, Piwnica-Worms D et al (1992) Malignant pleural mesothelioma: value of CT and MR imaging in predicting resectability. AJR American journal of roentgenology 159:961-966

33 Stewart D, Waller D, Edwards J, Jeyapalan K, Entwisle J (2003) Is there a role for pre-operative contrast-enhanced magnetic resonance imaging for radical surgery in malignant pleural mesothelioma? European journal of cardio-thoracic surgery 24:1019-1024

34 Miller AB, Hoogstraten B, Staquet M, Winkler A (1981) Reporting results of cancer treatment. Cancer 47:207-214

35 Tsuchida Y, Therasse P (2001) Response evaluation criteria in solid tumors (RECIST): new guidelines. Med Pediatr Oncol 37:1-3

36 Eisenhauer EA, Therasse P, Bogaerts J et al (2009) New response evaluation criteria in solid tumours: revised RECIST guideline (version 1.1). Eur J Cancer 45:228-247

37 Oxnard GR, Armato SG, 3rd, Kindler HL (2006) Modeling of mesothelioma growth demonstrates weaknesses of current response criteria. Lung Cancer 52:141-148

38 van Klaveren RJ, Aerts JG, de Bruin H, Giaccone G, Manegold C, van Meerbeeck JP (2004) Inadequacy of the RECIST criteria for response evaluation in patients with malignant pleural mesothelioma. Lung Cancer 43:63-69

39 Labby ZE, Straus C, Caligiuri P et al (2013) Variability of tumor area measurements for response assessment in malignant pleural mesothelioma. Med Phys 40:081916

40 Byrne MJ, Nowak AK (2004) Modified RECIST criteria for assessment of response in malignant pleural mesothelioma. Ann Oncol 15:257-260

41 Tsao AS, Garland L, Redman M, Kernstine K, Gandara D, Marom EM (2011) A practical guide of the Southwest Oncology Group to measure malignant pleural mesothelioma tumors by RECIST and modified RECIST criteria. J Thorac Oncol 6:598-601

42 Nackaerts K, Vansteenkiste J, Nafteux P (2011) A practical guide to measure "all" malignant pleural mesothelioma tumors by modified RECIST criteria? J Thorac Oncol 6:2143-2144; author reply 2144-2145

43 Armato SG, 3rd, Nowak AK, Francis RJ, Kocherginsky M, Byrne MJ (2014) Observer variability in mesothelioma tumor thickness measurements: defining minimally measurable lesions. J Thorac Oncol 9:1187-1194

44 Plathow C, Klopp M, Thieke C et al (2008) Therapy response in malignant pleural mesothelioma-role of MRI using RECIST, modified RECIST and volumetric approaches in comparison with CT. Eur Radiol 18:1635-1643

45 Blayney JK, Ceresoli GL, Castagneto B et al (2012) Response to chemotherapy is predictive in relation to longer overall survival in an individual patient combined-analysis with pleural mesothelioma. Eur J Cancer 48:2983-2992

46 Bech C, Sorensen JB (2010) Chemotherapy induced pathologic complete response in malignant pleural mesothelioma: a review and case report. J Thorac Oncol 5:735-740

47 Pasello G, Altavilla G, Bonanno L, Rea F, Favaretto AG (2010) A pathological complete response after preoperative chemotherapy with carboplatin and pemetrexed in malignant pleural mesothelioma: A case report. J Thorac Dis 2:254
48 Ak G, Metintas M, Metintas S, Yildirim H, Ozkan R, Ozden H (2010) Three-dimensional evaluation of chemotherapy response in malignant pleural mesothelioma. Eur J Radiol 74:130-135
49 Francis RJ, Byrne MJ, van der Schaaf AA et al (2007) Early prediction of response to chemotherapy and survival in malignant pleural mesothelioma using a novel semiautomated 3-dimensional volume-based analysis of serial 18F-FDG PET scans. J Nucl Med 48:1449-1458
50 Labby ZE, Nowak AK, Dignam JJ, Straus C, Kindler HL, Armato SG, 3rd (2013) Disease volumes as a marker for patient response in malignant pleural mesothelioma. Ann Oncol 24:999-1005
51 Labby ZE, Armato SG, 3rd, Dignam JJ, Straus C, Kindler HL, Nowak AK (2013) Lung volume measurements as a surrogate marker for patient response in malignant pleural mesothelioma. J Thorac Oncol 8:478-486
52 Nanni C, Castellucci P, Farsad M et al (2004) Role of 18F-FDG PET for evaluating malignant pleural mesothelioma. Cancer Biother Radiopharm 19:149-154
53 Zubeldia J, Abou-Zied M, Nabi H (2000) 11. Evaluation of Patients with Known Mesothelioma with 18F-Fluorodeoxyglucose and PET. Comparison with Computed Tomography. Clin Positron Imaging 3:165
54 Ambrosini V, Rubello D, Nanni C et al (2005) Additional value of hybrid PET/CT fusion imaging vs. conventional CT scan alone in the staging and management of patients with malignant pleural mesothelioma. Nucl Med Rev Cent East Eur 8:111-115
55 Truong MT, Marom EM, Erasmus JJ (2006) Preoperative evaluation of patients with malignant pleural mesothelioma: role of integrated CT-PET imaging. J Thorac Imaging 21:146-153
56 Kruger S, Pauls S, Mottaghy FM et al (2007) Integrated FDG PET-CT imaging improves staging in malignant pleural mesothelioma. Nuklearmedizin 46:239-243
57 Otsuka H, Terazawa K, Morita N, Otomi Y, Yamashita K, Nishitani H (2009) Is FDG-PET/CT useful for managing malignant pleural mesothelioma? J Med Invest 56:16-20
58 Gerbaudo VH, Mamede M, Trotman-Dickenson B, Hatabu H, Sugarbaker DJ (2011) FDG PET/CT patterns of treatment failure of malignant pleural mesothelioma: relationship to histologic type, treatment algorithm, and survival. Eur J Nucl Med Mol Imaging 38:810-821
59 Niccoli-Asabella A, Notaristefano A, Rubini D et al (2013) 18F-FDG PET/CT in suspected recurrences of epithelial malignant pleural mesothelioma in asbestos-fibers-exposed patients (comparison to standard diagnostic follow-up). Clin Imaging 37:1098-1103
60 Kawaguchi K, Taniguchi T, Usami N et al (2014) FDG PET/CT is useful for detecting infiltration to the port site in patients with malignant pleural mesothelioma. Gen Thorac Cardiovasc Surg 62:157-162
61 Feigen M, Lee ST, Lawford C et al (2011) Establishing locoregional control of malignant pleural mesothelioma using high-dose radiotherapy and (18) F-FDG PET/CT scan correlation. J Med Imaging Radiat Oncol 55:320-332

62 Fodor A, Fiorino C, Dell'Oca I et al (2011) PET-guided dose escalation tomotherapy in malignant pleural mesothelioma. Strahlenther Onkol 187:736-743
63 Wahl RL, Jacene H, Kasamon Y, Lodge MA (2009) From RECIST to PERCIST: Evolving Considerations for PET response criteria in solid tumors. J Nucl Med 50 Suppl 1:122S-150S
64 Benard F, Sterman D, Smith RJ, Kaiser LR, Albelda SM, Alavi A (1999) Prognostic value of FDG PET imaging in malignant pleural mesothelioma. J Nucl Med 40:1241-1245
65 Flores RM (2005) The role of PET in the surgical management of malignant pleural mesothelioma. Lung Cancer 49 Suppl 1:S27-32
66 Kadota K, Kachala SS, Nitadori J et al (2012) High SUVmax on FDG-PET indicates pleomorphic subtype in epithelioid malignant pleural mesothelioma: supportive evidence to reclassify pleomorphic as nonepithelioid histology. J Thorac Oncol 7:1192-1197
67 Abakay A, Komek H, Abakay O et al (2013) Relationship between 18 FDG PET-CT findings and the survival of 177 patients with malignant pleural mesothelioma. Eur Rev Med Pharmacol Sci 17:1233-1241
68 Nowak AK, Francis RJ, Phillips MJ et al (2010) A novel prognostic model for malignant mesothelioma incorporating quantitative FDG-PET imaging with clinical parameters. Clin Cancer Res 16:2409-2417
69 Basu S, Saboury B, Torigian DA, Alavi A (2011) Current evidence base of FDG-PET/CT imaging in the clinical management of malignant pleural mesothelioma: emerging significance of image segmentation and global disease assessment. Mol Imaging Biol 13:801-811
70 Klabatsa A, Chicklore S, Barrington SF, Goh V, Lang-Lazdunski L, Cook GJ (2014) The association of 18F-FDG PET/CT parameters with survival in malignant pleural mesothelioma. Eur J Nucl Med Mol Imaging 41:276-282
71 Lee HY, Hyun SH, Lee KS et al (2010) Volume-based parameter of 18)F-FDG PET/CT in malignant pleural mesothelioma: prediction of therapeutic response and prognostic implications. Ann Surg Oncol 17:2787-2794
72 Schaefer NG, Veit-Haibach P, Soyka JD, Steinert HC, Stahel RA (2012) Continued pemetrexed and platin-based chemotherapy in patients with malignant pleural mesothelioma (MPM): value of 18F-FDG-PET/CT. Eur J Radiol 81:e19-25
73 Genestreti G, Moretti A, Piciucchi S et al (2012) FDG PET/CT Response Evaluation in Malignant Pleural Mesothelioma Patients Treated with Talc Pleurodesis and Chemotherapy. J Cancer 3:241-245
74 Coolen J, De Keyzer F, Nafteux P et al (2014) Malignant Pleural Mesothelioma: Visual Assessment by Using Pleural Pointillism at Diffusion-weighted MR Imaging. Radiology. 10.1148/radiol.14132111:132111
75 Afaq A, Andreou A, Koh DM (2010) Diffusion-weighted magnetic resonance imaging for tumour response assessment: why, when and how? Cancer Imaging 10:S179-S188
76 Perez-Lopez R, Mateo J, Mossop H et al (2016) Diffusion-weighted Imaging as a Treatment Response Biomarker for Evaluating Bone Metastases in Prostate Cancer: A Pilot Study
77 Buijs M, Kamel IR, Vossen JA, Georgiades CS, Hong K, Geschwind J-FH (2007) Assessment of Metastatic Breast Cancer Response to

Chemoembolization with Contrast Agent–enhanced and Diffusion-weighted MR Imaging. Journal of Vascular and Interventional Radiology 18:957-963
78 Batchelor TT, Sorensen AG, di Tomaso E et al (2007) AZD2171, a Pan-VEGF Receptor Tyrosine Kinase Inhibitor, Normalizes Tumor Vasculature and Alleviates Edema in Glioblastoma Patients. Cancer cell 11:83-95
79 Song I, Kim CK, Park BK, Park W (2010) Assessment of response to radiotherapy for prostate cancer: value of diffusion-weighted MRI at 3 T. American Journal of Roentgenology 194:W477-W482
80 Kharuzhyk S, Fabel M, von Tengg-Kobligk H, Kauczor H-U (2008) Image-based evaluation of tumor response to treatment: where is radiology today. Exp Oncol 30:181-189
81 Coolen J, De Keyzer F, Nafteux P et al (2012) Malignant Pleural Disease: Diagnosis by Using Diffusion-weighted and Dynamic Contrast-enhanced MR Imaging—Initial Experience. Radiology 263:884-892
82 Balduyck B, Trousse D, Nakas A, Martin-Ucar AE, Edwards J, Waller DA (2010) Therapeutic surgery for nonepithelioid malignant pleural mesothelioma: is it really worthwhile? The Annals of thoracic surgery 89:907-911
83 Curran D, Sahmoud T, Therasse P, van Meerbeeck J, Postmus PE, Giaccone G (1998) Prognostic factors in patients with pleural mesothelioma: the European Organization for Research and Treatment of Cancer experience. Journal of Clinical Oncology 16:145-152
84 Baysal T, Bulut T, Gökirmak M, Kalkan S, Dusak A, Dogan M (2004) Diffusion-weighted MR imaging of pleural fluid: differentiation of transudative vs exudative pleural effusions. European Radiology 14:890-896
85 İnan N, Arslan A, Akansel G, Arslan Z, Eleman L, Demirci A (2009) Diffusion-weighted MRI in the characterization of pleural effusions. Diagnostic and Interventional Radiology 15:13
86 Armato SG, 3rd, Labby ZE, Coolen J et al (2013) Imaging in pleural mesothelioma: a review of the 11th International Conference of the International Mesothelioma Interest Group. Lung Cancer 82:190-196
87 Giesel FL, Bischoff H, von Tengg-Kobligk H et al (2006) Dynamic Contrast-Enhanced MRI of Malignant Pleural MesotheliomaA Feasibility Study of Noninvasive Assessment, Therapeutic Follow-up, and Possible Predictor of Improved Outcome. CHEST Journal 129:1570-1576
88 Hylton N (2006) Dynamic contrast-enhanced magnetic resonance imaging as an imaging biomarker. Journal of clinical oncology 24:3293-3298
89 Giesel FL, Choyke PL, Mehndiratta A et al (2008) Pharmacokinetic analysis of malignant pleural mesothelioma-initial results of tumor microcirculation and its correlation to microvessel density (CD-34). Acad Radiol 15:563-570
90 O'connor JP, Aboagye EO, Adams JE et al (2017) Imaging biomarker roadmap for cancer studies. Nature reviews Clinical oncology 14:169
91 Mulshine JL, Gierada DS, Armato SG et al (2015) Role of the Quantitative Imaging Biomarker Alliance in Optimizing CT for the Evaluation of Lung Cancer Screen–Detected Nodules. Journal of the American College of Radiology 12:390-395
92 Bloch F (1946) Nuclear induction. Physical review 70:460
93 Purcell EM, Torrey HC, Pound RV (1946) Resonance absorption by nuclear magnetic moments in a solid. Physical review 69:37

94 Hornak JP (1996-2017) The Basics of MRI. Interactive Learning Software, Henietta, NY. Available via http://www.cis.rit.edu/htbooks/mri/index.html

95 Haacke EM, Brown RW, Thompson MR, Venkatesan R (1999) Magnetic Resonance Imaging: Physical Principles and Sequence Design. Wiley

96 Pruessmann KP, Weiger M, Scheidegger MB, Boesiger P (1999) SENSE: sensitivity encoding for fast MRI. Magnetic resonance in medicine 42:952-962

97 McKinnon G (1993) Ultrafast interleaved gradient-echo-planar imaging on a standard scanner. Magnetic resonance in medicine 30:609-616

98 Butts K, Riederer SJ, Ehman RL, Thompson RM, Jack CR (1994) Interleaved echo planar imaging on a standard MRI system. Magnetic resonance in medicine 31:67-72

99 Müller M, Prasad P, Siewert B, Nissenbaum MA, Raptopoulos V, Edelman RR (1994) Abdominal diffusion mapping with use of a whole-body echo-planar system. Radiology 190:475-478

100 Wu W, Miller KL (2017) Image formation in diffusion MRI: A review of recent technical developments. Journal of Magnetic Resonance Imaging 46:646-662

101 Koh DM, Collins DJ (2007) Diffusion-weighted MRI in the body: applications and challenges in oncology. American Journal of Roentgenology 188:1622-1635

102 Koh DM, Takahara T, Imai Y, Collins DJ (2007) Practical aspects of assessing tumors using clinical diffusion-weighted imaging in the body. Magnetic Resonance in Medical Sciences 6:211-224

103 Henzler T, Schmid-Bindert G, Schoenberg SO, Fink C (2010) Diffusion and perfusion MRI of the lung and mediastinum. European journal of radiology 76:329-336

104 Bammer R (2003) Basic principles of diffusion-weighted imaging. European journal of radiology 45:169-184

105 Koh D-M, TAKAHARA T, IMAI Y, COLLINS DJ (2007) Practical aspects of assessing tumors using clinical diffusion-weighted imaging in the body. Magnetic Resonance in Medical Sciences 6:211-224

106 Donati OF, Chong D, Nanz D et al (2014) Diffusion-weighted MR imaging of upper abdominal organs: field strength and intervendor variability of apparent diffusion coefficients. Radiology 270:454-463

107 Koh DM, Blackledge M, Collins DJ et al (2009) Reproducibility and changes in the apparent diffusion coefficients of solid tumours treated with combretastatin A4 phosphate and bevacizumab in a two-centre phase I clinical trial. Eur Radiol 19:2728-2738

108 Padhani AR, Liu G, Koh DM et al (2009) Diffusion-weighted magnetic resonance imaging as a cancer biomarker: consensus and recommendations. Neoplasia 11:102-125

109 Blackledge MD, Collins DJ, Tunariu N et al (2014) Assessment of treatment response by total tumor volume and global apparent diffusion coefficient using diffusion-weighted MRI in patients with metastatic bone disease: a feasibility study. PloS one 9:e91779

110 Blackledge MD, Leach MO, Collins DJ, Koh D-M (2011) Computed diffusion-weighted MR imaging may improve tumor detection. Radiology 261:573-581

111 Rosenkrantz AB, Chandarana H, Hindman N et al (2013) Computed diffusion-weighted imaging of the prostate at 3 T: impact on image quality and tumour detection. European radiology 23:3170-3177

112 Bittencourt LK, Attenberger UI, Lima D et al (2014) Feasibility study of computed vs measured high b-value (1400 s/mm²) diffusion-weighted MR images of the prostate. World journal of radiology 6:374

113 Vural M, Ertaş G, Onay A et al (2014) Conspicuity of Peripheral Zone Prostate Cancer on Computed Diffusion-Weighted Imaging: Comparison of cDWI 1500, cDWI 2000, and cDWI 3000. BioMed research international

114 Feuerlein S, Davenport M, Krishnaraj A, Merkle E, Gupta R (2015) Computed high b-value diffusion-weighted imaging improves lesion contrast and conspicuity in prostate cancer. Prostate cancer and prostatic diseases

115 Grant KB, Agarwal HK, Shih JH et al (2015) Comparison of calculated and acquired high b value diffusion-weighted imaging in prostate cancer. Abdominal imaging 40:578-586

116 Ueno Y, Takahashi S, Kitajima K et al (2013) Computed diffusion-weighted imaging using 3-T magnetic resonance imaging for prostate cancer diagnosis. European radiology 23:3509-3516

117 Cheng L, Blackledge MD, Collins DJ, Tunariu N, Leach MO, Koh DM (2015) The use of Quantitative T2 to enhance Computed Diffusion Weighted Imaging. Intl. Soc. Mag. Reson. Med 23, Toronto, Canada, pp 3599

118 Bito Y, Hirata S, Yamamoto E (1995) Optimal gradient factors for ADC measurementsProc Intl Soc Magn Reson Med, pp 913

119 Jones D, Horsfield M, Simmons A (1999) Optimal strategies for measuring diffusion in anisotropic systems by magnetic resonance imaging. Magn Reson Med 42

120 Saritas EU, Lee JH, Nishimura DG (2011) SNR dependence of optimal parameters for apparent diffusion coefficient measurements. Medical Imaging, IEEE Transactions on 30:424-437

121 Kingsley PB (2006) Introduction to diffusion tensor imaging mathematics: Part II. Anisotropy, diffusion-weighting factors, and gradient encoding schemes. Concepts in Magnetic Resonance Part A 28:123-154

122 Douglas NHM, Winfield JM, deSouza NM, Collins DJ, Orton MR (2013) Development of a Phantom for Quality Assurance in Multi-Centre Clinical Trials with Diffusion-Weighted MRIIntl. Soc. Mag. Reson. Med., Salt Lake City, USA, pp 3114

123 Blackledge MD, Collins DJ, Koh D-M, Leach MO (2016) Rapid development of image analysis research tools: Bridging the gap between researcher and clinician with pyOsiriX. Computers in Biology and Medicine 69:203-212

124 Russ JC, Neal FB (2015) The Image Processing Handbook, Seventh Edition. CRC Press, pp 300-301

125 Gudbjartsson H, Patz S (1995) The Rician distribution of noisy MRI data. Magnetic resonance in medicine 34:910-914

126 Jones DK, Basser PJ (2004) “Squashing peanuts and smashing pumpkins”: How noise distorts diffusion-weighted MR data. Magnetic Resonance in Medicine 52:979-993

127 Provenzale JM, Engelter ST, Petrella JR, Smith JS, MacFall JR (1999) Use of MR exponential diffusion-weighted images to eradicate T2 "shine-through" effect. American Journal of Roentgenology 172:537-539
128 Park SY, Kim CK, Park JJ, Park BK (2016) Exponential apparent diffusion coefficient in evaluating prostate cancer at 3 T: preliminary experience. The British journal of radiology 89:20150470
129 Kimura T, Sakashita N, Machii Y (2015) A short-TE Computed Diffusion Imaging (CDWI)Intl. Soc. Mag. Reson. Med 23, pp 2929
130 Gatidis S, Schmidt H, Martirosian P, Nikolaou K, Schwenzer NF (2015) Apparent diffusion coefficient-dependent voxelwise computed diffusion-weighted imaging: An approach for improving SNR and reducing T2 shine-through effects. Journal of Magnetic Resonance Imaging
131 Vezhnevets V, Konouchine V (2005) GrowCut: Interactive multi-label ND image segmentation by cellular automataproc. of Graphicon. Citeseer, pp 150-156
132 Vezhnevets V, Konouchine V (2005) GrowCut: Interactive multi-label ND image segmentation by cellular automataproc. of Graphicon. Citeseer, pp 150-156
133 Egger J, Kapur T, Fedorov A et al (2013) GBM volumetry using the 3D Slicer medical image computing platform. Scientific reports 3:1364
134 Fedorov A, Beichel R, Kalpathy-Cramer J et al (2012) 3D Slicer as an image computing platform for the Quantitative Imaging Network. Magnetic resonance imaging 30:1323-1341
135 Egger J, Nimsky C, Chen X (2017) Vertebral body segmentation with GrowCut: Initial experience, workflow and practical application. SAGE Open Medicine 5:2050312117740984
136 Grady L (2006) Random walks for image segmentation. IEEE transactions on pattern analysis and machine intelligence 28:1768-1783
137 Kakutani S (1945) Markoff process and the Dirichlet problem. Proceedings of the Japan Academy 21:227-233
138 Doyle P, Snell L (1984) Random Walks and Electric Networks (Carus Mathematical Monographs). Mathematical Assn of America, first printing edition
139 Pass HI, Pogrebniak HW (1993) Malignant pleural mesothelioma. Current problems in surgery 30:926-1012
140 Priola AM, Priola SM, Gned D et al (2017) Diffusion-weighted quantitative MRI of pleural abnormalities: Intra-and interobserver variability in the apparent diffusion coefficient measurements. Journal of Magnetic Resonance Imaging 46:769-782
141 Revelli M, Chiesa F, Del Prato A et al (2016) Role of respiratory-triggered diffusion-weighted MRI in the assessment of pleural disease. The British journal of radiology 89:20160289
142 Bland JM, Altman DG (1986) Statistical methods for assessing agreement between two methods of clinical measurement. lancet 1:307-310
143 Limpert E, Stahel WA, Abbt M (2001) Log-normal Distributions across the Sciences: Keys and CluesOn the charms of statistics, and how mechanical models resembling gambling machines offer a link to a handy way to characterize log-normal distributions, which can provide deeper insight into variability and probability—normal or log-normal: That is the question. BioScience 51:341-352

144 Blackledge MD, Tunariu N, Orton MR et al (2016) Inter- and Intra-Observer Repeatability of Quantitative Whole-Body, Diffusion-Weighted Imaging (WBDWI) in Metastatic Bone Disease. PLoS ONE 11:e0153840
145 Dempster AP, Laird NM, Rubin DB (1977) Maximum likelihood from incomplete data via the EM algorithm. Journal of the royal statistical society Series B (methodological):1-38
146 Cheng L, Blackledge MD, Collins DJ et al (2016) T2-adjusted computed diffusion-weighted imaging: A novel method to enhance tumour visualisation. Computers in biology and medicine 79:92-98
147 Pedregosa F, Varoquaux G, Gramfort A et al (2011) Scikit-learn: Machine learning in Python. Journal of machine learning research 12:2825-2830
148 Jerome NP, Orton MR, d'Arcy JA, Collins DJ, Koh DM, Leach MO (2014) Comparison of free-breathing with navigator-controlled acquisition regimes in abdominal diffusion-weighted magnetic resonance images: Effect on ADC and IVIM statistics. Journal of Magnetic Resonance Imaging 39:235-240
149 Malyarenko DI, Newitt D, J. Wilmes L et al (2016) Demonstration of nonlinearity bias in the measurement of the apparent diffusion coefficient in multicenter trials. Magnetic resonance in medicine 75:1312-1323
150 Taouli B, Beer AJ, Chenevert T et al (2016) Diffusion-weighted imaging outside the brain: Consensus statement from an ISMRM-sponsored workshop. Journal of Magnetic Resonance Imaging 44:521-540

Relevant publications

Journal publications

1. **L. Cheng**, et al. "T2-adjusted computed diffusion-weighted imaging: A novel method to enhance tumour visualisation." Computers in Biology and Medicine 79 (2016): 92-98.
2. **L. Cheng**, et al. "Response evaluation in mesothelioma: Beyond RECIST." Lung Cancer 90.3 (2015): 433-441.

Conference proceedings

1. **L. Cheng**, et al, "Repeatability study of tumour volume and ADC from 3D semi-automatic segmentation and global thresholding in malignant pleural mesothelioma using DWI" Cancer Research UK Annual meeting (London), 2017.
2. **L. Cheng**, et al, "Treatment effect evaluation in tumour volume changes in malignant pleural mesothelioma using DWI: preliminary results" Cancer Research UK Annual meeting (London), 2017.
3. **L. Cheng**, et al, "Assessment off Repeatability of Disease Burden and ADC estimates in Malignant Pleural Mesothelioma using Diffusion Weighted Imaging" ISMRM (Hawaii), 2017.
4. **L. Cheng**, et al, "Contrast improvement in malignant pleural mesothelioma by using T_2-adjusted computed diffusion-weighted imaging" British Chapter ISMRM (Leeds), 2016
5. **L. Cheng**, et al, "Characterisation of disease heterogeneity in malignant pleural mesothelioma using mixture modelling of ADC and R2" ISMRM (Singapore), 2016.
6. **L. Cheng**, et al, "The Use of Quantitative T2 to Enhance Computed Diffusion Weighted Imaging", ISMRM (Toronto), 2015.